Aalborg Universitet

AALBORG UNIVERSITY

DENMARK

D1.3 -- Short Report on the First Draft Multi-link Channel Model

Steinböck, Gerhard; Fleury, Bernard Henri; Pedersen, Troels; Raulefs, Ronald; Steinboeck, Gerhard; Wang, Wei

Publication date:
2011

Document Version
Early version, also known as pre-print

[Link to publication from Aalborg University](#)

ICT–248894 WHERE2

D1.3

Short Report on the First Draft Multi-link Channel Model

Contractual Date of Delivery to the CEC:	M12
Actual Date of Delivery to the CEC:	11.07.2011
Editor:	Gerhard Steinboeck, Bernard H. Fleury
Authors:	Troels Pedersen, Ronald Raulefs, Gerhard Steinboeck, Wei Wang
Participants:	AAU, DLR
Work package:	WP1 – Scenarios, Relevant Models and Market Feedback
Est. person months:	
Security:	PU
Nature:	R
Version:	1.0
Total number of pages:	123

Abstract:

This deliverable is a preliminary report on the activities towards multi-link channel models. It summarizes the activities and achievements of investigations of WP1 Task 1.2 in the first year of the project. In this deliverable work focuses on the characterization of the cross-correlation of multi-link large scale parameters, such as rms delay spread, from outdoor to indoor scenarios and for different carrier frequencies. Furthermore indoor radio propagation in in-room scenarios is considered and first modeling approaches, potantially suitable for multi-link channels are presented. A sparse estimator of the dominant multipath components in the response of the radio channel is also proposed.

Keyword list: Multi-link channels, delay-power spectrum, power delay profile, path loss, rms delay spread, mean delay, large scale parameters, outdoor-to-indoor, indoor, reverberation, avalanche effect, propagation graph, positioning, tracking, non-line of sight bias, sparse parameter estimation.

Disclaimer:

EXECUTIVE SUMMARY

In this deliverable the intermediate research results, conducted in WHERE2 WP1, for the purpose of characterizing the multi-link radio channel are presented. This deliverable is structured in two parts, a body part that provides a summary of the reported activities organized topic-wise, and an appendix containing all related publications and reports produced within WP1. The latter documents are meant to provide the readers with more detailed information on the activities if needed or wanted.

The body part of the deliverable summarizes in Section 2 a measurement campaign conducted by DLR and AAU. The purpose of the campaign is the characterization of radio channels for cooperative localization and the validation of reverberant in-room channels. The data is not part of the WHERE2 project but is extensively used and analyzed within the project. The extensive measurement report can be found in Appendix A.1. First results using these measurements are also included in this deliverable.

First results of the characterization of the cross-correlation of multi-link large scale parameters are summarized in Section 3. The work so far has focused on the characterization of delay dependent large scale parameters and the range estimation error due to the non-line of sight bias. These investigations were done specifically for multi-link channels and for multi-carrier frequencies for the outdoor-to-indoor channel. Detailed information on this topic can be found in the Appendices A.2 and A.3.

Section 4 summarizes recent on-going work on reverberant in-room radio channel models. A distance-dependent delay-power spectrum model of in-room channels is considered. The proposed model is used to characterize various distance dependent parameters such as the received signal strength, mean delay and rms delay spread. The model allows for the prediction of these parameters for in-room multi-link scenarios. Furthermore, this section contains a model that describes the response of the indoor radio channel. The model's uniqueness is the consideration of the so-called avalanche effect. The structure of the model allows for an efficient implementation of multi-link channels. Details on these models can be found in the Appendices A.4 and A.5.

A sparse radio channel parameter estimator is summarized in Section 5. The avalanche effect observed in measurements makes it extremely difficult to reliably estimate parameters of multipath components. The presented method allows for the joint estimation of the parameters and the number of dominant multipath components. The method is also crucial for delay-power-profile based fingerprinting. A detailed description of the estimation algorithm can be found in Appendix A.6.

The presented results and the ongoing activities presented in this deliverable, together with the results and ongoing activities on non-stationary channels of deliverable D1.4 as well the investigations on ray-tracing tools in deliverables D1.5 and D1.6, form the basis for the characterization of a multi-link channel model.

TABLE OF CONTENTS

Authors

Partner	Name	Phone/e-mail
AAU	Bernard H. Fleury	Phone: +45 9940 8629
		e-mail: bfl@es.aau.dk
	Troels Pedersen	Phone: +45 9940 8672
		e-mail: troels@es.aau.dk
	Gerhard Steinboeck	Phone: +45 9940 8615
		e-mail: gs@es.aau.dk
DLR	Ronald Raulefs	Phone: +49 8153 28 2803
		e-mail: Ronald.Raulefs@dlr.de
	Wei Wang	Phone: +49 8153 28 2801
		e-mail: Wei.Wang@dlr.de

List of Acronyms and Abbreviations

3GPP	3rd Generation Partnership Project
CIR	Channel Impulse Response
FDP	First Detectable Path
GLoS	Geometrical Line-of-Sight
GNSS	Global Navigation Satellite Systems
GPS	Global Positioning System
LoS	Line-of-Sight
NLoS	None Line-of-Sight
PDP	Power Delay Profile
RMS	Root Mean Square
TB	Time Based
WHERE2	Wireless Hybrid Enhanced Mobile Radio Estimators - Phase 2
WP	Work Package

1   INTRODUCTION

As already identified in Annex I "Description of Work" of the WHERE2 project description [1], the positioning accuracy achievable with global navigation satellite systems can be greatly improved by usage of additional terrestrial mobile radio standards. This results in a combination of various standards in the form of heterogeneous multi-link systems. To characterize multi-link channels, for both localization and communication purposes, research in the WHERE2 project focuses on 1) the characterization of the statistical dependency between channel links, 2) the characterization of the transition of outdoor-to-indoor, 3) the non-stationarity and time variance, and 4) development of signal processing techniques that enable to conduct the investigations in items 1) to 3).

Typical channel models for radio communications and localization purposes, proposed sofar, only considered single-link propagation. Lately, in radio communication systems, the focus shifted towards multi-link systems but localization aspects are, if at all, only scarcely considered in these research activities. This is due to the different purpose in radio communications, namely the statistical description of the radio channel for evaluation of transceiver systems. The research activities in WHERE2 WP1 address these deficiencies and work is on-going towards a description of multi-link channel models for localization purposes.

In the following the intermediate research results, conducted in WHERE2 WP1, for the purpose of characterizing the multi-link radio channel are presented. This report is structured in two parts, a body part that provides a summary of the reported activities organized topic-wise, and an appendix containing all related publications and reports produced within WP1. The latter documents are meant to provide the readers with more detailed information on the activities if needed or wanted.

Section 2: A description of a measurement campaign conducted by DLR and AAU is provided. The purpose of the campaign is the characterization of radio channels for co-operative localization and the validation of reverberant in-room channels. First results using these data are already presented in this deliverable.

Section 3: Results on the correlation of large scale parameters of outdoor-to-indoor multi-link radio channels are summarized. The focus is on the correlation of time dispersive parameters in the multi-link and multi-carrier-frequency case and the bias of the time of arrival estimates of the first component, due to non-line of sight situations.

Section 4: This section presents recent and on-going work on in-room radio propagation channel models. A distance-dependent delay-power spectrum model of in-room channels is considered. The proposed model is used to characterize various distance dependent parameters such as the received signal strength, mean delay and rms delay spread. The model allows for the prediction of these parameters for in-room multi-link scenarios. A model that describes the response of the indoor radio channel is summarized in Section 4.3. The model's uniqueness is the consideration of the so-called avalanche effect. The structure of the model allows for an efficient implementation of multi-link channels.

Section 5: The sparse radio channel parameter estimation is addressed. The avalanche effect observed in measurements makes it extremely difficult to estimate reliably parameters of multipath components. The presented method allows for the joint estimation of the parameters and the number of dominant multipath components. The method is also crucial for delay-power-profile based fingerprinting.

Section 6: Conclusions.

Appendix A: The appendix contains a collection of already published or soon to be published articles or reports produced within the WHERE2 project. This collection contains more detailed information on the various sections in the deliverable.

2   MULTI-LINK AND REVERBERANT CHANNEL MEASUREMENT CAMPAIGN

A measurement campaign, not part of the WHERE2 project, with the focus on indoor multi-link and reverberant in-room channels was conducted by DLR and AAU. The measurement data is used from both parties within the WHERE2 project and can be shared with other partners upon request.

The measurement campaign has two main goals. Firstly to validate models for in-room channels including reverberation effects and secondly to provide measurement data for cooperative localization methods. First results using these data are already presented in this deliverable. For the measurement campaign the measurement platform for time-variant wireless channels from DLR, introduced in WHERE2 D1.4, was used. The high spatial resolution of the platform allows for combining several transmitter positions to a virtual array. Together with the circular receiver array, this enables a bi-directional channel characterization.

Reverberant Channel Measurement: Towards the end of the previous WHERE project a delay-power spectrum model based on the observations from measurements was proposed. Previous measurement campaigns e.g. in the WHERE project, were not fully suitable for validation of the model due to limited amount of data in the spatial domain. Thus for the validation of the proposed model it is necessary to have transmitter-receiver distances covering almost all possible distances in the room. The data should also allow for the development of further models accounting for the physical mechanisms leading to the reverberation phenomena. Thus several experiments, for instance with closed and opened windows or people placed around the conference table, were conducted.

Cooperative Localization Measurement: There is to our knowledge no measurement data for cooperative localization available, which contains detailed information on the transmitter and receiver positions, the antenna pattern and their rotation. We have defined scenarios that cover both LoS and NLoS links between transmitter and receiver. The choice of transmitter and receiver locations offer a robust approach for distance-based evaluation.

The obtained measurement data was already utilized in Section 4.1 and will be further used to evaluate multi-link and time variant channel parameters. A detailed description of the measurement campaign is provided in Appendix A.1.

3   CROSS CORRELATIONS OF MULTI-LINK LARGE SCALE PARAMETERS

Augmenting global navigation satellite systems (GNSSs) based positioning with signals of opportunity improves the position accuracy compared to a GNSS-only solution. The signals of terrestrial mobile radio standards can be exploited in addition to GNSS signals. A promising augmentation approach is to apply time based localization to terrestrial radio signals which provide considerably higher received power levels compared to GNSS [2]. Usually, the links between the mobile terminal and the anchor nodes or base stations are blocked (e.g., by walls or buildings). Moreover the geometrical conditions are worse such that the mobile terminal position can not be resolved accurately. Cooperative positioning, using time of arrival measurements from multiple peer-to-peer links, has been proposed to improve the performance in terms of accuracy and coverage problems.

The wireless channel has a significant impact on localization based on time measurement. The position error is directly related to the range estimation error of individual radio links. This section presents the evaluations of channel parameters in terms of mean delay, delay spread, and positioning related parameter non line of sight (NLoS) bias.

The focus in Section 3.1 is on correlation of time dispersive parameters in the multi-link and multi carrier frequency case. In Section 3.2 the bias, due to non-line of sight situations, of the time of arrival estimates of the first component is studied for the same outdoor-to-indoor measurements.

3.1   Time Dispersion Parameters

The mean delay and rms delay spread are usually of interest for evaluation of time dispersion characteristics. The multi-link rms delay spread and mean delay for different carriers at 2.45 GHz and 5.2 GHz are addressed in Appendix A.2 based on a comparison measurement. In this measurement the accurate transmitter and receiver location information are available. From the results, the outdoor reflections, showing up as clustered structure in the channel impulse response (CIR), introduce significant impact on the delay spread. Moreover it is noticeable that rms delay spread or mean delay do not appear to be significantly different at 2.45 GHz and 5.2 GHz. Besides, the obtained power delay profiles (PDPs) for both bands show the similar shapes. Therefore, the delay spread should be similar. This observation is important since channel models, relying on the rms delay spread for generating wideband CIRs are therefore able to use the same statistics at different carrier frequencies.

For multi-link scenarios, the inter-link time dispersion parameter correlations is an open issue, especially in the scope of cooperative networks. Similarly to the estimation in Appendix A.3, the inter-link correlation coefficient can be obtained for time dispersion parameters to evaluate the correlations. Based on the measurement described in Section 2 for indoor cooperative scenarios, it is interesting to investigate the multi-link cross correlation of the time dispersion parameters.

3.2   Positioning Related Parameters – NLoS Bias

One of the channel characteristics affecting the range estimation error is the positive bias on the first detectable path (FDP). This occurs in situations where the geometric line-of-sight (GLoS) path is blocked. This bias, i.e. the difference between the geometrical distance from the transmitter to the receiver and the propagation distance of the first detectable path is known as the non line-of-sight (NLoS) bias. This bias results in errors of the ranging estimates. Without loss of generality, the NLoS bias could be regarded as a large scale parameter for localization similar as the path loss, K factor, and delay spread in communication.

In order to obtain the characteristics of NLoS bias, analysis based on real channel measurement is desired. The GLoS distance can be obtained by using the tachymeter system.

For those scenarios where the link between transmitter and receiver is blocked, to determine the position of the transmit antenna a tachymeter giving a nominal accuracy in the sub-cm domain was utilized. A similar accuracy is achieved for the receive antenna by using a rotary encoder mounted on the motor of the model railway. The GLoS distance can be calculated straightforward by measuring the coordinates of transmitter and receiver. Concerning the delay of FDP, a super-resolution algorithm, namely SAGE, is used to estimate the channel parameters. Thereafter, the NLoS bias can be obtained.

Based on the measurement described in Section 3.1, we obtained results that show that there are no significant differences of NLoS bias between both carrier frequencies. These results are presented in more detail in Appendix A.2. Moreover to study the multi-link NLoS bias, the correlation coefficients of the NLoS bias between different transmit antenna positions indicate no correlation between NLoS biases from different links as shown in Appendix A.3. However, it is still an open issue to evaluate the inter-link NLoS bias correlation in the cooperative scenarios based on the indoor measurement presented in Section 2. In the indoor scenarios is the number of inter-links larger than in usual cellular networks.

4   REVERBERANT CHANNELS

This section considers indoor radio propagation of reverberant channel scenarios. The research is motivated by observations of the delay-power spectrum in research literature. In Section 4.1 a distance dependent delay-power spectrum model of in-room channels is considered. The proposed model is used to characterize various distance dependent parameters such as the received signal strength, mean delay and rms delay spread. A model to describe the response of the indoor radio channel, which generates similar delay-power spectra as the model in Section 4.1, is summarized in Section 4.3. The model's uniqueness is the consideration of the so-called avalanche effect.

4.1   Modeling the Delay Power Spectrum of Reverberant In-Room Channels

Experimental observations [5, 6] of the behavior of the delay-power spectrum for reverberant in-room channels show that the tail of the delay-power spectrum exhibits the same constant exponential decay regardless of the transmitter and receiver positions. Furthermore, a peak at the early part of the delay-power spectrum is strong at short transmitter-receiver distances and gradually vanishes as the distance increases. A similar behavior is observed in room acoustics [7] and electromagnetic fields in cavities [8].

Based on the observations from [5, 6], we propose in Appendix A.4 a model for the distance dependent delay-power spectrum with a "dominant" and a "reverberant" component. The dominant component represents the early part of the delay-power spectrum consisting of a directly propagating component and possible first-order reflections from the floor, ceiling and walls. The reverberant component represents the multitude of higher order reflections in the room which yield the diffuse tail of the delay-power spectrum. The model allows to predict the path loss, the mean delay and the rms delay spread as a function of transmitter-receiver distance via closed form expressions. Predictions of the model are in good agreement with experimental observations. A comparison to the widely used log-distance path loss model shows that the log-distance model blends the contribution of the dominant and reverberant component. As such the path loss exponent is below the free space path loss exponent. Furthermore, we observed that the log-distance path loss model for short distances overestimates the path loss were as for other distances the path loss is underestimated. The proposed model shows good agreement over the full distance range. Additionally the proposed model allows for the description of the mean delay and rms delay spread versus distance, which could be used as additional parameters in radio localization.

The proposed model for the delay-power spectrum in Appendix A.4 can be used for any transmitter receiver position in the room. It allows for prediction of the distance dependent path loss, mean delay and rms delay spread for multi-link channels. Current preliminary observations indicate that one obtains for the same room different path loss exponents for the log-distance model from measurements where mobile (eg. receiver) moves freely but the anker (eg. transmitter) is positioned at different locations in the room, eg. the center of the room or close to a corner. However this has yet to be verified by experimental data. Furthermore, it is of interest to explore the distance dependency of other parameters such as higher order moments of the delay power spectrum, kurtosis or for instance the Rice factor from the proposed delay-power spectrum model. Another open issue is the coupling between neighboring rooms which would allow the extension of the predictions of the model to neighboring rooms.

4.2   Modeling the Reverberation for In-room Channels

The reverberation time, which is the decay rate of the exponentially decaying tail of the delay power spectrum, plays an important role in radio localization. As is shown in Ap-

pendix A.4 the reverberation time influences several distance dependent parameters used in radio localization such as for instance the received signal strength, or the mean delay and rms delay spread. The distance dependent behavior of the delay-power spectrum shows that for a specific transmitter-receiver distance region, denoted as reverberation region, the early dominant peak can no longer be distinguished from the exponential tail. The reverberation time plays a vital part in characterizing the start and end points of the reverberation region. In delay dependent distance estimation often the strongest peak in the power delay profile is detected and considered as the geometric line of sight. Such an approach will lead to strongly biased distance estimates for distances in the reverberation region where the peak is part of the exponential tail. As we can see from these few examples it is of great interest for radio localization to model and estimate the reverberation time.

In room acoustics [7] a reverberation effect in the room describes the decay rate of the tail of the delay-power spectrum. The well known room acoustic models of Sabine and Eyring express the relation between the reverberation time and geometry in terms of the average wall absorption coefficient. In [6] the Sabine model was considered for indoor radio propagation. Results such as average wall absorption or the decay rate are presented. However, a thorough experimental model validation is missing. The Eyring model is used in [5] to predict the reverberation time. The used average wall absorption coefficient for the prediction is calculated from the electromagnetic properties of wall materials. The predicted and measured delay-power spectra are in good agreement. Unfortunately the power values were normalized before the comparison of the delay-power spectra.

For validating the model assumptions of the reverberation effect, we conducted an experiment within the measurements described in Section 2 with various numbers of open windows in a room. Opening the windows should alter the average wall absorption coefficient of the room. This in turn will result in a change of the decay rate of the reverberant component in the room. Preliminary results of the predicted decay rates show a good agreement to the experimentally obtained values for open windows. However these preliminary results need further investigation to confirm the validity of the assumptions for radio signals. Additional open issues concerning the decay rate are for instance the influence of additional absorbers in the room eg. the human body, possible effects due to coupling from neighboring rooms, and the changes of the decay rate for various room sizes.

4.3   Graph Based Modeling of Reverberant Multi-link Channels

It has been observed from measurements of channels [10] that the spatially averaged channel impulse response for single-link in-room scenarios exhibits an avalanche effect: The earliest signal components, which appear well separated in time, are followed by an avalanche of components arriving with increasing rate of occurrence, gradually merging into a diffuse tail with exponentially decaying power.

In Appendix A.5 we follow a new approach to design a model of the channel response which includes recursive scattering and thereby inherently accounts for the exponential power decay and the avalanche effect. The environment is modeled in terms of a propagation graph in which vertices represent transmitters, receivers, and scatterers, while edges represent propagation conditions between vertices. A closed form expression of the channel transfer function valid for any number of interactions is derived. We discuss an example where interactions are assumed to cause no time dispersion and thus delay occurs only due to propagation in between scatterers. For this example, a stochastic model of the propagation graph is stated based on which realizations of the channel transfer function and impulse response are generated for numerical evaluation. The results reveal that the graph's recursive structure yields both an exponential power decay and an avalanche effect in the generated impulse responses.

The propagation graph modeling framework and associated analytical results proposed in Appendix A.5 also encompass MIMO and multi-link systems. An appealing asset of the modeling framework is that the computational complexity is dominated by the number of scatterers rather than the number of transmitter-receiver links. However, it is an open issue to amend the stochastic example model presented in Appendix A.5 to incorporate multiple links. Such an amendment will enable the study of avalanche effects in multi-link channels via numerical simulations. An additional open issue is the validation of such multi-link models using measurement data.

4.4   Stochastic Model of Avalanche Processes in Reverberant Multi-link Channels

The delay dispersion of radio signals is an important effect, which impacts e.g. the accuracy of time of arrival-based (TOA-based) range estimators. For TOA-based estimation, the early part of the channel impulse response is particularly important, as this part governs the estimation errors. Radio channel models relying on a random spikes representation of the channel impulse response are commonplace for wideband and ultrawideband communications. State of the art models rely on essentially the same principle developed by Turin et al. [12] during the 1970s: The received signal consists of a linear combination of delayed copies of the transmitted signal. The delays are modeled according to a stochastic point process of varying kinds. Common to all models of this type is that assumptions on the intensity (or arrival rate) must be made.

The avalanche effect observed in measurements of indoor reverberant channels [10] indicate that the arrival rate for the signal components should increase with the delay, while the power of each component should decrease in order to allow for an exponentially decaying overall delay-power spectrum. The increasing arrival rate may impact localization applications relying on range estimates derived from estimated propagation delays (such as TOA, DTOA systems). The original model by Turin et al. relies on a Poisson point process of which the intensity function is obtained via extensive measurement campaigns. Similarly, the delay point process in the celebrated Saleh-Valenzuela model and its derivatives are based on a Cox-process, where the intensity parameters are obtained from measurements [13]. Unfortunately, the extraction of the arrival rate from measurements is non-trivial, and error prone, especially in indoor scenarios where reverberation effects prevail. This hassle is no less when considering multi-link channels.

It is therefore of interest to explore the connection between the geometric properties of the radio propagation environment (e.g. a single room, or a building) and the arrival rate. There are several related open issues: Determination of the connection between geometry of the propagation environment and the arrival rate; statement of stochastic models accounting for this connection; and extension of Turin-based models to multi-link channels. Finally, an interesting open issue is the directional properties of the reverberant channels.

5 SPARSE VARIATIONAL BAYESIAN (VB) EXTENSION OF THE SAGE ALGORITHM

When applying high resolution algorithms to the estimation of wireless multipath channels from multidimensional channel measurements, an accurate determination of the number of dominant multipath components is required in order to reproduce the channel behavior in a realistic manner – an essential driving mechanism for the design and development of next generation MIMO-capable wireless communication and localization systems.

In Appendix A.6 a sparse Variational Bayesian (VB) extension of the SAGE algorithm [15] for the high resolution estimation of the parameters of relevant multipath components in the response of frequency and spatially selective wireless channels is proposed. The application context of the algorithm considered is parameter estimation from channel sounding measurements for radio channel modeling purpose.

The new sparse VB-SAGE algorithm extends the classical SAGE algorithm in several respects: by monotonically minimizing the variational free energy, i) distributions of the multipath component parameters can be obtained instead of parameter point estimates and ii) the estimation of the number of relevant multipath components and the estimation of the component parameters are implemented jointly. The sparsity is achieved by defining parametric sparsity priors for the weights of the multipath components.

The Gaussian sparsity priors are revisited within the new VB-SAGE framework and extensions of the sparsity results for complex Laplace priors are investigated. The structure of the new VB-SAGE algorithm allows for an analytical stability analysis of the update expression for the sparsity parameters. This analysis leads to fast, computationally simple, yet powerful, adaptive selection criteria applied to the single multipath component considered at each iteration. The selection criteria are adjusted on a per-component-SNR basis to better account for model mismatches, e.g. diffuse scattering, calibration and discretization errors, allowing for a robust extraction of the relevant multipath components.

The performance of the sparse VB-SAGE algorithm and its advantages over conventional channel estimation methods are demonstrated in synthetic SIMO time-invariant channels; the algorithm has also been applied to real measurement data in a MIMO time-invariant context.

The future extension of the sparse VB-SAGE algorithm should target variational Bayesian estimation of additive white noise and estimation of diffuse multipath part of the channel response. Diffuse multipath contributions can be represented as non-white additive noise with zero mean and covariance matrix that models temporal and spatial structure of diffuse components. Variational methods can be applied to optimally estimate this covariance matrix from measurement data, thus effectively providing a framework for extending the sparse VB-SAGE algorithm to the estimation of diffuse multipath components.

6 CONCLUSIONS

This intermediate deliverable summarizes the ongoing activities of T1.2 in WHERE2 WP1 on the topic of multi-link channel models. The focus in this deliverable is put on the characterization, i.e. measurement, modeling and parameter estimation, of indoor and outdoor-to-indoor single- and multi-link channels.

An indoor measurement campaign for characterizing the radio channel for cooperative localization (multi-link channels) and reverberant in-room channels was introduced in Section 2. The measurement campaign was an initiative of DLR and AAU. The data is not part of the WHERE2 project but is extensively used and analyzed within the project. Results using these measurements are included in this deliverable.

First results of the characterization of the cross-correlation of multi-link large scale parameters were presented in Section 3. The work so far focused on the characterization of delay dependent large scale parameters and the range estimation error due to the non-line of sight bias. These investigations were done specifically for multi-link channels and for multi-carrier frequencies for the outdoor-to-indoor channel.

Indoor propagation was considered in Section 4 for single room scenarios. Motivated from measurement observations, a model for the delay-power spectrum, allowing to characterize several distance dependent large scale parameters such as received signal strength, mean delay and rms delay spread, was presented. A model for the channel response, which includes the avalanche effect, was presented too.

In Section 5 a method to estimate jointly the number and the parameters of relevant multipath components was proposed. Such methods are specifically useful when estimating relevant parameters from channel responses exhibiting an avalanche effect.

The presented results and including future activities are the basic foundation for the description of a multi-link channel model. Together with the results for non-stationary channels of D1.4 and investigations with ray-tracing tools in D1.5 and D1.6, a description for multi-link channel models for localization purposes will be prepared and continuously shared with the other work packages in WHERE2.

A   APPENDIX

The appendix contains a collection of articles and reports with detailed information to the summaries of the different sections in this deliverable, which are results of the WHERE2 project. Table 1 lists titles of the following sections in the appendix.

Table 1: Overview of the collection of papers and reports.

Appendix	Title	Page
A.1	Measurements for Validation of Models for Reverberant and Cooperative Channels	16
A.2	Outdoor-to-Indoor Channels at 2.45 GHz and 5.2GHz for Geolocation Applications	60
A.3	Multiple-Links NLoS Error Evaluations for Geolocation Channel Modelling	66
A.4	Model for the Path Loss of In-room Reverberant Channels	72
A.5	Modeling of Reverberant Radio Channels Using Propagation Graphs	78
A.6	Sparse Variational Bayesian SAGE Algorithm with Application to the Estimation of Multipath Wireless Channels	90

A.1   Measurements for Validation of Models for Reverberant and Cooperative Channels

The internal measurement report from the AAU-DLR measurement campaign can be found on the next pages.

**AAU-DLR 2010 Indoor
Measurement Campaign**

Measurements for Validation of Models for Reverberant and Cooperative Channels

Steinboeck G., Pedersen T., Wang W.

Version: 0.2   Date: 15.06.2011

CONTENTS

CHAPTER 1

MOTIVATION AND PURPOSE FOR THE MEASUREMENT CAMPAIGN

The measurement campaign has two main motivations. One motivation is to provide measurement data to validate models for in-room channel models including reverberation effects and the other motivation is to provide measurement data for cooperative localization methods.

1.1 Motivation for Validation of In-room Reverberant Model

A path loss model was developed based on observations of the behavior of the delay power spectrum. Previous measurement campaigns e.g. in the WHERE project, are not fully suitable for validation due a limited amount of data in the spatial domain. For the validation of the proposed model it is necessary to have transmitter receiver distances covering almost all possible distances in the room. Furthermore the data should allow for spatial averaging at the transmitter and receiver side in order to minimize the influence of small scale fading on the path loss.

One further motivation is to use the experimental data to find out or confirm the physical reasoning for the observed reverberation behavior. The data should also allow for the development of further models accounting for reverberation phenomena.

1.2 Motivation for the Cooperative Localization Measurements

There is to our knowledge no measurement data for cooperative localization available. We have defined scenarios that cover a. LoS and b. NLoS links between
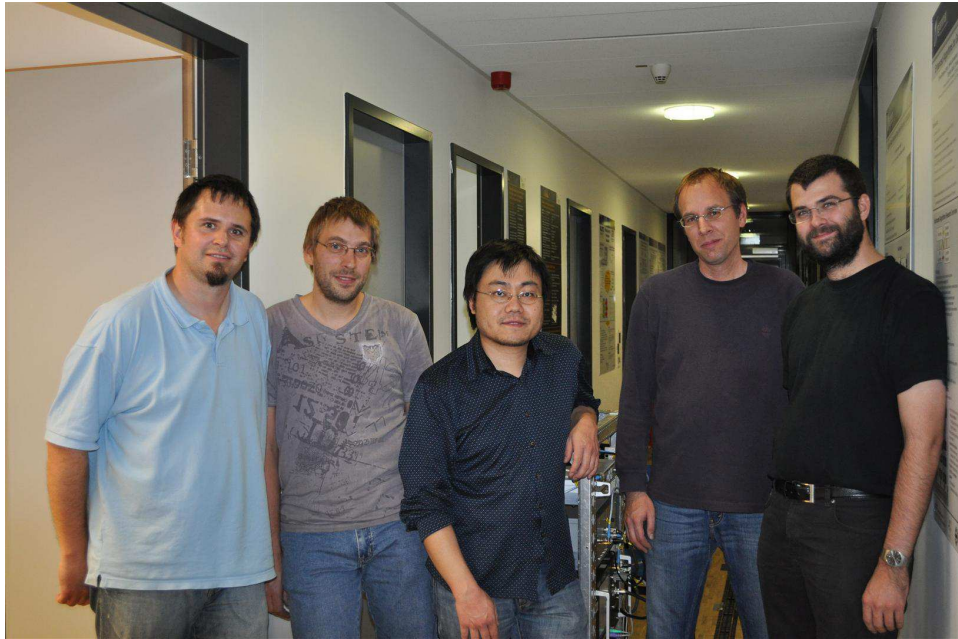
Figure 1.1: Measurement team. (From left to right: Steinboeck G., Jost T., Wang W., Raulefs R. and Pedersen T.)

transmitter and receiver. The three tracks of the train cover potential positions from three sides. This offers a robust approach for distance-based evaluations.

1.3 Measurement Team

The measurements were conducted in cooperation between the Institute for Communication and Navigation from German Aerospace Center (DLR) and the Navigation and Communication Section of Aalborg University (AAU). The people involved during the planing phase of the measurements were Ronald Raulefs and Wei Wang from DLR and Bernard Fleury, Troels Pedersen, and Gerhard Steinboeck from AAU.

During the measurement campaign the main actors were Thomas Jost, Ronald Raulefs, and Wei Wang from DLR. From AAU Troels Pedersen and Gerhard Steinboeck participated in the measurements. The team was supported by numerous other people during measurements, e.g. people taking photos or participating in the experiment described in Section 5.2.3. The measurement team is shown in Fig. 1.1.

CHAPTER 2

ENVIRONMENT

2.1 Measurement Environment

We consider an office environment at DLR premises. A floor plan is shown in Fig. 2.1. The building has 3 story heights above ground floor and a basement. The rooms considered are on the ground floor. The main focus was on the meeting room indicated as R4, because it was the largest room available. Fig. 2.2 shows the meeting room R4, and two offices R3 and R2. At a room height of 2.78 m is a intermediate ceiling of approx. 2 cm hard "mineral wool" slabs . The mineral wool slabs are mounted with metal frames to concrete ceiling with approximately 30 cm distance. The floor was wooden with concrete underneath. The outer walls mainly consist of windows with metallic coating occasionally interrupted by concrete pillars. The inner walls are drywalls and are the same for all inner walls. There are white boards in each room with the size of $1.8 \times 1.2 \text{m}^2$.

The transmitting antenna was mounted for the measurements on a model train at a height of 1.26 m. We considered two tracks of the model train in the meeting room R4, indicated with T1 and T2 and one track in in the office R3 labeled as T3.

The circular receiver antenna array with 8 elements was placed on several positions in the three rooms marked with red crosses. The receiver positions labeled with Rp1 to Rp9 are measured from all tracks and are at a height of 1.1 m. For the cooperative localization 10 additional receiver positions labeled as T1Rp1 to T1Rp5 and T2Rp1 to T2Rp5 at a height of 1.2 m were added. The channel was measured for these positions only with track T3 and T1 or T2 respectively.

Doors and windows are closed during the measurements, otherwise indicated.

The positions of white boards, heaters, windows, pillars, table, the receiver coordinates and several other things with respect to the walls have been measured as well. The results are indicated in Fig. 2.4.

The distance to the tree line outside of the building (see e.g. Fig. 4.2 in the windows) is approximately 22 m.
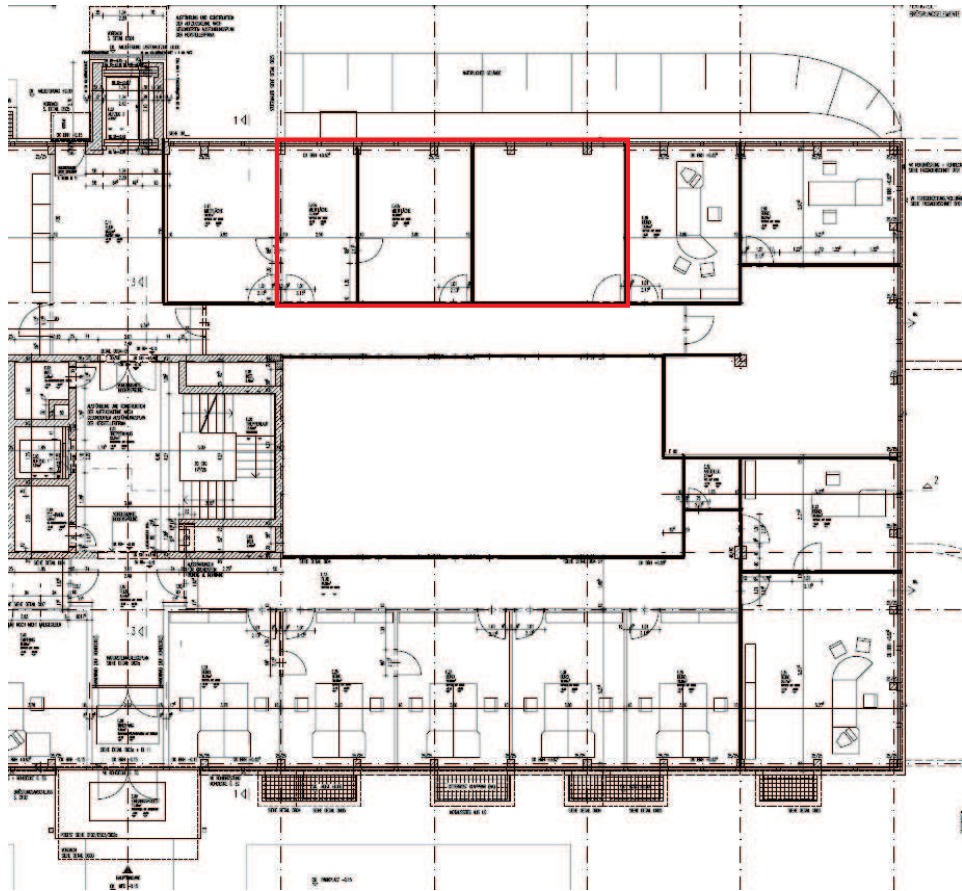
Figure 2.1: Ground floor of the DLR building. The red rectangle outlines rooms R2, R3 and R4 considered in the measurement campaign.
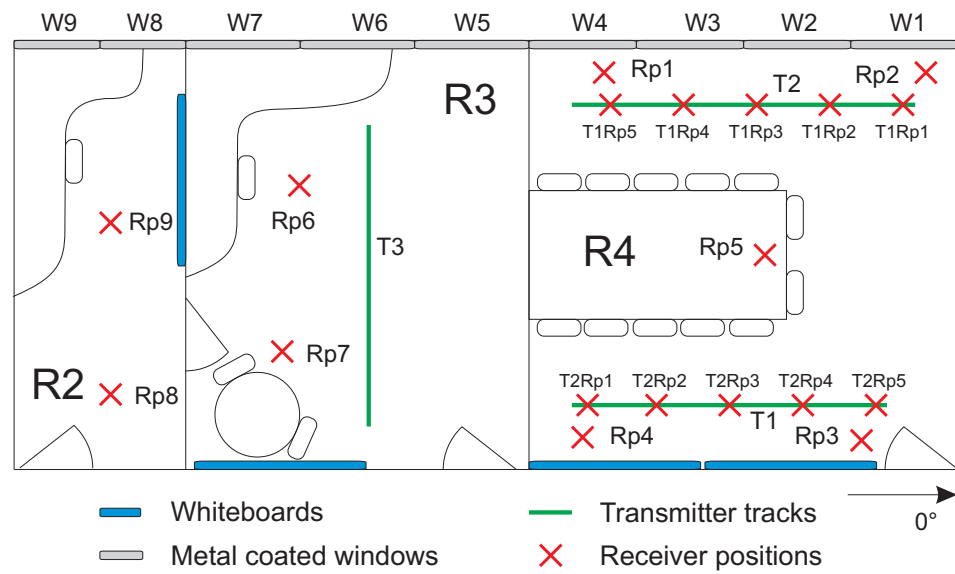

Figure 2.2: DLR premises for the measurement campaign.

2.2 Measuring Distances

The receiver and transmitter positions have been measured with a tachymeter and the coordinates are available in different formats. The moving of the transmitter was recorded with the tachymeter. In addition during the measurements were odometer pulses recorded with the channel sounder receiver unit.

The model railway is running on a cogwheel to prevent wheel slipping. The HEDL 5540 rotary encoder mounted on the model train engine counts the engine turns by giving 500 impulses per full rotation. This allows determining the odometer factor defined as the number of impulses per meter from measurements. To obtain this value, $K = 21$ train runs have been performed with traveled distance m_k and counted encoder impulses n_k for each run $k = 1, ..., K$. The odometer factor ρ is calculated as the sample mean

$$\rho = \frac{1}{K} \sum_{k=1}^{K} \frac{n_k}{m_k}. \tag{2.1}$$

Based on the K measurements, ρ is determined as $105212.52 \, \mathrm{m}^{-1}$. It indicates that the rotary encoder counts around 105212 impulses per traveled meter. This translates into $\simeq 105$ impulses for a traveled distance of $1 \, \mathrm{mm}$. In general a rotary encoder with less impulses per motor turn might be used, with the drawback of less spatial resolution. An estimate $\hat{m}$ of the traveled distance can be calculated straightforward as

$$\hat{m}_k = \frac{n_k}{\rho}. \tag{2.2}$$

The estimation error ζ_k between $\hat{m}_k$ and the true distance m_k normalized to m_k is defined as

$$\zeta_k = \frac{\hat{m}_k - m_k}{m_k}. \tag{2.3}$$

Taking all K measurements into account a mean error $\mu = -0.0024 \, \mathrm{mm/m}$ with standard deviation $\sigma = 0.2266 \, \mathrm{mm/m}$ is obtained as shown in Fig. 2.3. By storing the number of rotary encoder impulses synchronously with each measured CIR snapshot, since the start of the train movement, a traveled distance for each CIR snapshot can be obtained in a straightforward manner.

Unfortunately, the channel sounder raw data file format provides not the recorded number of odometer pulses. Instead a distance value with the configured number of pulses per meter is stored. The channel sounder has a limitation on the number of odometer pulses (100000) per meter. Thus one can calculate the corrected moved distance d_{true} along the track since the start of a measurement run as:

$$d_{true} = \frac{I_{Nav}}{I_{real}} \cdot d_{Nav}, \tag{2.4}$$

where I_{Nav} was set to the maximum possible number of odometer pulses (100000) in the channel sounder, I_{real} corresponds to above obtained $\rho = 105212$ and d_{Nav} is the distance recorded in the measurement data. The values of d_{Nav} and I_{Nav} can be retrieved from the raw data files using the Matlab function RSKNav from MEDAV.
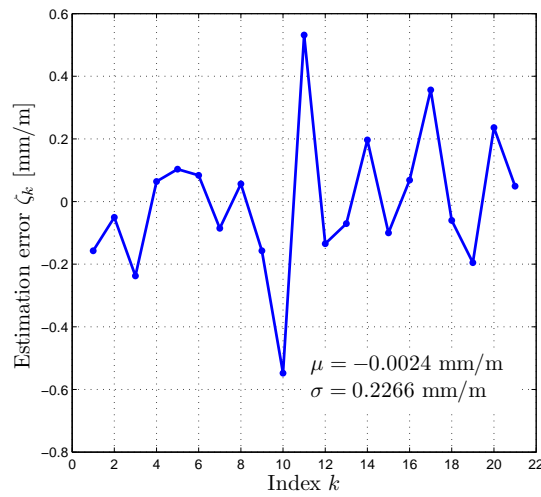
Figure 2.3: Estimation error of the distance for the $K = 21$ measurements obtained with $\rho = 105212$.

Figure 2.4: Measurements of the environment taken during the measurement campaign.

CHAPTER 3

CHANNEL SOUNDING EQUIPMENT

3.1 Channel Sounder and Setup

In the diagram of Fig. 3.1 is the general measurement setup shown. The three channel sounder units (transmitter, receiver and clock generator) were placed outside of room R4 in the corridor. The transmitter antenna was placed on a model train moving along T1, T2, or T3. During movement the train odometer creates pulses which are recorded from the receiver unit and stored together with the measurement data. The receiver unit of the channel sounder controls the multiplexer of the receive antennas.

3.1.1 Synchronization of Transmitter and Receiver

The transmitter and the receiver were both connected via same type of coaxial cables of length approximately 60 m with the rubidium clock generator unit of the channel sounder.

3.1.2 Transmitter Measurement Setup

The transmitter setup is shown in Fig. 3.1. The transmit antenna is mounted on a rail road car of a model train is shown in Fig. 3.8b. The height of the transmit antenna is 1.26 m.

3.1.3 Receiver Measurement Setup

The antennas were connected with short cables to the inputs of the multiplexer (see e.g. Fig. 3.2). The output of the multiplexer was connected with a 9 m long low-loss RF-cable SUCOFLEX 100 from Huber&Suhner with attenuation of 6 dB, labeled as "Z10A" to a 10 dB attenuator (R1) which was directly connected to the input of the low noise amplifier (LNA). The LNA has a gain of 50 dB. The
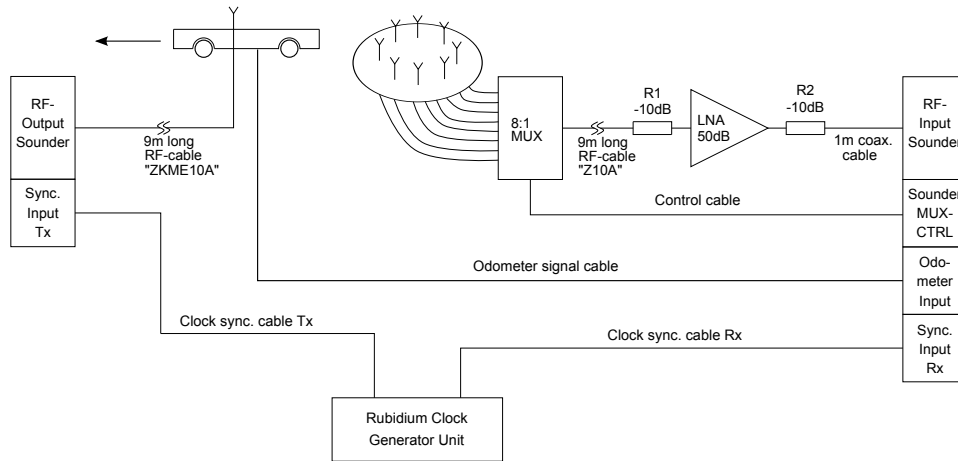
Figure 3.1: Overview of the measurement setup for Tx and Rx.
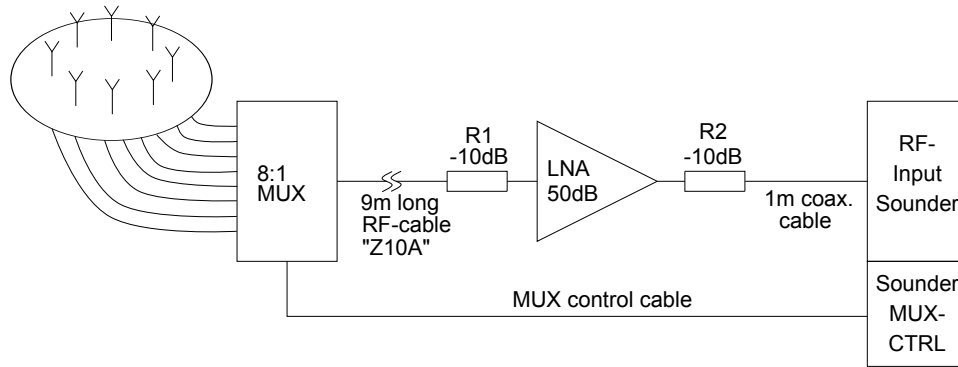
Figure 3.2: Receiver measurement setup.

noise figure of the LNA is about 1.5 dB and the effective bandwidth of the LNA is 120 MHz. The attenuator R1 from Rohde & Schwarz was used to prevent saturation of the LNA input for very short distances between transmitter and receiver. Directly on the output of the LNA was the attenuator R2 similar as R1 from Rohde & Schwarz (10 dB) connected to prevent saturating the RF input of the channel sounder. From R2 a short coaxial cable (1 m) was used to connect to the receiver input of the channel sounder. The attenuator R1 was removed for measurements when the Tx and Rx were separated in different rooms in order to keep a high SNR for those measurements.

3.1.4   Receive Antenna Array and Multiplexer

In Fig. 3.3 is the topview of the receiver array shown. The zero direction of the array is from the center towards antenna 1. The center of the array is the coordinate system. The antennas are equidistantly spaced ($45°$) on a circle with diameter of 75.18 mm. The receiver antenna 1 was connected to multiplexer port 1, antenna 2 to port 2, and so forth for all antennas. The cable connections from the antenna array to the multiplexer are shown in Fig. 3.4c. A laser pointer was mounted on
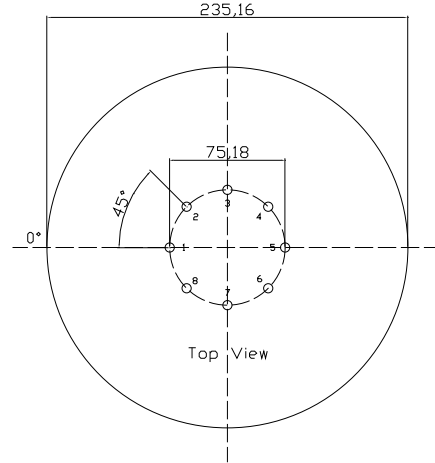
Figure 3.3: Rx antenna array topview. The $0°$ symbol in the drawing marks the $0°$ direction of the antenna array.

the array pointing into the $0°$ direction. This laser pointer was used in order to rotate the array such that the $0°$ direction is parallel to the wall along the corridor (opposite of the windows) as indicated in Fig. 2.2. The antenna array and the multiplexer were mounted on a tripod. A height of either 1.1 m or 1.2 m to the upper edge of the ground plane was used during the measurements.

The utilized time division multiplexer was manufactured by VAD GmbH in Dresden, Germany. This multiplexer contains a 8-of-1 pin diode switch with impedance matching inputs. In other words, if one antenna (channel) is switched on, thus connected to the out gate, the other seven antennas (channels) are closed and loaded with 50 Ω. The matched impedance at off-channels with 50 Ω ensures that there are no reflections from these antennas. A validation test on the multiplexer in the lab at DLR confirms the specifications of the multiplexer datasheet described above.

Antenna Array Calibration

Generally, if the array's position is known, with a sufficient amount of measured steering vectors, it is possible to identify the antenna calibration matrix and multiplicative constants by solving the nonlinear least squares problem.

The calibration for the antenna array is performed in a free space like environment at DLR. Referred to the carrier frequency, a narrow band signal was transmitted through a non-reflecting propagation channel. This means only one LoS path is expected during the calibration measurement. The environment ensures far field waves impinging on the antenna array, and mainly only one line of sight component exits. The transmit antenna and receive antenna were approximately 20 mseparated from each other.

Fig. 3.5 gives the definition of the incoming angles utilized in the calibration measurement. The arrow in the plot represents the impinging wave, and the corresponding azimuth angle α and elevation angle β definitions for the provided coordinate system are depicted. During the calibration measurement, the antenna array

(a)

(b)

(c)

Multiplexer

(d)
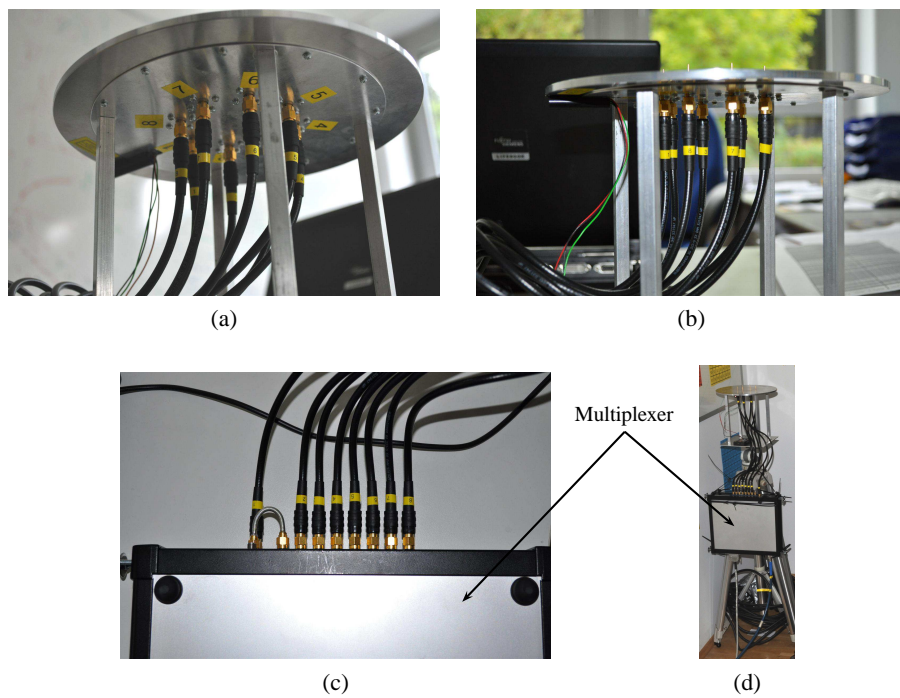
Figure 3.4: (a) connection of the cables and the antennas shown from the bottom of the array; (b) view from the side of the array and cables; subref-fig:switchrxantcables connection of the cables to the multiplexer; (d) to the left, the multiplexer and receiver antenna array on the tripod - to the right the model train with the transmit tower.
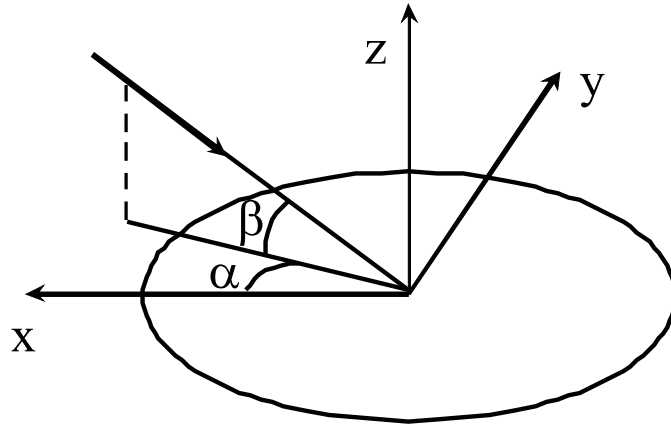
Figure 3.5: Definition of the incoming angles.
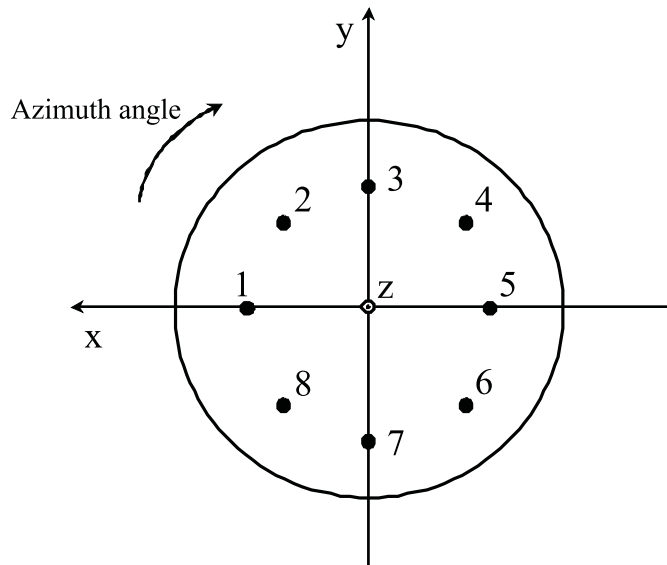
Figure 3.6: Rotation of antenna array to change the incoming azimuth angle.

was rotated in vertical plane with 5° steps to change the incoming azimuth angle. The array was rotated in the horizontal plan in 5° steps to change the incoming elevation angle as shown in Fig. 3.6 and Fig. 3.7. The azimuth angle was taken from 0 to 355°. For each azimuth angle, the antenna array was rotated in elevation from 0 to 90°.

3.1.5 Transmit Antenna

Transmit antenna: Huber&Suhner Type SOA 5600/360/3/20/V_1 [1] mounted on a circular groundplane of diameter 235.16 mm. The antenna was mounted on the tower of the model train at a height of 1.26 m measured from the floor to the upper edge of the groundplane.
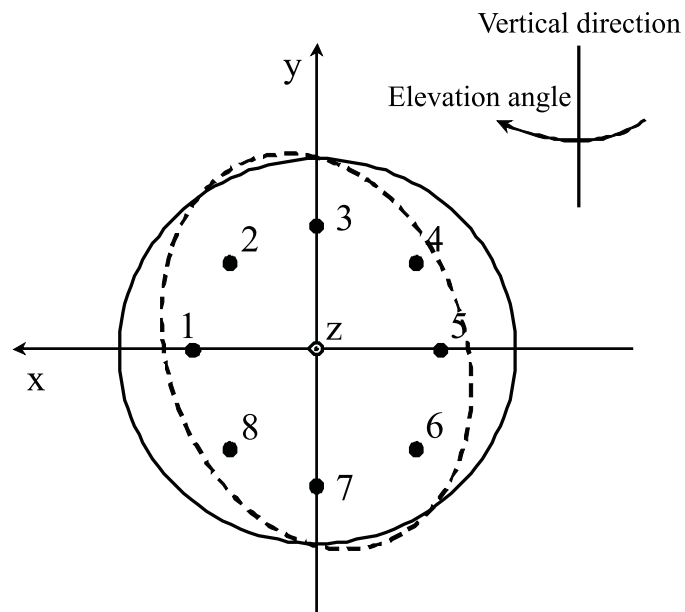
Figure 3.7: Rotation of antenna array to change the incoming elevation angle.

(a) (b)
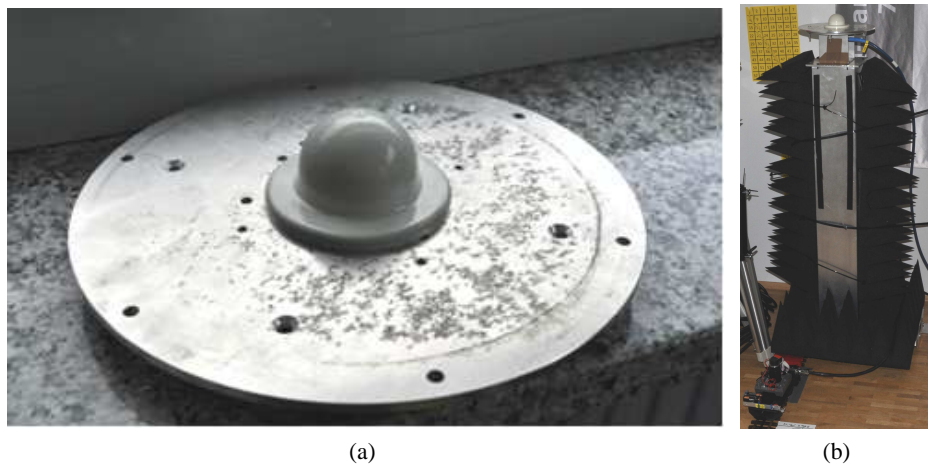
Figure 3.8: (a) shows the Hubner&Suhner transmit antenna mounted on the groundplane disc. (b) shows the transmit antenna mounted on the tower of the model train at the height of 1.26 metre.

3.2 Sounder Settings

In Table 3.2 are the used sounder settings summarized.

3.2.1 Sounding Signal

The duration of the sounding signal is $T_{\text{Tx}} = 12.8\,\mu\text{s}$. The measurement bandwidth is 120 MHz, with $N_c = 1536$ frequency tones. The inter-tone spacing is 78.125kHz.

3.2.2 Sounding Mode

The sounder was operating in the Fast Doppler (FD) and time grid mode. The timing scheme of the sounder is shown in Fig. 3.9.

The duration of the sounding pulse is denoted by T_{Tx}. The multiplexer sequentially switches the N_{Rx} elements of the receive antenna array. For each element measured, two sounding pulses are transmitted, thus the time duration T_{Rx} between the start of the measurement of two antenna elements is

$$T_{\text{Rx}} = 2 \cdot T_{\text{Tx}} \tag{3.1}$$

The time duration of a measurement cycle in which all receive antennas are measured once, is

$$T_{\text{cycle}} = N_{\text{Rx}} \cdot T_{\text{Rx}} = 2N_{\text{Rx}}T_{\text{Tx}} \tag{3.2}$$

In "Fast Doppler mode" the sounder measures a "burst" of N_{burst} cycles consecutively. The duration of one burst is

$$T_{\text{burst}} = N_{\text{burst}} \cdot T_{\text{cycle}} = 2N_{Rx}N_{\text{burst}}T_{\text{Tx}} \tag{3.3}$$

After each burst the sounder stores the recorded data and a break is for data storage is inserted. After the data is stored, the next burst is measured. Thus the time interval between consecutive bursts are

$$T_{\text{rep}} = N_{\text{rep}}T_{\text{burst}} \tag{3.4}$$

$$= 2N_{\text{Rx}}N_{\text{burst}}N_{\text{rep}}T_{\text{Tx}} \tag{3.5}$$

for some constant N_{rep} which is calculated by the sounder based on its hardware constraints.

Let the data acquired during one sensing period of a single antenna element be called a sub-channel sample. Then the ith sample is acquired at center time

$$t_i = (i-1 \mod N_{\text{Rx}}N_{\text{burst}})T_{\text{Rx}} + \left\lfloor \frac{i}{N_{\text{Rx}}N_{\text{burst}}} \right\rfloor T_{\text{rep}}, \qquad i = 1,2,3,\ldots \tag{3.6}$$

The ith sample is acquired from the antenna element with index

$$m(i) = i \mod N_{\text{Rx}}, \qquad i = 1,2,3,\ldots \tag{3.7}$$

During one burst, the transmitter moves

$$d_{\text{burst}} = v_{\text{Tx}}T_{\text{burst}} \approx 0.0035\lambda, \tag{3.8}$$

and in between each burst it moves

$$d_{\text{rep}} = v_{\text{Tx}}T_{\text{rep}} \approx \frac{\lambda}{8.8}. \tag{3.9}$$

Table 3.1: Timing Scheme Settings

Parameter	Symbol	Value
Number of receive antennas	N_{Rx}	8
Number of cycles per burst	N_{burst}	20
Number of bursts in the burst repetition time	N_{rep}	32
Transmit pulse length	T_{Tx}	12.8 µs
Interval between consecutive Rx measurements	$T_{\mathrm{Rx}} = 2T_{\mathrm{Tx}}$	25.6 µs
Burst duration	$T_{\mathrm{cycle}} = 16T_{\mathrm{Tx}}$	204.8 µs
Burst duration	$T_{\mathrm{burst}} = 320T_{\mathrm{Tx}}$	4 096 µs
Burst repetition time	$T_{\mathrm{rep}} = 10240T_{\mathrm{Tx}}$	131.072 ms
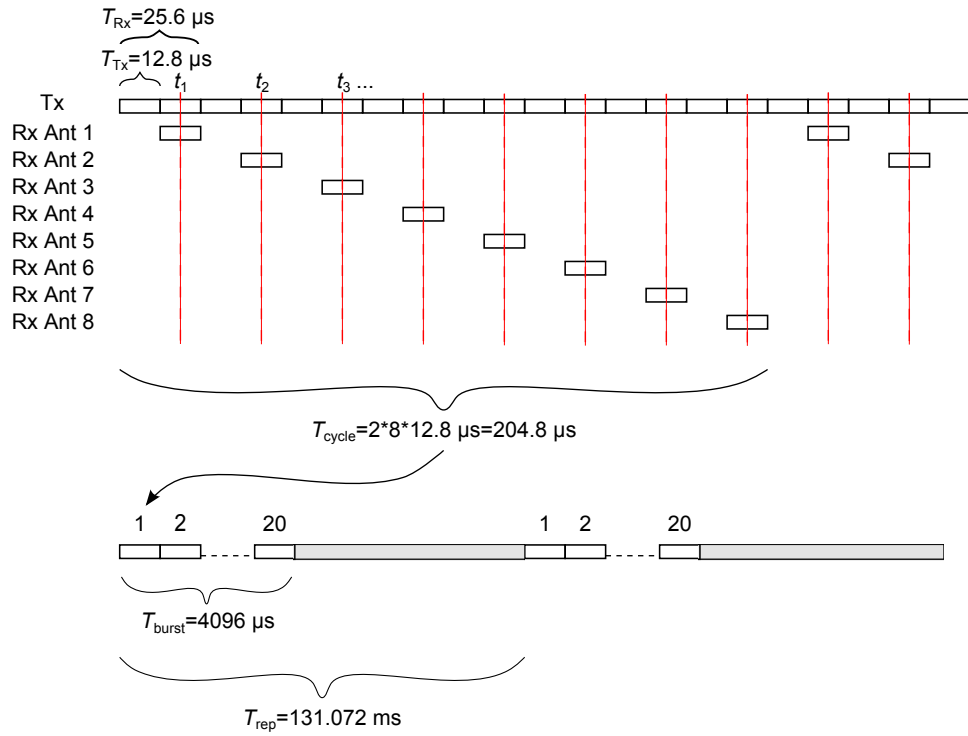
Figure 3.9: Timing schema used for the measurements.

Table 3.2: Setting of the channel sounder.

Parameter	Value
Carrier frequency f_c [GHz]	5.2
Bandwidth B [MHz]	120
Number of sub-carriers N_c	1536
Carrier separation Δf [kHz]	78.125
Tx velocity [m/s]	$\approx$0.05
Odometer pulse correction I_{real}	105212.523942

CHAPTER 4

RECORDING OF SPHERICAL PANOGRAPHS

During the preparation time panographs were made (full 360° in azimuth and full 180° in co-elevation) for all receiver positions at the height of the Rx antennas. The panographs show the whole scene viewed from each of the receiver positions. This allows for overlaying direction estimates on the photos.

One way of creating panographs with $360° \times 180°$ is to use multiple rows and columns of photos to "stitch" one big panograph. The photos should overlap and should have enough features in the overlapping area to align the images in an automatic stitching process. For the purpose of creating a minimal number of images, a very short focal length, resulting in large viewing angles is preferred. We used the website [2] to get the viewing angle for the used focal length and the size of the image sensor of the camera. The viewing angles allow to calculate the number of images needed for the $360° \times 180°$ panograph.

4.1 Equipment and Stitching Software

For the purpose of creating panoramic images, specifically indoors where objects are very close, it is important to align the cameras "nodal" point precisely to the center of rotation. This is important in order to have near and far objects aligned in different images taken from different viewing angles. In case of misalignment ghostly artifacts of the object can appear on different positions in the panograph and the stitching process can fail. Note, in case the focal length on the camera is changed, the nodal point changes too.

In order to mount the camera in its nodal point and to rotate the camera correctly in azimuth and elevation, we used the panorama system VR-System 6/8 from Novoflex (see Fig. 4.1). To find the nodal point of the camera system and to adjust it correctly with the panorama system, we used the method described [3].

The used camera is a Nikon D5000 with a crop factor of 1.5 (image sensor size 15.8×23.6 m^2). The camera was equipped with a AF-S DX Nikkor 18-55 mm

1:3,5-5,6G VR lens system. The focal length of the lens system was set to 18 mm. The resulting field of view is in portrait orientation $47.4° \times 66.7°$. We chose a $30°$ step size in azimuth leading to 40% overlap of the images. In elevation we chose to take 5 rows in total. One row in the azimuth plane ($0°$ elevation) and four rows with $\pm30°$ elevation and $\pm60°$ resulting in approximately 50% overlap.

For the stitching process we used the software "Stitcher Unlimited 2009" from Autodesk. The software allows for the creation of $360° \times 180°$ panographs from multiple rows and columns of images. The software supports multiple output formats. One of the formats creates a panograph with a equi-rectangular coordinate system for azimuth and elevation angles. This allows for easy mapping of e.g. directional Bartlett-spectra on the panograph.

4.2   Calibration and Use of Panographs

For calibration purpose and for stitching purpose colored posters were used. All posters show a numbered grid to assist in the stitching process. The right lower corner of the red posters is used for reference purposes. This corner is at the height of the receive antenna. Furthermore the distances in the room to the right lower corner of the red posters were measured. This allows to calculate reference angels from the receiver position to these posters. In addition known objects or other features (corners) of the room can be used to calculate reference angles. This allows to easily find the $0°$ direction (azimuth and elevation) in the panographs. The stitching software automatically adjusts the elevation angle to zero degree. This angle can be refined with the reference corner of the red posters, if necessary. The $0°$ azimuth is coarsely adjusted with the stitching software based on the known $0°$ direction such that the center of the image corresponds to $0°$ in azimuth and elevation.

After this adjustment in the stitching software we export the panograph in an equi-rectangular coordinate system for azimuth and elevation.

The size of the panograph in pixels corresponds to an image with $\pm180°$ in azimuth and $\pm90°$ in elevation. When importing the image into Matlab we map the image size in pixels to a coordinate system in degrees. A refinement of the $0°$ azimuth direction using the reference points is done by simple shifts of the image. The resulting calibrated images are stored for later use in Matlab with the $0°$ direction in the center of the image. The filenames of the calibrated images for the use in Matlab are listed in Table 4.1. An example image is shown in Fig. 4.2.

Figure 4.1: The panorama system VR-System 6/8 mounted on the tripod in (a) and with the camera in (b),(c), and (d). In (d) the setting of the focal length can be seen.
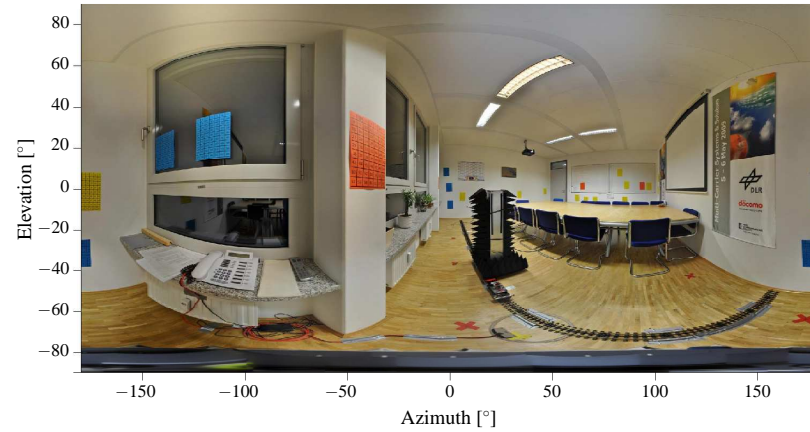
Figure 4.2: Spherical panoramic photo from Rp1 perspective. A equi-rectangular coordinate system for azimuth and elevation is used. The center of the image corresponds to $0°$ in azimuth and elevation.

Table 4.1: Panograph file names.

Receiver Position	Coarse adjustment with high resolution	Calibrated file for Matlab usage
Rp1	rp1_highres.jpg	rp1_matlab.jpg
Rp2	rp2_highres.jpg	rp2_matlab.jpg
Rp3	rp3_highres.jpg	rp3_matlab.jpg
Rp4	rp4_highres.jpg	rp4_matlab.jpg
Rp5	rp5_highres.jpg	rp5_matlab.jpg
Rp6	rp6_highres.jpg	rp6_matlab.jpg
Rp7	rp7_highres.jpg	rp7_matlab.jpg
Rp8	rp8_highres.jpg	rp8_matlab.jpg
Rp9	rp9_highres.jpg	rp9_matlab.jpg

CHAPTER 5

EXPERIMENTS

5.1 Experiments for Validation of In-room Path loss Model

The purpose of these measurements is the evaluation of the in-room reverberant channel model. For this evaluation it is necessary to have measurements with distances between Tx and Rx ranging from the smallest possible distance to the largest distance possible in the room. Thus the Rx is positioned in the room corners and the tracks for the Tx pass closely by the Rx. By choosing at the Rx a circular antenna array and placing the Tx on the model train, spatial averaging is possible for the evaluation of the path loss model. Furthermore the use of the circular array allows the creation of virtual Rx antenna patterns in order to evaluate the differences for localization with different virtual Rx antenna orientations.

5.1.1 Experiment 1.1: Noise Measurement

This experiment consists of a short measurement where the Tx is switched off and only "noise" at the receiver is measured. This should provide information on any present interference from e.g. the WiFi networks and allows to estimate the noise level. This obtained noise level might be different from the one later during the measurements due to the maximum dynamic range of the system.

5.1.2 Experiment 1.2: Path loss measurements for Rp1 to Rp9

For each of the indicated receiver position Rp1 to Rp9 are measurements conducted when the model train (transmitter) moves along the tracks T1 and T2. No people are in R4. People are working in R2 and R3. The used Tx tower height is 1.3 m.

5.1.3 Experiment 1.3: Static Measurements

Four static measurements for the receiver position Rp4 are conducted. The four positions of the transmitter are the start and end points of track T1 and track T2.

These measurements are control measurements to see if the environment can be considered static.

5.2   Reverberation Effect Experiments

In this experiment we conduct measurements with open windows or people present in the room. The windows are metal coated and when they are opened we expect a different reverberation in the room. By opening the windows we alter one wall of the room from low "absorption" (strong reflections from the windows) to high "absorption" coefficients (no reflections from the open window). Thus a lower power level for the reverberant field is expected.

The inner-walls of the building are drywalls and their attenuation (absorption) is unknown. It is unclear if the observed reverberation effect in the meeting room is generated by the room itself or by the larger structure of the building. If a change in the reverberation due to opening the windows in the neighboring rooms is observed, we conclude that the larger structure of the building creates the reverberation effect.

The underlying idea of the reverberation is based on reflections in the room with an average absorption coefficient. By adding persons to the room, the average absorption coefficient should change, thus the reverberation effect should change. We make the hypothesis that this alters the reverberant field in the room.

5.2.1   Experiment 2.1: Open Windows in Room R4

We use for the measurements track T1 for the transmitter. The receiver locations are Rp1 to Rp4. We conduct multiple measurements with different number of open windows until all windows in the room are open.

5.2.2   Experiment 2.2: Open Windows in Room R2 to R4

All windows in rooms R2, R3 and R4 are opened and we conduct measurements for the receiver locations Rp2 to Rp4 and the transmitter moving along track T1.

5.2.3   Experiment 2.3: Absorption of Human Bodies in the Room

Measurements are conducted with people in the meeting room sitting around the conference table. The receiver positions Rp2 to Rp4 are used for tracks T1.

5.3   Cooperative Localization Experiments

The purpose of these measurements is to provide measurement data for analyzing the multi-link radio channel for localization purposes. In room R4 the measurements are conducted for line of sight situations. Additional measurements from the neighboring rooms R2 and R3, corresponding to non-line of sight situations, are conducted as well.

5.3.1   Experiment 3.1: Cooperative Localization

Los Multi-link Measurements: Room R4 covers a scenario with only cooperative LoS links. We use the train track T1 with Rp1 and Rp2 and vice versa T2

with Rp3 and Rp4 from the experiment described in Section 5.1.2. This set is extended by five additional points on the opposing track. The train track T[1,2] and the T[1,2]_P[1..5] points were all measured with the same antenna height. With this we can investigate a mirroring effect as both measurements have the same conditions with the same sampling distances on both sides. The measurements for the points Rp[1..5] provide the possibilities to use a set of reference points for modeling anchors with perfect position information.

NLoS Multi-link Measurements: In room R3 a 3rd track and two more additional reference points (Rp6 and Rp7) are added. The 3rd track T3 allows to measure NLoS effects for the cooperative links established in room R4 together with a robust approach by using distance-based measurements. The robust approach is guaranteed as the geometrical constellation of the tracks (T3 vs. T[1,2]) is orthogonal to each other. The additional reference points Rp6 and Rp7 have LoS conditions to the track T3 to differ between having only LoS (R3) and NLoS (R4). This is further extended to room R2 and the points Rp8 and Rp9. The link between track T3 and Rp8 can be considered as strong NLoS (weak LoS) case, as the material in between transmitter and receiver is not concrete. The link between track T3 and Rp9 is blocked by a metallic white board and thus a weak NLoS link is expected.

5.4 Fluorescent Tube Experiment

5.4.1 Experiment 4.1: Fluorescent Tube

In previous measurement campaigns was reported that switched on fluorescent tubes create a time varying channel. An experiment at fixed transmitter and receiver positions is conducted to test this phenomenon in the given environment. The continuous radio channel is measured. In the few first seconds of the measurements, the fluorescent tubes are switched off and after a couple seconds the fluorescent tubes are switched on.

5.5 Measurement Protocol

In the following we summarize the measurement process and note exceptions which happened during the experiments. We refer the reader to Fig. 2.2, which shows a schematic of the measurement environment and to Fig. 4.2 showing a spherical panorama image from Rp1. The measurements are identified as scenarios numbered from 0.00 to 6.03, for practical reasons. Scenarios can be part of multiple experiments. A mapping of the scenarios to the corresponding experiments can be found in Table 5.1.

5.5.1 Measurement of Noise (Experiment 1.1)

A measurement of the noise was conducted before the measurements of the different scenarios were done. The measurement was conducted with the receiver at Rp4

and with the transmitter at the start position of T1. The main goal of this measurement was to see the input on the receiver when the transmitter is turned off. This should help to identify if there are any WiFi networks transmitting and if there are any other disturbing sources in the measured band width. Furthermore it should provide an indication of the noise power. Before this measurement was recorded, a detailed check of the noise power, the signal power and the AGC settings was done. Adjustments such as adding the LNA and tests with different attenuators were conducted to optimize for the full range of the AGC and to achieve as much SNR over all transmitter and receiver positions as possible.

Table 5.1: Mapping of Scenarios to Experiments.

Scen. #	Filename	Exp. 1.1: Noise	Exp. 1.2: Path loss	Exp. 1.3: Static	Exp. 2.1: Open windows in R4	Exp. 2.1: Open windows in R2 to R4	Exp. 2.1: Human absorption	Exp. 3.1: Coop. localization	Exp. 4.1: Fluorescent tubes
0.00	AAUDLR2010_noise_01	x							
1.01	AAUDLR2010_01_01_T1_Rp1		x	x					
⋮	⋮		⋮	⋮					
1.09	AAUDLR2010_01_09_T1_Rp9		x	x					
1.10	AAUDLR2010_01_10_T1_T2p1							x	
⋮	⋮							⋮	
1.14	AAUDLR2010_01_14_T1_T2p5							x	
2.01	AAUDLR2010_02_01_T2_Rp1		x	x					
⋮	⋮		⋮	⋮					
2.09	AAUDLR2010_02_09_T2_Rp9		x	x					
2.10	AAUDLR2010_02_10_T2_T1p1							x	
⋮	⋮							⋮	
2.14	AAUDLR2010_02_14_T1_T1p5							x	
3.01	AAUDLR2010_03_01_T3_Rp1							x	
⋮	⋮							⋮	
3.9	AAUDLR2010_03_20_T3_Rp9							x	
3.10	AAUDLR2010_03_10_T3_T1p1							x	
⋮	⋮							⋮	
3.14	AAUDLR2010_03_14_T3_T1p5							x	
3.15	AAUDLR2010_03_15_T3_T2p1							x	
⋮	⋮							⋮	
3.19	AAUDLR2010_03_19_T3_T2p5							x	
3.20	AAUDLR2010_03_20_T3_Rp6								x
4.01	AAUDLR2010_04_01_T1_Rp1						x		
4.02	AAUDLR2010_04_02_T1_Rp2						x		
4.03	AAUDLR2010_04_03_T1_Rp3						x		
5.01	AAUDLR2010_05_01_T1_Rp4_win1				x				
⋮	⋮				⋮				
5.04	AAUDLR2010_05_04_T1_Rp4_win1234				x				
5.05	AAUDLR2010_05_05_T1_Rp1_win1				x				
⋮	⋮				⋮				
5.08	AAUDLR2010_05_08_T1_Rp1_win1234				x				
5.09	AAUDLR2010_05_09_T1_Rp2_win1				x				
⋮	⋮				⋮				
5.12	AAUDLR2010_05_12_T1_Rp2_win1234				x				
5.13	AAUDLR2010_05_13_T1_Rp3_win1				x				
⋮	⋮				⋮				
5.16	AAUDLR2010_05_16_T1_Rp3_win1234				x				
6.01	AAUDLR2010_06_01_T1_Rp3_win1to9					x			
6.02	AAUDLR2010_06_02_T1_Rp4_win1to9					x			
6.03	AAUDLR2010_06_03_T1_Rp2_win1to9					x			

Table 5.2: Noise Measurement for Experiment of Section 5.1.1 .

Scen. # 0.00	Tx Track	Rx Pos.	Comments	Calibration File (suffix ".KOR")	Filename (suffix ".000.DLR1_DSK")
0.00	T1	Rp4	[1]	AAUDLR2010_cal_01	AAUDLR2010_noise_01

Comments:

[1] 20 s were recorded with transmitter switched off.

5.5.2 Measurements of Scenario 1

The measurements of scenario 1 consist of all measurements with the transmitter on track T1 with the receiver positions Rp1 to Rp9 and the positions T2Rp1 to T2Rp5. The room was empty and all windows were closed. The measurement team was standing outside in the corridor during the measurement process. The measurements of scenario 1.01 to 1.09 correspond to the experiment described in Section 5.1.2. The measurements of scenario 1.09 to 1.14 are intended for co-operative localization experiments and correspond to the experiment described in Section 5.3.

Table 5.3: Measurements for Transmitter on Track T1.

Scen. #	Tx Track	Rx Pos.	Comments	Calibration File (suffix ".KOR")	Filename (suffix ".000.DLR1_DSK")
1.01	T1	Rp1		AAUDLR2010_cal_01	AAUDLR2010_01_01_T1_Rp1
1.02	T1	Rp2		AAUDLR2010_cal_01	AAUDLR2010_01_02_T1_Rp2
1.03	T1	Rp3	[4]	AAUDLR2010_cal_01	AAUDLR2010_01_03_T1_Rp3
1.04	T1	Rp4	[5]	AAUDLR2010_cal_01	AAUDLR2010_01_01_T1_Rp4
1.05	T1	Rp5	[1],[6]	AAUDLR2010_cal_03	AAUDLR2010_02_05_T1_Rp5
1.06	T1	Rp6	[2]	AAUDLR2010_cal_03	AAUDLR2010_01_06_T1_Rp6
1.07	T1	Rp7		AAUDLR2010_cal_03	AAUDLR2010_01_07_T1_Rp7
1.08	T1	Rp8		AAUDLR2010_cal_03	AAUDLR2010_01_08_T1_Rp8
1.09	T1	Rp9		AAUDLR2010_cal_01	AAUDLR2010_01_09_T1_Rp9
1.10	T1	T2p1		AAUDLR2010_cal_01	AAUDLR2010_01_10_T1_T2p1
1.11	T1	T2p2		AAUDLR2010_cal_01	AAUDLR2010_01_11_T1_T2p2
1.12	T1	T2p3		AAUDLR2010_cal_01	AAUDLR2010_01_12_T1_T2p3
1.13	T1	T2p4		AAUDLR2010_cal_01	AAUDLR2010_01_13_T1_T2p4
1.14	T1	T2p5		AAUDLR2010_cal_01	AAUDLR2010_01_14_T1_T2p5

Comments:

[1] All measurements with Rp5 were measured at the end of the Tx T1 and T2 measurements, because the Rx needed to be moved from tripod to the table.

[2] Was measured after all measurements in R4 with T1 and T2 were finished.

[3] Change of the Rx height from 110 cm to 120 cm.

[4] Plastic strips mounting the Rx antenna MUX loosened. It needed to be tightened again. New stronger plastic strips were used.

[5] Scenario 1.04 was saved with the wrong file name. Manual fix afterwards.

[6] Scenario 1.05 was saved with the wrong filename. Manual fix afterwards.
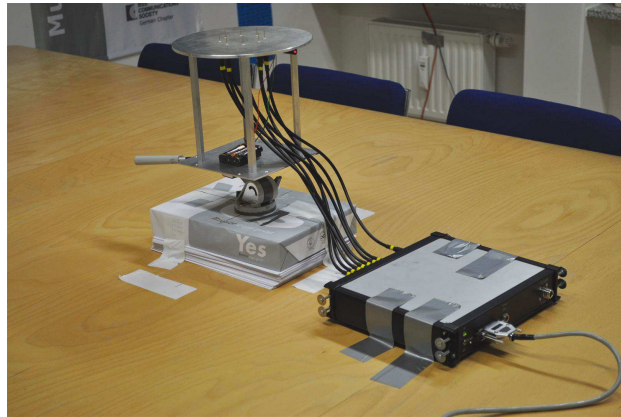
Figure 5.1: Mounting of the Rx array and the multiplexer on the table for the receiver position Rp5.

5.5.3 Measurements of Scenario 2

The measurements of scenario 2 consist of all measurements with the transmitter on track T2 with the receiver positions Rp1 to Rp9 and the positions T1Rp1 to T1Rp5. The room was empty and all windows were closed. The measurement team was standing outside in the corridor during the measurement process. The measurements of scenario 2.01 to 2.09 correspond to the experiment described in Section 5.1.2. The measurements scenario 2.09 to 2.14 are intended for cooperative localization and are described in Section 5.3.

Table 5.4: Measurements for Transmitter on Track T2.

Scen. #	Tx Track	Rx Pos.	Comments	Calibration File (suffix ".KOR")	Filename (suffix ".000.DLR1_DSK")
2.01	T2	Rp1		AAUDLR2010_cal_02	AAUDLR2010_02_01_T2_Rp1
2.02	T2	Rp2		AAUDLR2010_cal_02	AAUDLR2010_02_02_T2_Rp2
2.03	T2	Rp3		AAUDLR2010_cal_02	AAUDLR2010_02_03_T2_Rp3
2.04	T2	Rp4		AAUDLR2010_cal_02	AAUDLR2010_02_04_T2_Rp4
2.05	T2	Rp5		AAUDLR2010_cal_03	AAUDLR2010_02_05_T2_Rp5
2.06	T2	Rp6		AAUDLR2010_cal_03	AAUDLR2010_02_06_T2_Rp6
2.07	T2	Rp7		AAUDLR2010_cal_03	AAUDLR2010_02_07_T2_Rp7
2.08	T2	Rp8		AAUDLR2010_cal_03	AAUDLR2010_02_08_T2_Rp8
2.09	T2	Rp9		AAUDLR2010_cal_02	AAUDLR2010_02_09_T2_Rp9
2.10	T2	T2p1		AAUDLR2010_cal_02	AAUDLR2010_02_10_T2_T1p1
2.11	T2	T2p2		AAUDLR2010_cal_02	AAUDLR2010_02_11_T2_T1p2
2.12	T2	T2p3		AAUDLR2010_cal_02	AAUDLR2010_02_12_T2_T1p3
2.13	T2	T2p4		AAUDLR2010_cal_02	AAUDLR2010_02_13_T2_T1p4
2.14	T2	T2p5		AAUDLR2010_cal_02	AAUDLR2010_02_14_T2_T1p5

Comments:

Track T2 is longer than T1. The measurement files are approximately 60 s long.

Figure 5.2: Panograph from Rp1 perspective showing track T2, the train and the antenna tower.

5.5.4 Measurements of Scenario 3

All measurements of scenario 3 are with the transmitter on track T3 with the receiver positions Rp1 to Rp9, T1Rp1 to T1Rp5 and the positions T2Rp1 to T2Rp5. The room was empty and all windows were closed. The measurement 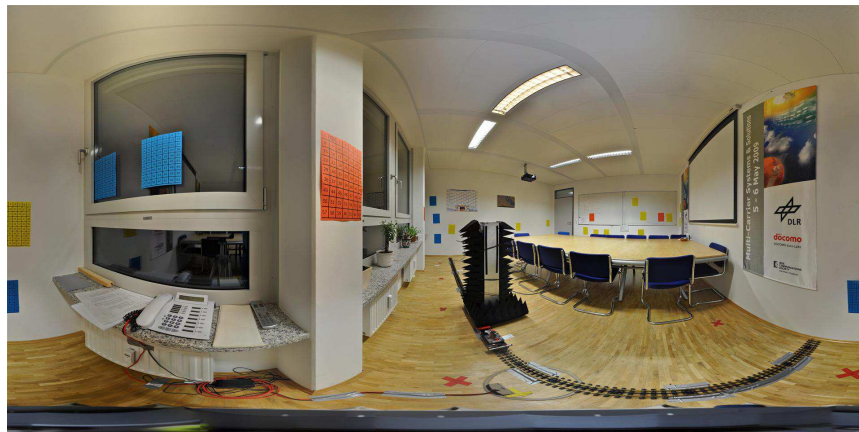team was standing outside in the corridor during the measurement process. The measurements of scenario 3 are intended for cooperative localization and their purpose is described in Section 5.3.

Furthermore the measurement of scenario 3.20 was a measurement with the Tx standing at the end of track T3. In this measurement the lights (fluorescent tubes) were in the beginning switched of and after approximately 20 seconds switched on. This measurement corresponds to experiment 4.1 described in Section 5.4.1.

Table 5.5: Measurements for Transmitter on Track T3.

Scen. #	Tx Track	Rx Pos.	Comments	Calibration File (suffix ".KOR")	Filename (suffix ".000.DLR1_DSK")
3.01	T3	Rp1		AAUDLR2010_cal_05	AAUDLR2010_03_01_T3_Rp1
3.02	T3	Rp2		AAUDLR2010_cal_05	AAUDLR2010_03_02_T3_Rp2
3.03	T3	Rp3		AAUDLR2010_cal_05	AAUDLR2010_03_03_T3_Rp3
3.04	T3	Rp4		AAUDLR2010_cal_05	AAUDLR2010_03_04_T3_Rp4
3.05	T3	Rp5		AAUDLR2010_cal_04	AAUDLR2010_03_05_T3_Rp5
3.06	T3	Rp6		AAUDLR2010_cal_06	AAUDLR2010_03_06_T3_Rp6
3.07	T3	Rp7	[1]	AAUDLR2010_cal_06	AAUDLR2010_03_07_T3_Rp7
3.08	T3	Rp8		AAUDLR2010_cal_05	AAUDLR2010_03_08_T3_Rp8
3.09	T3	Rp9		AAUDLR2010_cal_05	AAUDLR2010_03_09_T3_Rp9
3.10	T3	T1p1		AAUDLR2010_cal_05	AAUDLR2010_03_10_T3_T1p1
3.11	T3	T1p2		AAUDLR2010_cal_05	AAUDLR2010_03_11_T3_T1p2
3.12	T3	T1p3		AAUDLR2010_cal_05	AAUDLR2010_03_12_T3_T1p3
3.13	T3	T1p4		AAUDLR2010_cal_05	AAUDLR2010_03_13_T3_T1p4
3.14	T3	T1p5		AAUDLR2010_cal_05	AAUDLR2010_03_14_T3_T1p5
3.15	T3	T2p1		AAUDLR2010_cal_05	AAUDLR2010_03_15_T3_T2p1
3.16	T3	T2p2		AAUDLR2010_cal_05	AAUDLR2010_03_16_T3_T2p2
3.17	T3	T2p3		AAUDLR2010_cal_05	AAUDLR2010_03_17_T3_T2p3
3.18	T3	T2p4		AAUDLR2010_cal_05	AAUDLR2010_03_18_T3_T2p4
3.19	T3	T2p5		AAUDLR2010_cal_05	AAUDLR2010_03_19_T3_T2p5
3.20	T3	Rp6	[2]	AAUDLR2010_cal_06	AAUDLR2010_03_20_T3_Rp6lights

Comments:
[1] Door to R2 was open.
[2] Measurement with the train at the end of the track. First 20 seconds lights switched off. After 20 seconds lights (flourescent tubes) switched on.

Figure 5.3: Panograph from Rp6 perspective showing the interior of room R3 and track T3.

5.5.5 Measurements of Scenario 4

The measurements of scenario 4 consist of all measurements with the transmitter on track T1 with the receiver positions Rp2 to Rp4. Around the meeting table were 10 people sitting (Fig. 5.4) and all windows were closed. The purpose of the measurements is described in Section 5.2.3.

Table 5.6: Measurements with 10 persons R4.

Scen. #	Tx Track	Rx Pos.	Comments	Calibration File (suffix ".KOR")	Filename (suffix ".000.DLR1_DSK")
4.01	T1	Rp1		AAUDLR2010_cal_02	AAUDLR2010_04_01_T1_Rp2
4.02	T1	Rp2		AAUDLR2010_cal_02	AAUDLR2010_04_02_T1_Rp3
4.03	T1	Rp3		AAUDLR2010_cal_02	AAUDLR2010_04_03_T1_Rp4

Comments:
10 people were sitting in the room around the table. People were asked to not move. No Laptops or any other additional equipment.

Figure 5.4: Ten persons placed around the meeting room table.

5.5.6 Measurements of Scenario 5

The measurements of scenario 5 consist of all measurements with the transmitter on track T1 with the receiver positions Rp1 to Rp4 and open windows. The purpose of the measurements is described in Section 5.2.1. The windows open to the inside (Fig. 5.5) and the frames of the windows are metallic. Notice at receiver position Rp1 is window number 4 and at Rp2 window number 1 above the receiver array when these windows are opened. An influence on the antenna response due to the metallic window frame is expected. The order of opening the windows at position Rp2 was changed as compared to the other measurements. The intention was that only when all 4 windows are open, window 1 is above Rp2.

Table 5.7: Measurements with open windows.

Scen. #	Tx Track	Rx Pos.	Comments	Calibration File (suffix ".KOR")	Filename (suffix ".000.DLR1_DSK")
5.01	T1	Rp4	[1]	AAUDLR1010_cal_02	AAUDLR2010_05_01_T1_Rp4_win1
5.02	T1	Rp4	[2]	AAUDLR1010_cal_02	AAUDLR2010_05_02_T1_Rp4_win12
5.03	T1	Rp4	[3]	AAUDLR1010_cal_02	AAUDLR2010_05_03_T1_Rp4_win123
5.04	T1	Rp4	[4]	AAUDLR1010_cal_02	AAUDLR2010_05_04_T1_Rp4_win1234
5.05	T1	Rp1	[1]	AAUDLR1010_cal_02	AAUDLR2010_05_05_T1_Rp1_win1
5.06	T1	Rp1	[2]	AAUDLR1010_cal_02	AAUDLR2010_05_06_T1_Rp1_win12
5.07	T1	Rp1	[3]	AAUDLR1010_cal_02	AAUDLR2010_05_07_T1_Rp1_win123
5.08	T1	Rp1	[4]	AAUDLR1010_cal_02	AAUDLR2010_05_08_T1_Rp1_win1234
5.09	T1	Rp2	[5]	AAUDLR1010_cal_02	AAUDLR2010_05_09_T1_Rp2_win4
5.10	T1	Rp2	[6]	AAUDLR1010_cal_02	AAUDLR2010_05_10_T1_Rp2_win34
5.11	T1	Rp2	[7]	AAUDLR1010_cal_02	AAUDLR2010_05_11_T1_Rp2_win234
5.12	T1	Rp2	[4]	AAUDLR1010_cal_02	AAUDLR2010_05_12_T1_Rp2_win1234
5.13	T1	Rp3	[1]	AAUDLR1010_cal_02	AAUDLR2010_05_13_T1_Rp3_win1
5.14	T1	Rp3	[2]	AAUDLR1010_cal_02	AAUDLR2010_05_14_T1_Rp3_win12
5.15	T1	Rp3	[3]	AAUDLR1010_cal_02	AAUDLR2010_05_15_T1_Rp3_win123
5.16	T1	Rp3	[4]	AAUDLR1010_cal_02	AAUDLR2010_05_16_T1_Rp3_win1234

Comments:
[1] W1 open.
[2] W1 and W2 open.
[3] W1, W2 and W3 open.
[4] W1, W2, W3 and W4 open.
[5] W4 open.
[6] W3 and W4 open.
[7] W2, W3 and W4 open.

(a)   (b)

Figure 5.5: (a) The receiver is at position Rp1 and W1 to W4 are open. (b) The receiver at position Rp2. The metallic frame of W1 is only approximatly 10 cm above the antenna array.

5.5.7 Measurements of Scenario 6

The measurements of scenario 6 consist of measurements with the transmitter on track T1 with the receiver positions Rp2 to Rp4. The windows W1 to W9 in the rooms R2, R3 and R4 were open during the measurements. The intended use of the measurements is described in Section 5.2.2.

Table 5.8: Measurements with window W1 to W9 open.

Scen. #	Tx Track	Rx Pos.	Comments	Calibration File (suffix ".KOR")	Filename (suffix ".000.DLR1_DSK")
6.01	T1	Rp3		AAUDLR2010_cal_02	AAUDLR2010_06_01_T1_Rp3_win1to9
6.02	T1	Rp4		AAUDLR2010_cal_02	AAUDLR2010_06_02_T1_Rp4_win1to9
6.03	T1	Rp2		AAUDLR2010_cal_02	AAUDLR2010_06_03_T1_Rp2_win1to9

Comments:
The windows in room R2, R3 and R4 were open.

CHAPTER 6

DATA STRUCTURE AND FILE NAMES

6.1 Import of RAW Measurement Data

The descriptions in the previous sections refer to the measurement data in the raw channel sounder format. In order to use this data format a 32 bit Matlab version is necessary to use the MEDAV import functions. DLR's MEDAV sounder uses an older file format which is not compatible with the currently distributed "Hyeff" filters from MEDAV. One can obtain with the "Hyeff" licence the import functions for the DLR sounder, directly from DLR.

6.1.1 Import Functions and Data Formats

In the following we state some example Matlab code to import the measurement data with the Medav functions.

```
[Error, Header] = RSKHead(0,[measurementFolder filename],0 );
[Error, Info] = RSKInfo(0,[measurementFolder filename],0 );
for iLoop=1:Header.DataSets
[Error, Data, Snap] = RSKData(0,[measurementFolder filename],...
        [(iLoop−1)∗Header.SetsPerFDBlock+1 1 iLoop∗Header.SetsPerFDBlock],...
        [257 1 1793], [1 2 3 4 5 6 7 8], [],[],0,[],0 );
[Error, Nav, GPS] = RSKNav(0,[measurementFolder filename],...
        [(iLoop−1)∗Header.SetsPerFDBlock+1:1:iLoop∗Header.SetsPerFDBlock],0 );
end
```

The code above imports in every iteration one burst of data with the `RSKData()` function. The function uses a vector specifying the measurement cycles to import. We specify this vector in Matlab as
`[(iLoop-1)*Header.SetsPerFDBlock+1 1 iLoop*Header.SetsPerFDBlock]`
to import all cycles with the burst index `iLoop`. In the raw data file and for the used measurement settings consists each measured frequency response of 2048 samples from which only a part is non zero. We obtain the non zero part with the vector `[257 1 1793]`, which specifies the first frequency sample (257), the step size in

Table 6.1: Data fields of the "Header" structure.

Fieldname	Value
DataSets	7140
Channels	8
FDDChannels	1
MeasureMode	2
MeasureModeText	'Time grid mode'
FDDMode	0
FDDModeText	'FDD disabled'
Periode	2048
TxCount	1
Grid	131.0720
Bandwidth	120000000
RF	5.2000e+009
FDD-RF	[250000000 250000000]
IF	80000000
SampleFreq	320000000
FDBlocksPerDBlock	1
SetsPerFDBlock	20
PreProcessing	1
PreProcessingText	'Rowdata whithout preprocessing'
OdometerPulses	100000
NavDataSource	0
NavDataSourceText	'Receiver unit'
CalibTxPower	0
CalibAGC	87
CalibAttenuation	33
CalibFactor	0
MeasTxPower	0

samples (1) and the last sample (1793) out of the 2048. The measured receive antennas are selected with the vector [1 2 3 4 5 6 7 8]. The size of the "Data" variable is $N_{\text{burst}} \times N_{\text{c}} \times N_{\text{Rx}}$ ($20 \times 1537 \times 8$). For a detailed overview of the function description we refer to the headers in the source code of the import functions. The fields of the other data structures are listed in Table 6.1, Table 6.2, and Table 6.3.

6.2   Detection of Erroneous Frequency Responses

Using long cables to the antenna multiplexer creates random distortions in the measured frequency responses. The frequency responses with such distortions need to be detected automatically such that one can decide to include these data or not. We observe these distortions as a drop in the power of the frequency response for some arbitrary frequency ranges. The size of these frequency ranges and their locations in the considered bandwidth is random over the different measured frequency responses.

During our measurements were no moving objects in the room and the transmitter moved only 0.0035λ during one burst. Thus we assume that the measured frequency responses of N_{burst} is constant at each antenna. In order to detect the frequency distortions from the antenna multiplexer we compare each measured frequency response to an averaged frequency response. We represent the measured frequency response as $H_{i,j}(f)$ where $j = 1 \ldots N_{\text{Rx}}$ is the index for the number of receive antennas and $i = 1 \ldots N_{\text{burst}}$ is the index of the cycles in a burst. We calculate

Table 6.2: Data fields of the "Info" structure.

Fieldname	Value
MeasFileName	'D:\RUSKData\Data\WHERE2_01_01_T1_Rp1.000.DLR1_DISK'
CalibFileName	'D:\RUSKData\Calibration\Where2_cal_01KOR'
StartTime	'02.01.1999; 04:28:10'
EndTime	'02.01.1999; 04:28:59'
MeasPlace	''
MeasSeries	''
MeasLeader	''
TxUnit	''
TxAntenna	'RUSK DLR 1.51 GHz 1x1-Tx-antenna (Id=1050, SNr. 24547)'
TxPosition	''
RxUnit	''
RxAntenna	'RUSK DLR external multiplexer 8 times, f=1..5.3GHz, Pmax=2W, Serial number 33563, Id=9050'
RxPosition	''
Comment1	''
Comment2	''
Comment3	''
Comment4	''
Comment5	''
Scenario	[49x1 struct]

Table 6.3: Data fields of the "Nav" structure.

Fieldname	Value
Number	[1 2 3 4 5 6 7 8 9 10 11 12 13 14 15 16 17 18 19 20]
RelTime	[0 0 0 0 0 0 0 0 0 0 0 0 0 0 0 0 0 0 0 0]
Time	[0 0 0 0 0 0 0 0 0 0 0 0 0 0 0 0 0 0 0 0]
Distance1	[1x20 double]
Distance2	[0 0 0 0 0 0 0 0 0 0 0 0 0 0 0 0 0 0 0 0]

the average frequency response for the j antenna in a burst as

$$\widehat{H}_j(f) = \frac{1}{N_{\text{burst}}} \sum_{i=1}^{N_{\text{burst}}} H_{i,j}(f). \tag{6.1}$$

We use these averaged frequency responses for each antenna to calculate the error between the averaged frequency responses and the frequency responses of each cycle in the burst as

$$\widehat{e}_{i,j}(f) = H_{i,j}(f) - \widehat{H}_j(f). \tag{6.2}$$

Furthermore we estimate the sample based standard deviation of the absolute values of the error over the measurement bandwidth as

$$\widehat{\sigma}_{i,j} = \sqrt{\frac{1}{N_c} \sum_f \left(|\widehat{e}_{i,j}(f)| - \frac{1}{N_c} \sum_f |\widehat{e}_{i,j}(f)| \right)^2}. \tag{6.3}$$

For the case the frequency responses of one antenna in a burst are not distorted, varies the standard deviation of the errors only due to measurement noise. If a distortion of a frequency response occurred is the standard deviation of the errors larger. We chose a threshold to detect distorted frequency responses. The threshold is calculated as the product of some constant value q and the minimum standard deviation of the error in a burst for each antenna. Thus we achieve the index set

$D_{i,j}$ of distorted frequency responses as

$$D_{i,j} = \mathbb{1}(\widehat{\sigma}_{i,j} > q \min_i \widehat{\sigma}_{i,j}), \tag{6.4}$$

where $\mathbb{1}$ is the indicator function. We obtain for each burst such an index $D_{i,j}$ set.

6.3 Measurement Data in Matlab Format

The mentioned import functions in Section 6.1 for the channel sounder data only work in specific 32 bit Matlab versions running on Windows. In order to allow for the use of the measurement data in 64 bit Matlab versions and on Linux systems are the data files converted in Matlab data files. The filenames are the same as the raw data files except that the suffix ".000.DLR1_DSK" is replaced by the file ending ".mat".

The data contained in these files are the "Header" and "Info" structures. In addition are the frequency responses of each burst stored in their own variable (eg. "Data0000001",...,"Data0001000"). This allows for easy access to specific bursts and not opening the complete data at once, which would results in huge memory consumption. Additionally are to each burst the indices of the detected distorted frequency responses saved. For the threshold we chose the value $q = 1.2$, based on some experimental tests. These indices are stored as logical variables and denoted eg. "IndexGood0000001" or "IndexBad0000001" for the good and bad indices of burst one. Similarly, for each burst are the "Gps" and "Nav" structures stored with the corresponding indices, eg. as"Gps0000001" and "Nav0000001".

BIBLIOGRAPHY

[1] Huber+Suhner, "Datasheet for Sencity Antenna For In-Carriage Wireless Communication, Type: SOA 5600/360/3/20/V_1," Document No. 01.02.1358, May 2007.

[2] S. McHugh, "Panoramic Image Projections," Online.

[3] A. Hamblenne and M. Therer, "The grid, Method for a precise location of the entrance pupil on a DLSR camera," PDF Online, Sept. 2004.

A.2   Outdoor-to-Indoor Channels at 2.45 GHz and 5.2GHz for Geolocation Applications

W. Wang, T. Jost, C. Gentner, A. Dammann, and U. Fiebig. Outdoor-to-Indoor Channels at 2.45 GHz and 5.2 GHz for Geolocation Applications. In *The 5th European Conference on Antennas and Propagation (Eucap)*, Rome, Italy, April 2011.

Outdoor-to-Indoor Channels at $2.45\,\mathrm{GHz}$ and $5.2\,\mathrm{GHz}$ for Geolocation Applications

Wei Wang, Thomas Jost, Christian Gentner, Armin Dammann, and Uwe-Carsten Fiebig

German Aerospace Center (DLR)

Institute of Communications and Navigation

Oberpfaffenhofen, 82234 Wessling

Wei.Wang@dlr.de

Abstract—**Time Based (TB) localization in terrestrial mobile radio as an augmentation for global navigation satellite systems has recently gained plenty of interests. As an essential tool to develop suitable algorithms for positioning applications in mobile radios, channel models for wireless transmissions have growing significance. Currently there is a lack of investigations on comparing the propagation characteristics at $2.45\,\mathrm{GHz}$ and $5.2\,\mathrm{GHz}$ for positioning applications. Therefore, we present a statistic evaluation based on a channel measurement campaign. Several propagation characteristics are researched like the received power and the delay spread. While some measures like the received power is carrier frequency dependent, most of the measures like the non line-of-sight bias or the delay spread are independent of this measurement parameter. Instead they are more influenced by the location and the environment.**

I. INTRODUCTION

Global Navigation Satellite Systems (GNSSs) such as the Global Positioning System (GPS) provide very accurate positioning as long as line-of-sight (LoS) conditions between satellites and receiver prevail. However, in critical scenarios like urban canyons, the position accuracy by GNSSs very much deteriorates due to shadowing, diffraction, and reflection of satellite signals. In indoor environment GNSS receivers suffer from severe multipath effects, signal blockage resulting in very low receive power handicapping the tracking of satellite signals.

Augmenting GNSSs based positioning with signals of opportunity helps very much in these environments and improves the position accuracy compared to a GNSS-only solution. The signals of terrestrial mobile radio standards can be exploited in addition to GNSS signals. A promising approach is to apply Time Based (TB) localization to terrestrial radio signals which provide considerably higher received power levels compared to GNSS. In particular we focus our attention on the Long Term Evolution (LTE) system operating at $800\,\mathrm{MHz}$ and $2.6\,\mathrm{GHz}$, and to WIFI networks operating at $2.4\,\mathrm{GHz}$ and $5\,\mathrm{GHz}$. The potential of these signals for localization has been addressed in [1] and [2]. For the LTE system the frequency band at $800\,\mathrm{MHz}$ is used for scenarios with large cell size like in rural areas; the $2.6\,\mathrm{GHz}$ band is foreseen for small and medium cell size scenarios like in urban areas and for femtocells; the $5\,\mathrm{GHz}$ band is another potential center frequency for femtocells. TB localization requires simultaneously receiving signals from several base stations which is critical in rural areas. Therefore, we focus on small cell size scenarios and, in turn, on the $2.6\,\mathrm{GHz}$ and $5\,\mathrm{GHz}$ bands.

The wireless channel has a significant impact on TB localization. The position error is directly related to the range estimation error of individual radio links. Two different major channel characteristics affect the range estimation error: firstly, ranging based on the first detectable wave is positively biased if the Geometric Line-of-Sight (GLoS) path is blocked. This bias, i.e. the difference between the geometrical distance from the transmitter to the receiver and the propagation distance of the first detectable path is known as the non Line-of-Sight (NLoS) bias. Secondly, due to multipath the correlator based synchronizer which is generally used for range estimation is biased positively or negatively by the superposition of paths. So far only few articles on the propagation channel at around $2.4\,\mathrm{GHz}$ and around $5.7\,\mathrm{GHz}$ for outdoor to indoor scenarios have been published, see e.g. [3]. However, these activities have been conducted for communication applications, omitting important measures needed for ranging applications such as the NLoS bias and the spatial correlation characteristics. This paper aims to compare outdoor to indoor broadband wave propagations at $2.45\,\mathrm{GHz}$ and $5.2\,\mathrm{GHz}$ for geolocation applications based on a DLR channel measurement campaign for a time-variant mobile channel.

In Section II, the setup of the channel measurement campaign is addressed. Thereafter, Section III discusses the data processing methods and Section IV the corresponding results including the received power, Root-Mean-Square (RMS) delay spread, and NLoS bias. Section V will conclude this paper and provides an outlook to future work.

II. CHANNEL MEASUREMENT

The measurement was accomplished in the Single Input Single Output (SISO) manner with a MEDAV RUSK broadband channel sounder at the Institute of Communications and Navigation of the German Aerospace Center (DLR) in September 2010. A spread spectrum signal — in particular an Orthogonal Frequency Division Multiplexing (OFDM) signal — has been sent by the transmitter at operating center frequency $2.45\,\mathrm{GHz}$ and $5.2\,\mathrm{GHz}$. The parameter setup of the channel sounder is summarized in Table I.

The transmit antenna depicted on the left side of Fig. 1 was positioned at four different locations referred to as Tx-1 to Tx-

TABLE I
CHANNEL SOUNDER SETUP

	S-Band	C-Band
RF centre frequency	2.45 GHz	5.2 GHz
Bandwidth	90 MHz	90 MHz
Transmit Power	5 W ≅ 37 dBm	5 W ≅ 37 dBm
Signal period	6.4 µs	6.4 µs
Measurement time grid	38.9 ms	38.9 ms
Antennas	Omni-directional (V)	Omni-directional (V)

4 on the rooftop of office building TE02 in a height of $12\,\mathrm{m}$ above ground as shown in Fig. 2. Two other transmit locations Tx-5 and Tx-6 in front of the office building TE01 were used with an antenna height of $2\,\mathrm{m}$ above ground as depicted in Fig. 2. The same antennas at both transmitter and receiver were used for $2.45\,\mathrm{GHz}$ and $5.2\,\mathrm{GHz}$. The transmitter was emitting a signal with a power of $35\,\mathrm{dBm}$ and a rectangular spectral shape of $B = 90\,\mathrm{MHz}$ bandwidth. The transmitted periodic signal was vertical polarized with a repetition rate of $6.4\,\mathrm{µs}$ leading to a maximum resolvable propagation distance of $1.92\,\mathrm{km}$. The channel sounder recorded the Channel Impulse Response (CIR) $h(i,n)$ every $T_g = 38.912\,\mathrm{ms}$, where i denotes the snapshot number and $n = 0,\ldots,N-1$ the delay bin of the CIR at delay $\tau(n) = \frac{n}{B}$. The same Rubidium standard frequency normal was used for both transmitter and receiver clocks to keep them synchronized. The receiver was located inside office building TE01 as shown in Fig. 2. Both buildings TE01 and TE02 can be characterized as standard three story office buildings of concrete with metalized window glass. Our primary goal was is assess the dynamic nature of the channel which is typically experienced by a moving receiver. Thus, instead of static point measurements with a fixed receiver the receiving antenna was mounted on a model train shown on the right side of Fig. 1 moving with a speed of about $0.05\,\mathrm{m/s}$ as described in [4]. For all six transmitter positions, the model train was running on tracks T1 and T2 for both carrier frequency.

Fig. 1. Left plot: transmit antenna located on the rooftop; Right plot: model train including mounted receive antenna

As it was not possible to transmit both frequencies at the same time from the same position, it was necessary to perform measurements for both bands in series. The inter-band switching was done after the model train completed its run on both tracks. The position of the transmitter was pre-
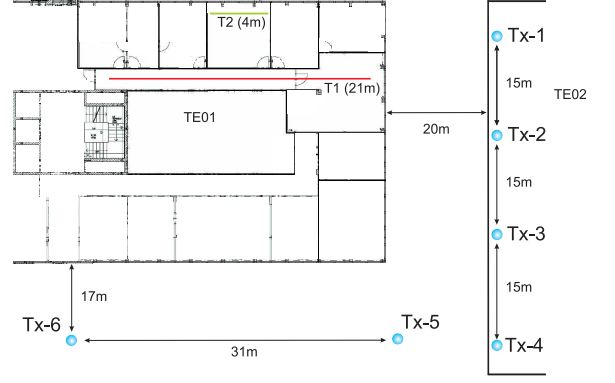

Fig. 2. Measurement Scenarios. Transmit antenna positions Tx-1 to Tx-4 are located on the rooftop, whereas Tx-5 and Tx-6 are located in front of the building. The receiving antenna mounted on the model railway runs along the tracks T1 and T2.

cisely determined using a Leica tachymeter giving a nominal accuracy in the sub-cm domain. To get a similar accuracy for the receiv antenna mounted on the model train, the train run by a cogwheel, is equipped with a rotary encoder giving 500 impulses per motor turn. This results in a precise travelled distance measure for each captured CIR snapshot. More details of the hardware setups are described in [4].

III. DATA PROCESSING AND EVALUATION

To compare the channel characteristics at center frequencies $2.45\,\mathrm{GHz}$ and $5.2\,\mathrm{GHz}$, the normalised received power $P(i)$, RMS delay spread $\sigma(i)$, mean delay $m(i)$, and the NLoS bias $\varepsilon(i)$ are investigated.

Each measured CIR $h(i,n)$ at snapshot i is normalized in power by the free space loss of the GLoS, and shifted in delay such that the first delay bin corresponds to the distance between receiving and transmitting antennas [4]. The normalized CIR is denoted as $h_n(i,n)$ with delay $\tau_n(n)$. The normalised received power $P(i)$ is calculated as

$$P(i) = \sum_{n=0}^{N-1} |h_n(i,n)|^2. \tag{1}$$

The RMS delay spread $\sigma(i)$ is calculated as

$$\sigma(i) = \sqrt{\frac{\sum_{n=0}^{N-1}(\tau_n(n)-m(i))^2 \cdot t\left(|h_n(i,n)|^2\right)}{\sum_{n=0}^{N-1} t\left(|h_n(i,n)|^2\right)}} \tag{2}$$

with the mean delay $m(i)$

$$m(i) = \frac{\sum_{n=0}^{N-1}\tau_n(n)\cdot t\left(|h_n(i,n)|^2\right)}{\sum_{n=0}^{N-1} t\left(|h_n(i,n)|^2\right)}, \tag{3}$$

where $t(x)$ stands for a thresholding function with

$$t(x) = \begin{cases} x & x \geq x_t \\ 0 & \text{otherwise} \end{cases} . \qquad (4)$$

x_t is calculated as the maximum of x minus $20\,\text{dB}$.

For NLoS scenarios, the GLoS path is blocked by buildings, trees or other objects. As a result, its power P_{GLoS} is extremely low, such that it cannot be detected. Hence, the First Detectable Path (FDP) has a larger propagation distance than the GLoS path resulting in a bias for range estimation. The GLoS path delay $\tau^{GLoS}(i)$ for each snapshot i is determined by the measured distance between transmit and receive antennas divided by the speed of light. Therefore, the NLoS bias $\varepsilon(i)$ is calculated as

$$\varepsilon(i) = c \cdot \tau^{FDP}(i) - c \cdot \tau^{GLoS}(i), \qquad (5)$$

where $\tau^{FDP}(i)$ is the delay of the FDP. To estimate $\tau^{FDP}(i)$ super resolution results provided by the Space-Alternating Generalized Expectation-maximization (SAGE) algorithm [5] have been used.

Due to the measurement setup, the accuracy of the position measurement and the size of the antennas the nominal GLoS distance error in the measurement campaign is within cm domain. Nevertheless, several recordings under LoS condition were made for verification and calibration purposes.

IV. CHANNEL CHARACTERISTICS

A. Received Power

Fig. 3 and Fig. 4 show examples of measured CIRs at frequencies $2.45\,\text{GHz}$ and $5.2\,\text{GHz}$ respectively, with the grey line representing the GLoS distance. It can be seen that the CIRs measured at both frequencies show similar trends. At the start of track T1 the receiving antenna was close to the window and the NLoS bias is therefore small. When the receiving antenna was moving on the track T1 into the corridor, the NLoS bias noticeable increase. A clustered structure in the CIR can be seen at both bands. This is most probably caused by reflections between the two buildings TE01 and TE02. Due to the use of metallized window glass, reflections between the two buildings are of high power. The received power normalized to the free space loss is shown in Fig. 5. Due to the normalization of the power the values depicted represent the propagation loss. When the transmit antenna is located at Tx-1 or Tx-2, the electromagnetic waves enter the rooms of TE01 directly through the windows facing TE02. Wave propagation at $5.2\,\text{GHz}$ experiences higher penetration loss by the metalized window glass compared to $2.45\,\text{GHz}$. Whereas the propagation loss at $5.2\,\text{GHz}$ is close to $2.45\,\text{GHz}$ when the transmit antenna is located further away from Tx-1.

B. Time Dispersion Parameters

The statistics for RMS delay spread and mean delay are shown in Fig. 6 to Fig. 9. For the transmit antenna locations Tx-1 to Tx-4 the RMS delay spread and the mean delay slightly decrease. Outdoor reflections showing up as clustered structure in the CIR introduce significant impact on the delay
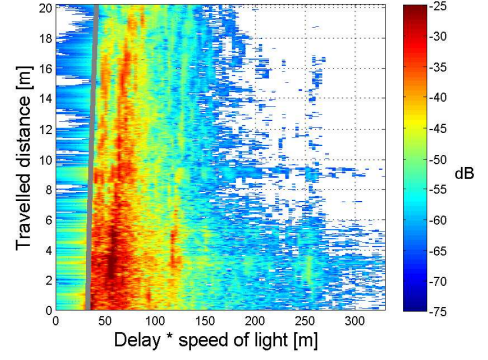

Fig. 3. CIRs normalized in power to the free space loss of the GLoS path for $2.45\,\text{GHz}$ over travelled distance. The grey line represents the GLoS distance. The transmit antenna was located at Tx-5, and the model railway run on track T1.

Fig. 4. CIRs normalized in power to the free space loss of the GLoS path for $5.2\,\text{GHz}$ over travelled distance. The grey line represents the GLoS distance. The transmit antenna was located at Tx-5, and the model railway run on track T1.
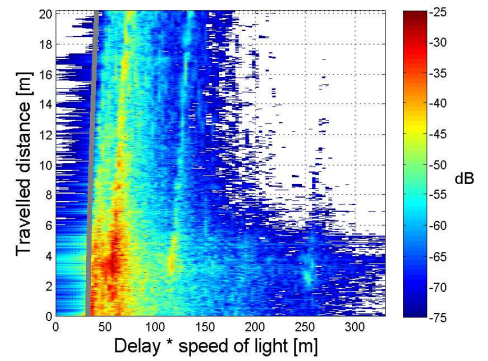

Fig. 5. Normalized received power $P(i)$ in dependence of transmit antenna location and frequency band. The error bars are indicating the standard deviation of the calculated values.

spread. When the transmit antenna location is changed from Tx-1 to Tx-4, the power levels of reflections between both buildings seen at the receiver are reduced due to the change of the impinging angle at TE01. As a result, the delay spread

Fig. 6. RMS delay spread $\sigma(n)$ in dependence of transmit antenna location and frequency band. The error bars are indicating the standard deviation of the calculated values.

Fig. 8. Cumulative density function of calculated RMS delay spread.
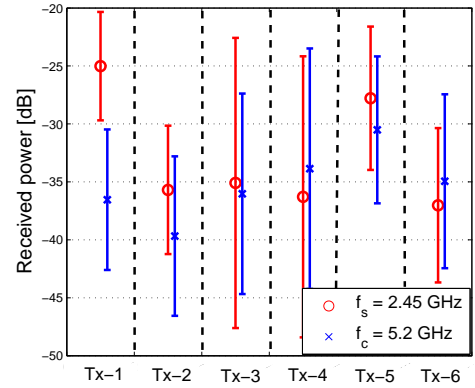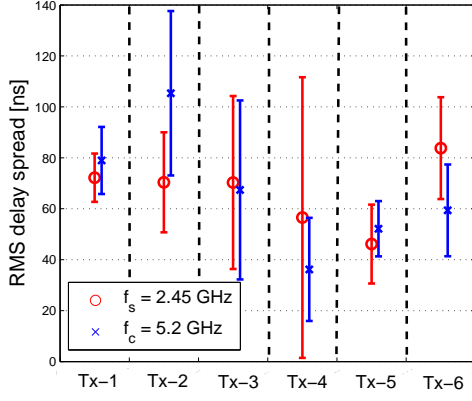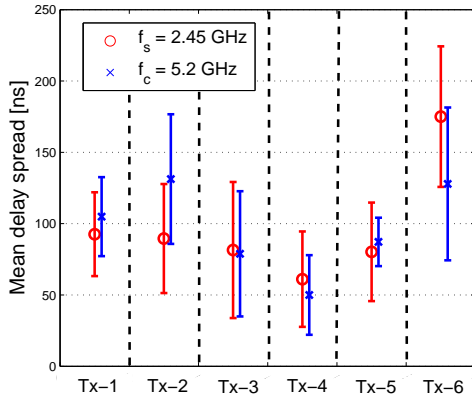

Fig. 7. Mean delay $m(n)$ in dependence of transmit antenna location and frequency band. The error bars are indicating the standard deviation of the calculated values.
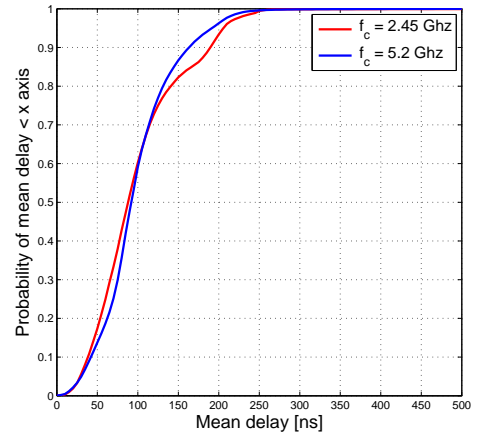
Fig. 9. Cumulative density function of calculated mean delay.

becomes smaller. According to Fig. 8 and Fig. 9 it is noticeable that there are no significant RMS delay spread or mean delay differences between wave propagation at $2.45\,\text{GHz}$ and $5.2\,\text{GHz}$ Also, the CIR examples depicted in Fig. 3 and Fig. 4 show a similar structure. Therefore, the delay spread should be similar. Channel models, which rely on the RMS delay spread for generating wideband CIRs are therefore able to use the same statistics for different frequencies.

C. NLoS Bias

As one of most essential factors in channel modelling for positioning applications, the NLoS bias $\varepsilon(n)$ plays a crucial role in algorithm performance. Fig. 10 to Fig. 12 show statistics of the estimated NLoS bias $\varepsilon(n)$. When the transmit antenna is positioned on the rooftop of building TE02, the NLoS bias does not vary much in its mean value for each antenna position. Only a slight increase for the NLoS bias is visible when the transmit antenna is moving from Tx-1 towards Tx-4. At these positions the waves are propagating directly into the room where the track T1 starts. However,
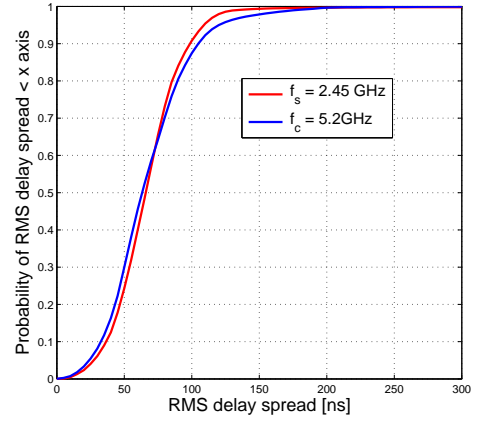
when the transmit antenna is located in the front of TE01, the NLoS bias is obviously larger as visible in Fig. 10. When the transmit antenna is located at Tx-5, there is still a small "visible sight" from the transmit antenna to the outer wall of TE01 facing TE02. The NLoS bias is slightly larger compared to the values obtained, when the transmit antenna is located at Tx-4. It seems that the NLoS bias depends on the incident angle of the waves to the building. When the transmit antenna is located at Tx-6, a direct LoS to the outer wall of TE01 facing TE02 is not present. As a result, the NLoS bias is larger. Similar as for the RMS delay spread, there is no significant difference for the NLoS bias at $2.45\,\text{GHz}$ compared to $5.2\,\text{GHz}$. Therefore, it seems that the NLoS bias is frequency independent.

V. CONCLUSIONS

In this paper, based on a broadband wireless channel measurement campaign, we studied propagation characteristics at $2.45\,\text{GHz}$ and $5.2\,\text{GHz}$ for geolocation applications. It shows that the received power is influenced slightly by the incident angle of the waves to the building. It has been noticed that

Fig. 10. NLoS bias $\varepsilon(n)$ in dependence of transmit antenna location and frequency band. The error bars are indicating the standard deviation of the calculated values.

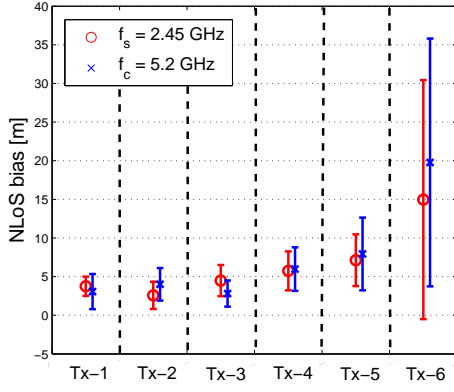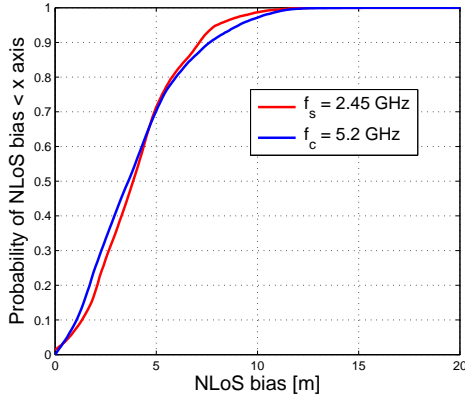Fig. 11. Cumulative density function of estimated NLoS bias when the transmit antenna is located on the rooftop of TE02.
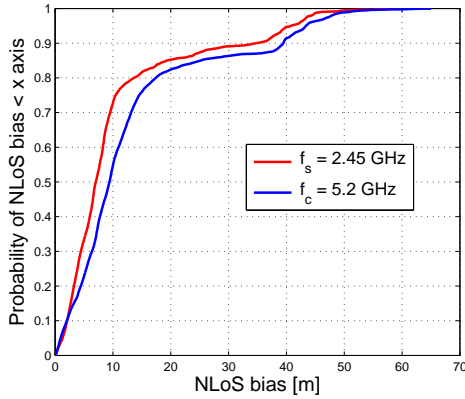
Fig. 12. Cumulative density function of estimated NLoS bias when the transmit antenna is located in front of TE01.

there are no significant differences for RMS delay spread and mean delay at $2.45\,\mathrm{GHz}$ and $5.2\,\mathrm{GHz}$. Therefore, channel models relying on the RMS delay spread to generate wideband CIRs are able to use the same statistics for different carrier frequencies. Moreover, no significant differences for the NLoS bias at $2.45\,\mathrm{GHz}$ compared to $5.2\,\mathrm{GHz}$ could be found.

REFERENCES

[1] C. Mensing, S. Sand, A. Dammann, and W. Utschick. Interference-Aware Location Estimation in Cellular OFDM Communications Systems. *Proceedings of the IEEE International Conference on Communications (ICC)*, Dresden, Germany, June 2009.

[2] C. Mensing, S. Sand, A. Dammann, and W. Utschick. Data-Aided Location Estimation in Cellular OFDM Communications Systems. *Proceedings of the IEEE Global Communications Conference (GLOBECOM)*, Honolulu, HI, USA, November/December 2009.

[3] G. Woodward, I. Oppermann, and J. Talvitie. Outdoor-Indoor Temporal & Spatial Wideband Channel Model for ISM Bands. *Proceedings of the IEEE Vehicular Technology Conference (VTC)*, Amsterdam, Netherlands, September 1999.

[4] W. Wang, T. Jost, and A. Dammann. Outdoor to Indoor Channel Characteristics on Two Different Floors. *European Transactions on Telecommunications*, vol. 21, pp. 426-434, Aug. 2010.

[5] B. Fleury, M. Tschudin, R. Heddergott, D. Dahlhaus, and K. Pedersen. Channel Parameter Estimation in Mobile Radio Environments Using the SAGE Algorithm. *IEEE Journal on Selected Areas in Communications*, vol. 17, no. 3. pp. 434-450, March, 1999.

A.3   Multiple-Links NLoS Error Evaluations for Geolocation Channel Modelling

W. Wang and T. Jost.   Multiple-Links NLoS Error Evaluations for Geolocation Channel Modelling. In *The 71th IEEE Vehicular Technology Conference (VTC 2010 - Spring)*, Taipei, Taiwan, May 2010.

Multiple-Links NLoS Error Evaluations for Geolocation Channel Modelling

Wei Wang and Thomas Jost

German Aerospace Center (DLR)
Institute of Communications and Navigation
Oberpfaffenhofen, 82234 Wessling, Germany
Email: {Wei.Wang, Thomas.Jost}@DLR.de

Abstract—**Time Based (TB) localization by terrestrial cellular communications mobile radio as a complementation to Global Navigation Satellite Systems (GNSSs) has gained plenty of interests. Apart from multipath considered in standard communication channel models, the Non Line-of-Sight (NLoS) error due to an undetectable Line-of-Sight (LoS) path, defined as the additional propagation distance between the first detectable path and the Geometric LoS (GLoS), needs to be taken into account. In TB localizations, the range estimates from at least 3 different links to Base Stations (BSs) are required to solve the 2 dimensional navigation equation. In this paper we analyze the link-level NLoS errors based on a channel measurement campaign. It turns out to be, that the NLoS errors for difference links are i.i.d. processes.**

I. INTRODUCTION

Positioning by using GNSSs, such as the Global Positioning System (GPS) operating at L-band, promises very accurate location information, when a LoS condition to the satellite is present. However, positioning in urban canyons, where LoS might be absent, GNSSs does not provide accurate positions. For some indoor areas, like rooms with metalized windows, satellite signals can not be tracked by GPS receivers because of low signal power. TB localization, utilizing available ground cellular communication networks [1][2], are investigated as a complementation to GNSS with the advantage of higher power level in comparison. By suitable Hybrid Data Fusion (HDF) algorithms to combine measures obtained from GNSS and terrestrial cellular networks, the accuracy of the estimated position can be improved.

As an essential tool for receiver development in terms of TB localization in cellular communication networks, wireless channel modelling has a growing significance. Due to a dissimilar focus between communications and positioning, channel models for both applications are different.

- For communications in cellular networks, multipath modeling is more used to evaluate the Bit Error Rate (BER), and is considered as the most essential part for algorithms evaluation, like the channel estimation, coding/decoding, and synchronization.
- TB positioning using cellular networks focuses on investigating of the position error, which is directly related to the range error of individual links. The ranging accuracy strongly depends on the presence of a GLoS propagation

path. Two different major channel characteristics effect the range error. First a positive bias is introduced if the GLoS path is blocked, such that the ranging is based on the first detectable reflected wave. Generally this bias, between the geometrical distance from the transmitter to the receiver and the propagation distance of the first detectable path is known as the NLoS error [3]. Secondly due to multipath the correlator based synchronizer which is generally used for range estimation is biased positively or negatively by the superposition of pathes [2].

Additionally, in TB localization, ranges from at least 3 different BSs are required to solve the 2 dimensional navigation equation. Therefore, the evaluation of correlation between NLoS errors for different links involved in localization is an important factor to model link level channels. Some research works have investigated the single link NLoS errors based on indoor to indoor ultra wide band measurement [4]. In this paper, we evaluated the link level characteristics of the NLoS errors based on a broadband outdoor to indoor channel sounder measurement at premises of the German Aerospace Center (DLR).

In Section II, the setup of the channel measurement campaign is addressed. Thereafter, Section III discusses the data processing methods and the evaluations. The corresponding results, like the distribution of NLoS error and its link-level correlation are shown in Section IV.

Throughout this paper, $E_x\{\cdot\}$ denotes the expectation over x and is replaced by the sample mean for calculation.

II. CHANNEL MEASUREMENT CAMPAIGN

The measurement was accomplished in the Single Input Single Output (SISO) manner with a MEDAV RUSK broadband channel sounder at premises of the German Aerospace Center (DLR) in June 2008. A spread spectrum signal — in particular an Orthogonal Frequency Division Multiplexing (OFDM) signal — has been sent by the transmitter. The parameter setup of the channel sounder is summarized in Table I. The measured i-th snapshot of the Channel Impulse Response (CIR), $h(i,j), j = 0, \ldots, M-1$ consists of $M = 1537$ samples at delays $\tau_j = j\Delta\tau$, with $\Delta\tau = 1/B$. The channel sounder records one CIR every $T_g = 1.024$ ms providing a measurement rate of 976 CIRs per second (CIRs/s).

TABLE I
CHANNEL SOUNDER SETTINGS FOR THE MEASUREMENT

RF center frequency	5.2 GHz
Bandwidth	$B = 120$ MHz
A/D Converter	8 bits, 320 MHz
Transmit Power	5 W $\cong$ 37 dBm
Signal period	12.8 μs
Number of carrier	1537
Measurement mode	Time grid mode
Measurement time grid	1.024 ms
Antennas	Omni-directional

The receiver antenna was located 1 m above the ground of the top floor of the building. Measurements were performed at $N_P = 90$ points in a distance grid of 1 m covering most of the floor area as shown in Fig. 1. At each point $N = 6000$ CIR snapshots were measured within 6 s. The transmitter was located outside, in front of the building. Fig. 1 depicts the scenario information of the measurement site. Overall 4 different emitter positions were used, 2 different horizontal positions (marked as $H1$ and $H2$), together with 2 different heights ($V1$ and $V2$) for each horizontal position. In this paper we denote the transmitter position by α, where $\alpha \in \{d1\ (H1, V1),\ d2\ (H1, V2),\ d3\ (H2, V1),\ d4\ (H2, V2)\}$. Therefore, 360 point measurements have been obtained. The heights were $H1 = 12$ m and $H2 = 18$ m above the ground. $V1$ and $V2$ were 32 m horizontally spaced. The distance from the transmitter to the outer wall of the building was approximately 16 m.

For range applications the propagation delay is the most important factor and therefore the most important part in this measurement campaign. Hence, receiver and transmitter were perfectly synchronized by cable connection using one common rubidium atomic clock serving as frequency normal. This setup prevents time drifts which usually occur in channel sounder measurements using separated clocks. A system calibration before the measurement has been performed to equalize influences of the analog hardware.

The positions of the transmitter antenna and the receiver antenna were measured in the World Geodetic System 1984 (WGS84) format using a Leica tachymeter system giving a nominal accuracy in sub-cm domain. Thereafter, the true distance from the transmitter to the receiver was determined based on the measured transceiver coordinates to derive the GLoS distance for each point.

III. DATA PROCESSING AND EVALUATION

A. Power Delay Profile (PDP) Normalized to GLoS

To calculate a conventional PDP, the Channel Impulse Response (CIR) is normalized in power by total receive power or maximum path power, and shifted in delay to the first incoming path [5].

In positioning, it is essential to take the GLoS distance into account. To better study the channel PDPs for this purpose, the CIR $h_n(i, j)$ corresponds to $h(i, j)$ normalized in power by the free space loss, and shifted in delay by the GLoS distance divided by speed of light c. The PDP for a measurement at a certain point with a certain transmitter location is calculated
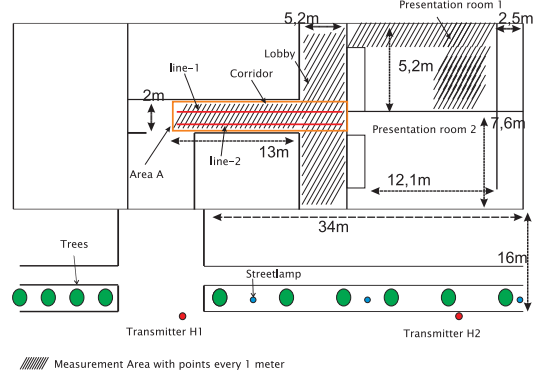
Fig. 1. Scenario information of the measurement

as

$$P_k(j) = \frac{1}{N} \sum_{i=1}^{N} |h_n(i, j)|^2 \qquad (2)$$

where i is the snapshot index for each point, and $k = 1, \ldots, 4N_P$.

B. Channel Parameters Estimation

For each point, the measured CIRs are divided into blocks of 100 snapshots. In each block b, the CIRs are averaged to reduce the noise floor resulting in $h(b, j)$ with increased signal-to-noise ratio. As the environment was stable, the averaging does not introduce disturbance to the CIR. To accurately estimate the path delays, and complex amplitudes from the measured bandlimited CIR, the Space-Alternating Generalized Expectation-maximization (SAGE) super resolution algorithm [6] has been utilized. Without loss of generality, the channel model can be denoted as the summation of paths

$$\hat{h}(b, j) = \sum_{l=1}^{L(b)} a_l(b)s(j - \tau_l(b) \cdot B) \qquad (3)$$

where $a_l(b)$ is the complex amplitude of path l, $\tau_l(b)$ is the delay of path l, and $s(j)$ denotes the transmitted reference signal which is a bandlimited dirac function. $L(b)$ is the number of paths for block b which is estimated by Minimum Description Length (MDL) [7]. Values for the parameters of $\hat{h}(b, j)$ are obtained by fitting to the measured data $h(b, j)$ separately for each block b based on the Maximum Likelihood (ML) criterion for the parameters $a_l(b)$ and $\tau_l(b)$.

C. NLoS Error Calculation

For NLoS scenarios, the GLoS path is blocked by buildings, trees or other objects. As a result, its power P_{GLoS} is extremely low as shown in Fig. 2 and Fig. 3, such that it cannot be detected. The First Detectable Path (FDP) has a larger propagation distance than the GLoS resulting in a bias for ranging applications. The GLoS delay $ToA^{GLoS}(p, \alpha)$ for each point $p = 1, \ldots, N_P$ is determined by the measured distance between transmitter, located at α and receiver point divided by the speed of light. Shown in Fig. 3 as an example,

$$\rho_\varepsilon(\alpha_1, \alpha_2) = \frac{E_p\left\{(\varepsilon_{NLoS}(p, \alpha_1) - E_p\{\varepsilon_{NLoS}(p, \alpha_1)\})(\varepsilon_{NLoS}(p, \alpha_2) - E_p\{\varepsilon_{NLoS}(p, \alpha_2)\})\right\}}{\sqrt{E_p\left\{(\varepsilon_{NLoS}(p, \alpha_1) - E_p\{\varepsilon_{NLoS}(p, \alpha_1)\})^2\right\} E_p\left\{(\varepsilon_{NLoS}(p, \alpha_2) - E_p\{\varepsilon_{NLoS}(p, \alpha_2)\})^2\right\}}} \tag{1}$$
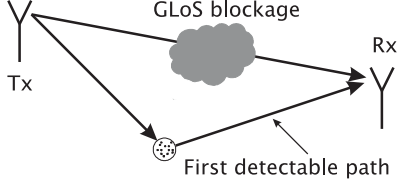

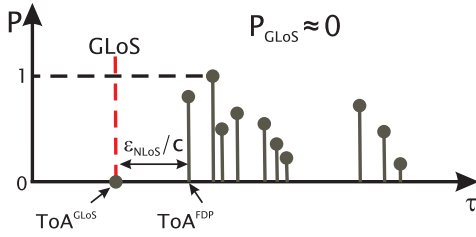Fig. 2. NLoS scenario with blocked GLoS path which is difficult to detect

Fig. 3. Example of a NLoS error ε_{NLoS} for a CIR. c is the speed of light, ToA^{GLoS} is the propagation delay of the GLoS path, and ToA^{FDP} is the propagation delay of first detectable path

the NLoS error $\varepsilon_{NLoS}(p, \alpha)$ for point p is calculated as the mean of NLoS errors of for all blocks

$$\varepsilon_{NLoS}(p, \alpha) = E_b\{c \cdot (ToA^{FDP}(b, p, \alpha)\} - ToA^{GLoS}(p, \alpha)), \tag{4}$$

where $ToA^{FDP}(b, p, \alpha)$ is the estimated delay of the FDP for block b while the transmitter was locating at position α.

The GLoS distance errors caused by the size of the antenna and position measurement errors are in cm domain. However, in order to improve the accuracy, several LoS calibrations were done based on the measurements of LoS points. The GLoS distance was calibrated based on estimated LoS path delay.

D. Inter-Link NLoS Error Correlation Evaluation

As multiple links are required in positioning, the inter-link correlation of NLoS error becomes essential for suitable receiver algorithm development. The inter-link NLoS error correlation coefficient $\rho_\varepsilon(\alpha_1, \alpha_2)$ is defined by Eq. (1). α_1 and α_2 represent the transmitter position $d1$, $d2$, $d3$ or $d4$. Three scenarios are considered in this paper:

- $S1$ where the transmitters are at the same horizontal place with different heights (($d1, d2$), and ($d3, d4$)),
- $S2$ where the transmitter are at same heights with different horizontal places (($d1, d3$), and ($d2, d4$)),
- and $S3$ where the transmitter are at different heights and different horizontal places (($d1, d4$), and ($d2, d3$)).

E. Spatial Characterization

A covariance analysis has been performed to explore the spatial evolution of the NLoS error $\varepsilon_{NLoS}(p, \alpha)$ in a statistical manner. The spatial sample covariance function $c_{\alpha,l}(d)$ is calculated as the covariance of the NLoS error for measurement points by

$$c_{\alpha,l}(d) = E_{p_x, p_y}\{(\varepsilon_{NLoS}(p_x, \alpha) - \mu_{pl})(\varepsilon_{NLoS}(p_y, \alpha) - \mu_{pl})\}. \tag{5}$$

where the expectation is over all sets $\{p_x, p_y\}$ of the two measurement points p_x and p_y on the line-l ($l = 1, 2$, see Fig. 1) separated spatially by d, and the mean μ_{pl} is equal the average NLoS error for point measurement of line-l. In this paper, the d is forced to be 1 m due to spacing between neighboring points.

IV. EVALUATION RESULTS

A. PDP with Normalization to GLoS

The Probability Density Function (PDF) of the PDP $P_k(j)$ is presented in Fig. 4. A Gaussian kernel estimator [8] has been used to estimate the one-dimensional PDF for $P_k(j)$ for each delay bin j. Around delay 0 μs which represents the propagation time of GLoS, the probability of attenuation is spread from −20 dB to −50 dB. For high attenuations the GLoS path is difficult to be detected. In addition, clusters at around 0.2 μs and 0.5 μs are observed. These clusters are well satisfying the mutipath model in [9].

B. NLoS Error Modelling

Mathematical evaluation and modelling of NLoS error are essential for future channel models used for positioning applications. The measured single link NLoS error $\varepsilon_{NLoS}(p, \alpha)$ overall measurements has a mean value of 1.9 meter and a standard deviation of 1.8 meter. To find its PDF, several distributions, like the Weibul distribution, exponential distribution, log normal distribution, and Gaussian distribution, have been tested for fitting. The exponential distribution is found to
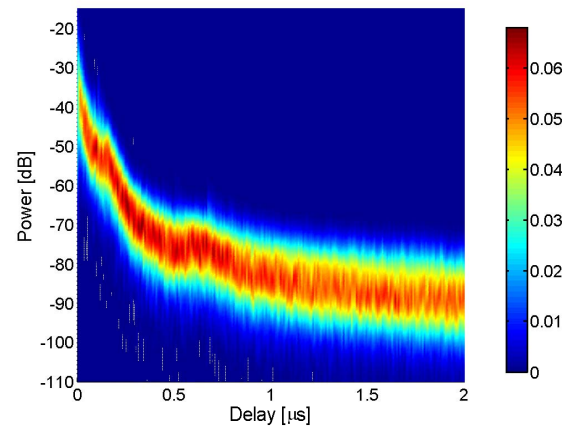

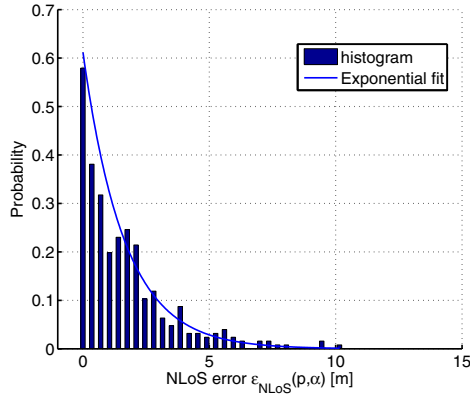Fig. 4. PDF estimate of the PDP $P(j)$ after normalized to GLoS

Fig. 5. Histogram of NLoS error $\varepsilon_{NLoS}(p,\alpha)$ with an exponential fit
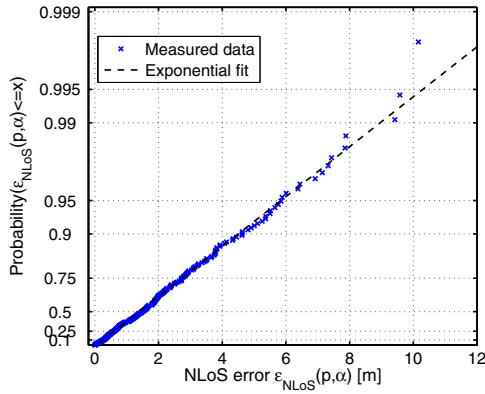

Fig. 6. Probability plot for NLoS error $\varepsilon_{NLoS}(p,\alpha)$ with exponential fit

promise the best fit to the calculated NLoS errors. Fig. 5 shows the histogram of the NLoS error together with its exponential distribution fit. In a more accurate and intuitive way, Fig. 6 shows the probability plot of exponential fit to the NLoS error. To further confirm the exponential fit, the data samples are evaluated by Kolmogorov-Smirnov hypothesis test. The calculated p-value of 0.92 promises a good fit to the null hypothesis of an exponential distribution.

Except for the free space loss, reflection, penetration or diffraction physically degrade the signal strength depending on the materials' electrical properties. For large NLoS errors, the first detectable path suffers from larger attenuations due to the longer propagation distance, reflections and/or diffractions. It is clearly shown in Fig. 7 which depicts the FDP versus the corresponding NLoS error $\epsilon_{NLoS}(p,\alpha)$. Similar as Section III the power is normalized to the free space loss of the GLoS. As soon as the NLoS error becomes larger, the corresponding path suffers from additional attenuation.

C. NLoS Error Correlations

As an essential factor for link level channel models, the inter-link correlation coefficient between $\varepsilon_{NLoS}(p,\alpha)$ for different links is essential. As described in Section III, three scenarios are considered in this paper: $S1$ where the transmitters are at the same horizontal place but different heights ($(d1, d2)$,
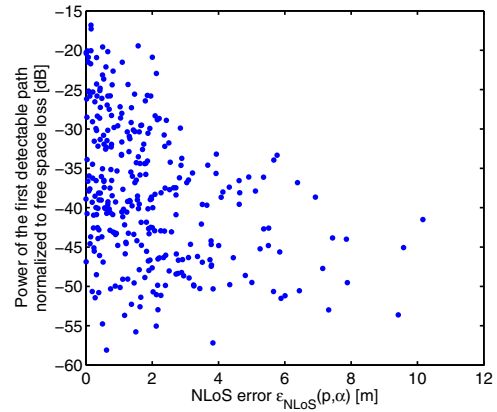
Fig. 7. The first detectable path power normalized to free space loss versus the NLoS error $\varepsilon_{NLoS}(p,\alpha)$

and $(d3, d4)$), $S2$ where the transmitter are at the same height but different horizontal places ($(d1, d3)$, and $(d2, d4)$), and $S3$ where the transmitter are at difference heights and different horizontal places ($(d1, d4)$, and $(d2, d3)$). According to Eq. (1) the correlation coefficients $\rho_\varepsilon(\alpha_1, \alpha_2)$ are listed in Table II. It can be seen that the NLoS errors for different links have a certain correlation if the transmitters were located in the same horizontal place, but different height. For transmitters located at different horizontal places, the NLoS errors of different links have no correlation. In other words, the NLoS errors are uncorrelated to each other. In cellular networks, the links to BSs from different cells would therefore result in uncorrelated NLoS errors. For channel modelling, this implies the fact that NLoS errors for different links can be generated as an independent and identically-distributed process.

TABLE II
INTER-LINK CORRELATION COEFFICIENTS OF $\varepsilon_{NLoS}(p,\alpha)$

$S1$	$\rho_\varepsilon(d1, d2)$	$\rho_\varepsilon(d3, d4)$
	0.4769	0.6874
$S2$	$\rho_\varepsilon(d1, d3)$	$\rho_\varepsilon(d2, d4)$
	-0.192	0.108
$S3$	$\rho_\varepsilon(d1, d4)$	$\rho_\varepsilon(d2, d3)$
	-0.112	-0.072

To evaluate the coherence characteristics of the NLoS error, the spatial correlation of $\epsilon_{NLoS}(p,\alpha)$ is investigated which is calculated as the covariance function. Since the measurement was performed in a discrete point manner, the measurement positions along two lines in the area A (see Fig. 1) are taken into account. Fig. 8 and Fig. 9 show the spatial correlation results for different transmitter positions. Considering a level of 0.5, distances are ranging between 0.5 m and 3 m.

V. CONCLUSIONS

In this paper, based on a broadband wireless channel measurement campaign, we studied propagation characteristic for geolocation channel modelling in terms of the NLoS error. An exponential decaying PDP is observed in the measurement data. Based on probability density function tests, an
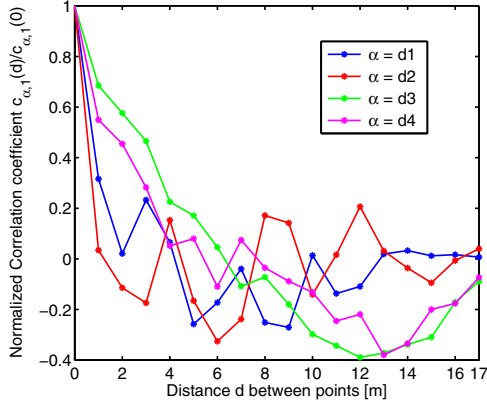
Fig. 8. Spatial correlation of NLoS error $\varepsilon_{NLoS}(p, \alpha)$ for line-1 along the area A
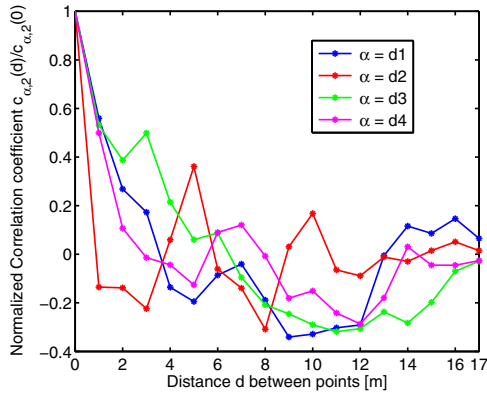
Fig. 9. Spatial correlation of NLoS error $\varepsilon_{NLoS}(p, \alpha)$ for line-2 along the area A

exponential distribution model for NLoS errors is presented in this paper. Additionally, the inter-link correlation of NLoS errors are investigated. The results imply that NLoS errors for different links are independent and identically-distributed processes. However, the NLoS errors from those BSs, which are located at same horizontal places but different heights, show a certain correlation to each other.

REFERENCES

[1] C. Mensing, S. Sand, A. Dammann, and W. Utschick. Interference-Aware Location Estimation in Cellular OFDM Communications Systems. *Proceedings of the IEEE International Conference on Communications (ICC)*, Dresden, Germany, June 2009.

[2] C. Mensing, S. Sand, A. Dammann, and W. Utschick. Data-Aided Location Estimation in Cellular OFDM Communications Systems. *Proceedings of the IEEE Global Communications Conference (GLOBECOM)*, Honolulu, HI, USA, November/December 2009.

[3] W. Wang, T. Jost, C. Mensing, and A. Dammann. ToA and TDoA Error Models for NLoS Propagation Based on Outdoor to Indoor Channel Measurement. *Proceedings of the IEEE Wireless Communications and Networking Conference (WCNC)*, Budapest, Hungary, April 2009.

[4] F. Akgul, and K. Pahlavan. A New Ray Optical Statistical Model for Multipath Characteristics Pertinent to Indoor Geolication. *Proceedings of the IEEE Wireless Communications and Networking Conference (WCNC)*, Budapest, Hungary, April 2009.

[5] T. S. Rappaport. *Wireless Communications, Principles And Practice*. Pearson Education Inc., 2nd Edtion. 2002.

[6] B. Fleury, M. Tschudin, R. Heddergott, D. Dahlhaus, and K. Pedersen. Channel Parameter Estimation in Mobile Radio Environments Using the SAGE Algorithm. *IEEE Journal on Selected Areas in Communications*, vol. 17, no. 3. pp. 434-450, March, 1999.

[7] G. Xu, R. H. Roy, and T. Kailath. Detection of Number of Sources via Exploitation of Centro-Symmetry Property. *IEEE Transactions on Signal Processing*, vol. 42, no. 1. pp. 102-112, January, 1994.

[8] B. W. Silverman. *Density Estimation for Statistic and Data Analysis*. Chapman and Hall. 1986.

[9] A. A. M. Saleh, and R. A. Valenzuela. A Statistical Model for Indoor Multipath Propagation. *IEEE Journal on Selected Areas in Communications*, Vol. SAC-5, No. 2. February 1987.

A.4   Model for the Path Loss of In-room Reverberant Channels

G. Steinböck, T. Pedersen, and B.H. Fleury. Model for the Path Loss of In-room Reverberant Channels. In *Vehicular Technology Conference (VTC 2011-Spring), 2011 IEEE 73rd*, pages 1–5, May 2011.

Model for the Path Loss of In-room Reverberant Channels

Gerhard Steinböck[1], Troels Pedersen[1], Bernard H. Fleury[1], Wei Wang[2], Thomas Jost[2] and Ronald Raulefs[2]

[1]Dept. of Electronic Systems,
Section Navigation and Communications,
Aalborg University
Fredrik Bajers Vej 7, DK-9220 Aalborg East, Denmark
Email: {gs, troels, bfl}@es.aau.dk

[2]Institute of Communications and Navigation,
German Aerospace Center (DLR)
Oberpfaffenhofen, 82234 Wessling, Germany
Email: {Wei.Wang, Thomas.Jost, Ronald.Raulefs}@DLR.de

Abstract—A general path loss model for in-room radio channels is proposed. The model is based on experimental observations of the behavior of the delay-power spectrum in closed rooms. In such a room, the early part of the spectrum observed at different positions typically consists of a dominant component (peak) that vanishes as the transmitter-receiver distance increases; the late part decays versus distance according to the same exponential law in delay regardless of the distance. These observations motivate the proposed model of the delay-power spectrum with an early dominant component and a reverberant component. The dominant component is modeled as a Dirac delta function weighted with a factor decaying according to an inverse distance power law (d^{-n}). The reverberant component is an exponentially decaying function versus delay with distance-dependent onset. Its power decays exponentially with distance. The proposed model allows for the prediction of path loss, mean delay, and rms delay spread versus distance. We use measurements to validate the model. We observe good agreement of the model prediction for mean delay and rms delay spread.

I. INTRODUCTION

The field of indoor radio-localization has recently attracted significant interest. One approach for solving the localization problem is to rely on the measured power of the received signal [1] and to use a path loss model to infer the corresponding length of a radio link. Knowledge of the received power is often used for localization in already deployed systems (e.g. WiFi) where received signal strength is readily available or with cheap low power devices in sensor networks. Even when deploying localization techniques with higher accuracy, path loss models are used to predict the signal-to-noise ratio and the probability of connectivity [2], which are both important criteria for system analysis.

Indoor path loss models, relating the received power to the transmitter-receiver distance, have been a valuable instrument to the communication engineer [3]. A vast amount of such models have been proposed for various propagation scenarios and environments and have been validated for diverse purposes in wireless communications. The primary concern so far has been to predict the power loss with respect to distance. These models consider indoor scenarios in which path loss is caused by transmission across multiple walls and floors, and multipath fading [4], [5]. Thus, they cover a whole building. Only
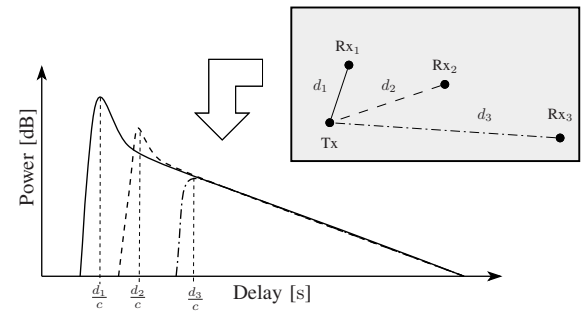
Fig. 1. Typical behavior of the bandlimited delay-power spectrum experimentally observed in an in-room environment at three different transmitter-receiver distances (schematically presented by the grey box).

few models are available in the literature that characterize propagation in a single room [6].

In this contribution we propose an in-room path loss model based on experimental observations of the behavior of the delay-power spectrum [7], [8] and on analogies to models used in room acoustics [9] and electromagnetic fields in cavities [10]. In our model the delay-power spectrum consists of a dominant and a reverberant component. The model allows for the prediction of the path loss, the mean delay and the rms delay spread versus transmitter-receiver distance. The proposed model is validated with a new set of measurement data.

II. DELAY POWER SPECTRUM MODEL

We consider an in-room scenario as illustrated in Fig. 1. The delay-power spectrum is observed at different transmitter and receiver locations. A system bandwidth high enough to observe frequency fading (delay dispersion), but to low to separate single propagation paths in the environment is considered. The regarded carrier frequencies are high enough, such that the smallest dimension of the room is large compared to the wavelength λ. The delay-power spectrum is the expectation of the squared magnitude of the impulse response $h(\tau, d)$:

$$G(\tau, d) = \mathrm{E}[|h(\tau, d)|^2]. \tag{1}$$

Here τ is the delay and d is the transmitter-receiver distance. In [8] it is observed that the delay-power spectrum in such

Parameter	Meaning
G_0	Path gain at reference distance d_0.
d_0	Reference distance, typically 1 m.
n	Path gain decay exponent of the dominant component.
q	Ratio $G_{\text{rev}}(d_0)/G_{\text{dom}}(d_0)$.
T	Reverberation time of the reverberant component.

an in-room scenario exhibits the typical behavior depicted in Fig. 1. The tail of the delay-power spectrum exhibits the same constant exponential decay regardless of the transmitter-receiver distance. The early part is strong at short distance and gradually vanishes as this distance increases.

Based on these observations, we model the delay-power spectrum as a dominant component plus a reverberant component:

$$G(\tau, d) = \mathrm{E}[|h_{\text{dom}}(\tau, d)|^2] + \mathrm{E}[|h_{\text{rev}}(\tau, d)|^2]$$
$$= G_{\text{dom}}(\tau, d) + G_{\text{rev}}(\tau, d). \quad (2)$$

Subscript dom indicates the dominant component and subscript rev denotes the reverberant component. The dominant component represents the early part of the delay-power spectrum consisting of a directly propagating component and possible first-order reflections from the floor, ceiling and walls. The reverberant component represents the multitude of higher order reflections in the room which yield the diffuse tail of the delay-power spectrum.

We model the delay-power spectrum of the dominant component as

$$G_{\text{dom}}(\tau, d) = G_0 \left(\frac{d_0}{d}\right)^n \delta\left(\tau - \frac{d}{c}\right), \quad (3)$$

where n is the power decay exponent, $\delta(\,\cdot\,)$ is the Dirac delta function, c the speed of light, and $G_0 > 0$ is the gain at the reference distance d_0.

We model the reverberant delay-power spectrum as an exponentially decaying function with onset determined by the transmitter-receiver distance:

$$G_{\text{rev}}(\tau, d) = \begin{cases} G_{0,\text{rev}} \, e^{-\frac{\tau}{T}}, & \tau > \frac{d}{c} \\ 0, & \text{otherwise} \end{cases} \quad (4)$$

where $G_{0,\text{rev}}$ is the reference gain of the reverberant component. In analogy to acoustics [8], [9] we call T the reverberation time.

We remark that the models in [7] and [8] are based on the room acoustic theory. They both neglect the transmitter-receiver distance. In [7] the delay-power spectrum of the reverberant component, i.e. corresponding to (4), is non-exponential. It has maximum power one and constant onset at delay zero. In [8] the model only accounts for the exponentially decaying delay-power spectrum of the reverberant component in (2).

III. PREDICTIONS OF THE DELAY POWER SPECTRUM MODEL

Based on the model (2) we now derive expressions for the path gain, mean delay, and rms delay spread as a function of the transmitter-receiver distance.

A. Path gain

The path gain at distance d is

$$G(d) = \int G(\tau, d)\mathrm{d}\tau$$
$$= \underbrace{G_0 \left(\frac{d_0}{d}\right)^n}_{G_{\text{dom}}(d)} + \underbrace{G_{0,\text{rev}} \, T \, e^{\frac{-d}{c\,T}}}_{G_{\text{rev}}(d)}. \quad (5)$$

The component $G_{\text{dom}}(d)$ decays with d^{-n}, while $G_{\text{rev}}(d)$ decays exponentially. Denoting by q the ratio of reverberant to dominant gain at reference distance d_0:

$$q = \frac{G_{\text{rev}}(d_0)}{G_{\text{dom}}(d_0)} = \frac{G_{0,\text{rev}}}{G_0} \, T \, e^{\frac{-d_0}{c\,T}}, \quad (6)$$

the path gain can be recast as

$$G(d) = G_0 \left(\frac{d_0}{d}\right)^n + G_0 \, q \, e^{\frac{d_0 - d}{c\,T}}. \quad (7)$$

Examples of $G(d)$ are graphed in Fig. 2a. At small distances $G_{\text{dom}}(d)$ dominates and the path gain decays as d^{-n}. Beyond a certain distance, the contribution of the reverberant component $G_{\text{rev}}(d)$ in $G(d)$ leads to a deviation from $G_{\text{dom}}(d)$. This effect occurs over a certain distance interval, denoted as the reverberation region $D_{\text{rev}} = \{d : G_{\text{rev}}(d) \geq G_{\text{dom}}(d)\}$. At larger distances $G_{\text{rev}}(d)$ vanishes and $G(d)$ approaches $G_{\text{dom}}(d)$ again.

We remark that the path loss is defined as the inverse of the path gain: $L(d) = G(d)^{-1}$. For notational convenience we consider only path gain in the sequel.

B. Mean Delay and Root Mean Squared Delay Spread

The mean delay at distance d as is derived from (2) as

$$\mu_\tau(d) = \frac{1}{G(d)} \int \tau \, G(\tau, d)\mathrm{d}\tau \quad (8)$$
$$= \frac{d}{c} + T \frac{1}{1 + \left(\frac{d_0}{d}\right)^n \frac{1}{q} \, e^{\frac{d - d_0}{c\,T}}}. \quad (9)$$

In (9) the first term is the delay of a directly propagating component and the second term results from the reverberant component. Fig. 2b depicts the mean delay versus distance with the settings specified in the legend of the figures. The mean delay increases with distance. For distances in the reverberation region, the curves approximately follow the straight line $\frac{d}{c} + T$. It can be seen from (9) that $\lim_{d \to 0} \mu_\tau(d) = 0$ and that $\mu_\tau(d)$ has the asymptote $\frac{d}{c}$ for $d \to \infty$. Note that the range of distance considered in the plot of Fig. 2b is to small to observe the convergence of $\mu_\tau(d)$ towards its asymptote.

Similarly, (2) enables computation of the rms delay spread: $\sigma_\tau(d)$:

$$\sigma_\tau^2(d) = \frac{1}{G(d)} \int \tau^2 \, G(\tau, d)\mathrm{d}\tau - (\mu_\tau(d))^2. \quad (10)$$

Insertion of (7) and (9) into (10) leads to

$$\sigma_\tau^2(d) = \frac{T^2}{1 + \left(\frac{d_0}{d}\right)^n \frac{1}{q} \, e^{\frac{d - d_0}{c\,T}}} \left(2 - \frac{1}{1 + \left(\frac{d_0}{d}\right)^n \frac{1}{q} \, e^{\frac{d - d_0}{c\,T}}}\right). \quad (11)$$
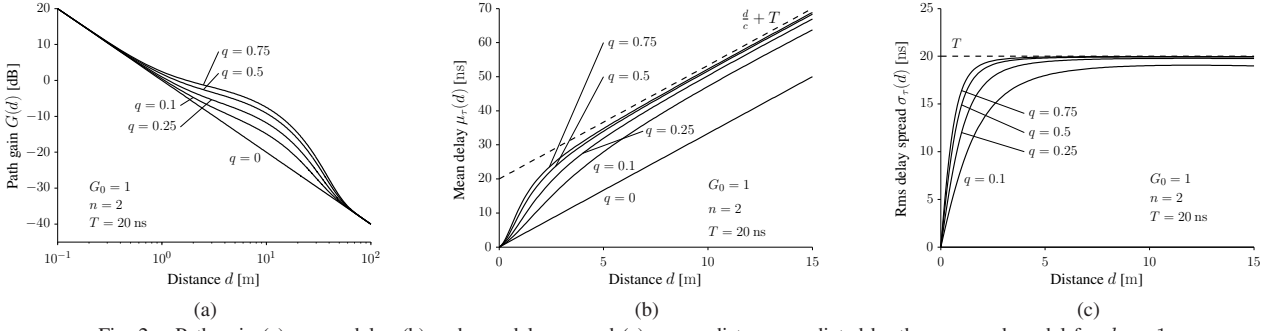
Fig. 2. Path gain (a), mean delay (b) and rms delay spread (c) versus distance predicted by the proposed model for $d_0 = 1$ m.

Fig. 2c depicts the rms delay spread versus distance. Notice, $\sigma_\tau(d)$ in (11) has the following limits

$$\lim_{d \to 0} \sigma_\tau(d) = \lim_{d \to \infty} \sigma_\tau(d) = 0. \qquad (12)$$

Here again, the range of the distance considered in Fig. 2c is to small to observe the convergence of $\sigma_\tau(d)$ towards 0 as $d \to \infty$. For distances in the reverberation region $\sigma_\tau(d)$ approaches the reverberation time T. Indeed it can be shown that

$$T = \sup_{d,n,q} \{\sigma_\tau(d) : d \geq 0, n \geq 0, q \geq 0\}, \qquad (13)$$

i.e. the rms delay spread is upper bounded by T for any distance.

IV. MEASUREMENT DATA

We validate the proposed model by means of measurement data from a campaign conducted at DLR in Oberpfaffenhofen, Germany. The investigated room is sketched in Fig. 3. A panograph of it is depicted in Fig. 4. The environment was static and no one was in the room while the measurements were taken.

The dimensions of the room are $5.1 \times 5.25 \times 2.78$ m^3. The three inner walls are made of plaster boards. As visible in the panograph, the outer "wall" consists mainly of four windows (W1–W4) and two pillars made of concrete. The frames of the windows are metallic and the glass is metal coated. The height of the transmit and receive antenna was 1.26 m and 1.1 m, respectively.

The measurement data were collected using the Rusk-DLR channel sounder [11] operating at 5.2 GHz. The settings of the sounder are summarized in Table II. The transmit antenna [12] was omni-directional with 3 dBi gain. A uniform circular array of eight monopoles with diameter 75.18 mm was used at the receiver. The transmitter and receiver were synchronized to a common clock via cables throughout the measurements.

The equipment used a multiplexer to sequentially sound the eight channels between the port of the transmit antenna and the ports of the eight elements of the receive array. One measurement cycle, in which all eight channel frequency responses were measured, was completed in 204.8 µs. The sounder was operating in "burst" mode. In each burst 20 consecutive measurement cycles were performed. One burst lasted $20 \cdot 204.8$ µs = 4096 µs. Between each burst, the
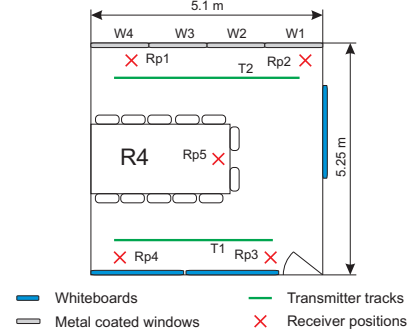
Fig. 3. Schematic of the investigated room.
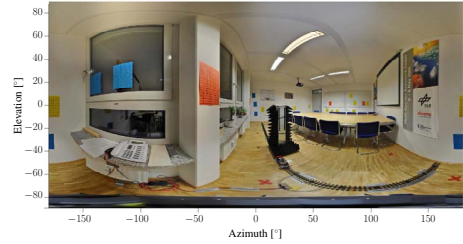
Fig. 4. Panograph (spherical panoramic photo) of the investigated room seen from Rp1 using an equi-rectangular projection.

sounder paused for data storage; the burst repetition time was 131.072 ms.

The receive antenna array was placed at five fixed locations labeled as Rp1 to Rp5 respectively in Fig. 3. The transmit antenna was mounted on a model train which moved on two tracks labeled as T1 and T2. Frequency responses were measured for each receiver position while the transmitter moved along the two tracks with a constant speed of approximately 0.05 m/s. During one measurement burst the transmitter moved 204.8 µm = 0.0035λ. Over this distance the channel response can be considered constant. Between two consecutive bursts, the transmitter moved 6.55 mm $\approx \lambda/8.8$.

The positions Rp1-Rp5 and the trajectory along the track were measured with a tachymeter. The odometer of the model train was connected to the channel sounder to record the measurement locations.

V. RESULTS

We compute the received power at all receiver and transmitter positions. Notice that one measurement burst corresponds uniquely to one pair of transmitter and receiver positions. Let us consider one specific burst. The frequency responses of each of the eight channels measured during the burst are averaged.

The averaged responses are then squared and integrated to obtain the power values of the eight channels. Averaging these values yields the power measured in the burst. Fig. 5 reports the scatter plot of power values computed for all bursts versus transmitter-receiver distance. Since the noise-floor is below -70 dBm in all measurements, we disregard the noise.

We compute the mean delay estimate $\widehat{\mu}_\tau$ and rms delay spread estimates $\widehat{\sigma}_\tau$ for each burst. We multiply the averaged frequency responses of the eight channels obtained for a given burst (see above) with a Hann window. Taking the inverse Fourier transform of the filtered frequency responses yields estimates of the impulse responses of the eight channels. The mean delay and delay spread estimates for the burst are obtained by inserting the squared average of the eight impulse responses in (8) and (10), respectively. These estimates computed for all bursts are reported versus transmitter-receiver distance in Fig. 6. These values are in accordance with values reported in [5] for office environments.

We use the model assumption (4) on the behavior of the tail of the delay-power spectrum versus τ to estimate T from experimental delay-power spectra. More specifically, an estimate of T is obtained from a linear least squares estimate of the slope of the late part of the experimental log power spectra. As can be seen in Fig. 7 the underlying model assumption (4) holds true for the experimental delay-power spectra. Considering the restriction of the log spectra obtained for any transmitter and receiver positions in the delay range 40 ns $\leq \tau \leq 150$ ns, the linear least squares estimator yields $\widehat{T} = 18.73$ ns.

We test the behavior of the mean delay ($\mu_\tau \rightarrow \frac{d}{c} + T$, see Fig. 2b) and the rms delay spread ($\sigma_\tau \approx T$, see Fig. 2c) predicted by the model when d ranges in the reverberation region. The scatter plot of estimates of the rms delay spread in Fig. 6 shows a constant behavior for distances larger than 3 m. Therefore, we estimate T by taking the average of these estimates for $d > 3$ m. This yields $\widehat{T} = 16.02$ ns. Similarly we estimate T from the scatter plot of estimates of the mean delay versus distance. For each estimate, say $\widehat{\mu}_\tau(d)$, the difference $\widehat{\mu}_\tau(d) - \frac{d}{c}$ is computed for $d > 3$ m. The estimate $\widehat{T}$ is the
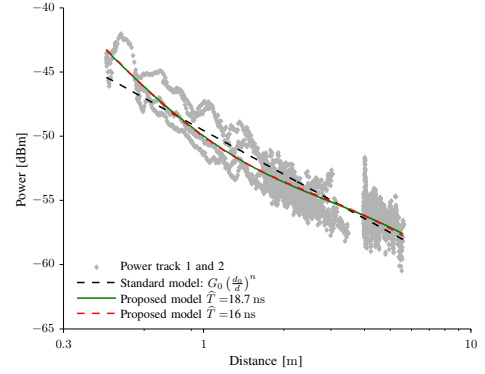
Fig. 5. Estimated received power versus distance with the predictions computed using the standard and the proposed path gain models.
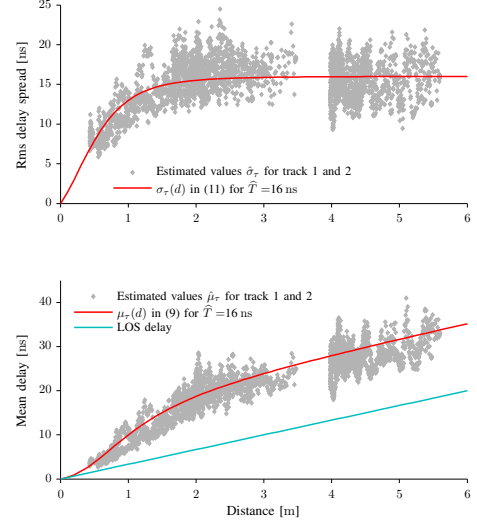
Fig. 6. Scatter plots of estimates of the rms delay spread and the mean delay versus distance. The solid lines depict the predicted rms delay spread and mean delay obtained with the proposed model. For reference we also plot the line corresponding to $\frac{d}{c}$.

average of these differences. Doing so yields $\widehat{T} = 13.07$ ns. The theoretical results for μ_τ and σ_τ in Fig. 2b and Fig. 2c, respectively, show that for some model parameter settings, the bound $\sigma_\tau \approx T$ and specifically the asymptote of the mean delay $\mu_\tau \rightarrow \frac{d}{c} + T$ are not reached. Thus we proceed with the analysis by considering the two close estimates $\widehat{T} = 18.73$ ns and $\widehat{T} = 16.02$ ns.

We estimate the parameters of both the standard path loss model ($G(d) = G_0 \left(\frac{d_0}{d}\right)^n$) and the proposed model from the estimated power values reported in Fig. 5. More specifically, the estimates are computed by considering the log-power domain. For the standard path loss model a linear least squares estimation is performed. We use the Matlab curve fitting toolbox [13], which provides a non-linear least squares estimator, to fit the proposed path gain model (7). This toolbox returns estimates of the parameters G_0, n and q with the estimate $\widehat{T}$ provided as input.

The estimates of the parameters of the models are reported in Table III and the path gains versus distance computed from the models with these parameter settings are shown in Fig. 5. The path gain predictions of the standard and proposed models (for the two sets of parameter estimates) almost overlap.
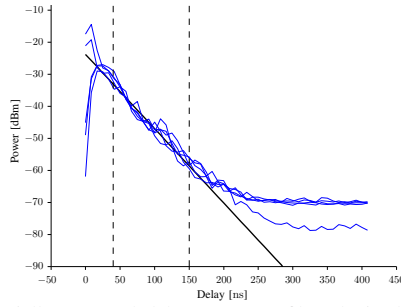
Fig. 7. Spatially averaged delay-power profiles obtained for the receiver positions Rp1 to Rp5 when the transmitter was at the start position on track T1. The straight line depicts an exponentially decaying function with decay factor $\widehat{T} = 18.73\,\text{ns}$. The dashed lines indicate the range $40\,\text{ns} \leq \tau \leq 150\,\text{ns}$ used for the estimation of $\widehat{T}$.

VI. Discussion

The estimate $\widehat{n} = 1.14$ of the path loss exponent of the standard path gain model is in the range of published values obtained from in-room measurement data [6] and references therein. Traditionally, exponent values lower than 2 are attributed to wave guiding effects. However, the dimensions of the room do not advocate this interpretation. A reverberation phenomenon in the room provides a more plausible explanation to the observed low exponent.

The estimates of the mean delay $\widehat{\mu}_\tau(d)$ and rms delay spread $\widehat{\sigma}_\tau(d)$ shown in Fig. 6 are in accordance with the model prediction obtained with $\widehat{T} = 16.02$ ns. The predicted transition of the mean delay and the rms delay spread from zero at $d = 0$ to respectively $\frac{d}{c} + T$ and T for d ranging in the reverberation region is well observed.

The parameter estimates of the model computed from the two estimated reverberation times slightly differ (see Table III). However, the path gains predicted by the two model estimates fall on top of each other as shown in Fig. 7.

The estimate $\widehat{T} = 18.73$ns obtained directly from the delay-power spectra deviates by only 14.5 % from $\widehat{T} = 16.02$ ns obtained from (13). These observations support the hypothesis that the reverberant component impacts significantly the received power, mean delay, and rms delay spread.

The estimated values for q, which characterize the ratio between the power of the dominant and reverberant components, is 0.56 and 0.71 respectively. Thus, the reverberant component plays an important role in the description of the path gain. The estimates $\widehat{n} = 2.26$ and 2.39 of the path gain decay exponent of the dominant component are close to the exponent of free-space propagation.

The estimated reverberation times are close to typical rms delay spreads observed in office environments [5]. This suggests that these rms delay spreads might have been measured in the reverberation region and are thus dominated by the reverberation term. This interpretation is further supported by the fact that the reverberation region starts as close a distance as 1.2 m in the considered scenario.

VII. Conclusions

A model of the delay-power spectrum of an in-room reverberant channel has been proposed. The model includes a dom-inant and a reverberant component. The dominant component follows an inverse distance power law (d^{-n}). The reverberant component decays exponentially versus delay and exhibits a distance dependent onset. As a result, its power decays exponentially with distance. The proposed model allows for the prediction of path gain, mean delay and rms delay spread. The model was validated using measurement data and compared to the standard path loss model. The predictions of mean delay and rms delay spread agree well with the estimates obtained from the measurement data. In the investigated environment the ratio of the gain of the reverberant component to the gain of the dominant component is 0.56. Hence, the reverberant component is prominent in this environment. The estimated path gain exponent of the dominant component in the proposed model is close to the free-space path gain exponent. Due to its inability to separate the dominant component from the reverberant component the standard path gain model yields a path gain exponent close to unity. This model merely provides a fit of the path gain that blends the contributions from the dominant and reverberant component.

References

[1] H. Liu, H. Darabi, P. Banerjee, and J. Liu, "Survey of Wireless Indoor Positioning Techniques and Systems," *IEEE Trans. Syst., Man, Cybern. C*, vol. 37, no. 6, pp. 1067–1080, Nov. 2007.

[2] D. Dardari, A. Conti, C. Buratti, and R. Verdone, "Mathematical Evaluation of Environmental Monitoring Estimation Error through Energy-Efficient Wireless Sensor Networks," *IEEE Trans. Mobile Comput.*, vol. 6, no. 7, pp. 790–802, July 2007.

[3] R. Vaughan and J. B. Andersen, *Channels, Propagation and Antennas for Mobile Communications*. Institution of Engineering and Technology, 2003.

[4] J. Keenan and A. Motley, "Radio coverage in buildings," in *Br. Telecom Technol. J.*, vol. 8, no. 1, Jan. 1990, pp. 19–24.

[5] E. Damosso, Ed., *Digital mobile radio towards future generation systems: COST 231 Final Report*. Bruxelles, Belgium: European Commission, 1999.

[6] D. Xu, J. Zhang, X. Gao, P. Zhang, and Y. Wu, "Indoor Office Propagation Measurements and Path Loss Models at 5.25 GHz," *IEEE Veh. Technol. Conf. (VTC)*, pp. 844–848, Oct. 2007.

[7] C. Holloway, M. Cotton, and P. McKenna, "A model for predicting the power delay profile characteristics inside a room," *IEEE Trans. Veh. Technol.*, vol. 48, no. 4, pp. 1110–1120, 1999.

[8] J. B. Andersen, J. Ø. Nielsen, G. F. Pedersen, G. Bauch, and J. M. Herdin, "Room electromagnetics," *IEEE Antennas Propag. Mag.*, vol. 49, no. 2, pp. 27–33, 2007.

[9] H. Kuttruff, *Room Acoustics*, 4th ed. London: Taylor & Francis, 2000.

[10] D. A. Hill, *Electromagnetic Fields in Cavities: Deterministic and Statistical Theories*, ser. IEEE Press Series on Electromagnetic Wave Theory. Piscataway, NJ: Wiley/IEEE Press, 2009.

[11] J. Stephan, Y. Lostanlen, J. Keignart, W. Wang, D. Slock, and F. Kaltenberger, "Measurements of location-dependent channel features," ICT-217033 WHERE, Del. 4.1, Oct. 2008, http://www.ict-where.eu/.

[12] Huber+Suhner, "Datasheet for Sencity Antenna For In-Carriage Wireless Communication, Type: SOA 5600/360/3/20/V_1," Document No. 01.02.1358, May 2007.

[13] Mathworks, "Matlab Curve Fitting Toolbox, Version 1.2.2 (r2008b)," 2008.

A.5   Modeling of Reverberant Radio Channels Using Propagation Graphs

T. Pedersen, G. Steinböck, and B.H. Fleury. Modeling of Reverberant Radio Channels Using Propagation Graphs. *IEEE Trans. Antennas Propagat.*, submitted.

Modeling of Reverberant Radio Channels Using Propagation Graphs

Troels Pedersen, Gerhard Steinböck, and Bernard H. Fleury

Abstract— It has been observed from measurements that the spatially averaged channel impulse response for in-room scenarios exhibits an avalanche effect: The earliest signal components, which appear well separated in time, are followed by an avalanche of components arriving with increasing rate of occurrence, gradually merging into a diffuse tail with exponentially decaying power. A new approach is followed to design a model of the channel response which includes recursive scattering and thereby inherently accounts for the exponential power decay and the avalanche effect. The environment is modeled in terms of a propagation graph in which vertices represent transmitters, receivers, and scatterers, while edges represent propagation conditions between vertices. A closed form expression of the channel transfer function valid for any number of interactions is derived. We discuss an example where interactions are assumed to cause no time dispersion and thus delay occurs only due to propagation in between scatterers. For this example, a stochastic model of the propagation graph is stated based on which realizations of the channel transfer function and impulse response are generated for numerical evaluation. The results reveal that the graph's recursive structure yields both an exponential power decay and an avalanche effect in the generated impulse responses.

Fig. 1. Spatially averaged delay-power spectrum measured within an office of $5 \times 5 \times 2.6 \, \text{m}^3$ with a signal bandwidth of 10GHz. The spectrum is the rms value of impulse responses obtained at 30×30 receiver positions on a square horizontal grid with steps of 1 cm. The delay scale includes some cable delays; the transmitter-receiver distance is approximately 3.8 m. The vertical axis is with reference to 10 GHz, shifting the curve by $-100 \, \text{dB}$. Reprinted from [6] with permission (©) 2002 IEEE). See [6] for further details.

I. INTRODUCTION

Engineering of modern indoor radio systems for communications and geolocation relies heavily on models for the time dispersion of the wideband and ultrawideband radio channels [3]–[5]. From measurement data, as exemplified in Fig. 1, it appears that the spatially averaged channel impulse response (or delay-power spectrum) for in-room scenarios exhibits an avalanche effect: The earliest signal components, which appear well separated in time, are followed by an avalanche of components arriving with increasing rate of occurrence, gradually merging into a diffuse tail with exponentially decaying power. A similar avalanche effect is well-known in room acoustics [7] where it is attributed to recursive scattering of sound waves. Indoor radio propagation environments are particularly exposed to recursive scattering as electromagnetic waves may be reflected back and forth in between walls, floor, and ceiling. Thus, in the present contribution we hypothesize that recursive scattering is the cause of both the observed avalanche effect and the exponential power decay.

Recursive scattering phenomena have been previously considered in a number of radio channel models. The works [8]–[11] use the analogy to acoustical reverberation theory to predict the exponential decay. As a matter of fact, there exists a well-developed theory of electromagnetic fields in cavities [12], [13], but in this field too the avalanche effect has received little attention. Recursive scattering between particles

Department of Electronic Systems, Aalborg University, DK-9220 Aalborg East, Denmark. Email: {troels,gs,fleury}@es.aau.dk. The present contributions builds on and expands on the work presented in [1], [2].

in a homogeneous medium is a well-known phenomenon studied by Foldy [14] and Lax [15], [16]. The solution, given by the so-called Foldy-Lax equation [17], has been applied in the context of time-reversal imaging by Shi and Nehorai [18]. The solution is, however, intractable for heterogeneous indoor environments. In [19] the radio propagation mechanism is modeled as a "stream of photons" performing continuous random walks in a homogeneously cluttered environment. The model predicts a delay power spectrum consisting of a single directly propagating "coherent component" followed by an incoherent tail. Time-dependent radiosity [20]–[23] accounting for delay dispersion has been recently applied to design a model for the received instantaneous power [24]. Thereby, the exponential power decay and the avalanche effect can be predicted.

Simulation studies of communication and localization systems commonly rely on synthetic realizations of the channel impulse response. A multitude of impulse response models exist [4], [5], [25], but only few account for the avalanche effect. Ray tracing methods can also be used, but to achieve tractable computational complexity, the maximum number of interactions considered is limited [26]. Thus the avalanche effect is discounted. The models [27]–[29] treat early components via a geometric model whereas the diffuse tail is generated via another stochastic process; the connection between the propagation environment and the diffuse tail is, however, not considered.

In this contribution, we model the channel response fol-

lowing a new approach which includes recursive scattering. The obtained model thus accounts inherently for the exponential power decay and the avalanche effect. We represent the environment in terms of a propagation graph, where vertices represent transmitters, receivers, and scatterers, while edges represent propagation conditions between vertices. This modelling approach allows for a closed form expression of the channel transfer function valid for any number of interactions. We assess the validity of the hypothesis by considering an example of a propagation graph suitable for Monte Carlo simulations. Scatterer interactions are assumed to cause no time dispersion and thus delay dispersion occurs only due to propagation in between vertices. We state a stochastic model of the propagation graph allowing for numerical evaluation of realizations of the channel impulse response and transfer function. The results reveal that the graph's recursive structure yields both an exponential power decay and an avalanche effect in the generated impulse responses.

II. REPRESENTING RADIO CHANNELS AS GRAPHS

In a typical propagation scenario, the electromagnetic signal emitted by a transmitter propagates through the environment interacting with a number of objects called scatterers. The receiver, which is usually placed away from the transmitter, senses the electromagnetic signal. If a line of sight exists between the transmitter and the receiver, direct propagation occurs. Also, the signal may arrive at the receiver indirectly via one or more scatterers. In the following we represent recursive and non-recursive propagation mechanisms using graphs. First we state the necessary definitions of directed graphs and associated terms.

A. Directed Graphs

Following [30], we define a directed graph $\mathcal{G}$ as a pair $(\mathcal{V}, \mathcal{E})$ of disjoint sets of vertices and edges. The two mappings $\mathrm{init} : \mathcal{E} \to \mathcal{V}$ and $\mathrm{term} : \mathcal{E} \to \mathcal{V}$ assign to edge $e \in \mathcal{E}$ an initial vertex $\mathrm{init}(e)$ and a terminal vertex $\mathrm{term}(e)$ respectively. We also say that the edge e is ingoing to vertex $\mathrm{term}(e)$ and outgoing from vertex $\mathrm{init}(e)$. Edges e and e' are parallel if $\mathrm{init}(e) = \mathrm{init}(e')$ and $\mathrm{term}(e) = \mathrm{term}(e')$. When a graph has no parallel edges, an edge e can be identified by the vertex pair $(\mathrm{init}(e), \mathrm{term}(e)) \in \mathcal{V}^2$. With a slight abuse of notation we write in this case $e = (\mathrm{init}(e), \mathrm{term}(e))$. With this identification, $\mathcal{E} \subseteq \mathcal{V}^2$. This notation also allows for the graph to have anti-parallel edges, i.e. if the edge $e = (v, v')$ is in the graph, the edge $e' = (v', v)$ can also exist. A walk (of length K) in $\mathcal{G}$ is a sequence $(v_1, v_2, \ldots, v_{K+1})$ of vertices in $\mathcal{V}$ such that $(v_k, v_{k+1}) \in \mathcal{E}, k = 1, \ldots K$. A walk which fulfills $v_1 = v_K$ is called a cycle. A loop is an edge $e = (v, v)$, i.e., $\mathrm{init}(e) = \mathrm{term}(e)$. Thus, by definition, a loop is a walk of length 1.

B. Propagation Graphs

We define a propagation graph as a directed graph $\mathcal{G} = (\mathcal{V}, \mathcal{E})$ where vertices in $\mathcal{V}$ represent transmitters, receivers and scatterers. Edges in $\mathcal{E}$ represent the propagation conditions
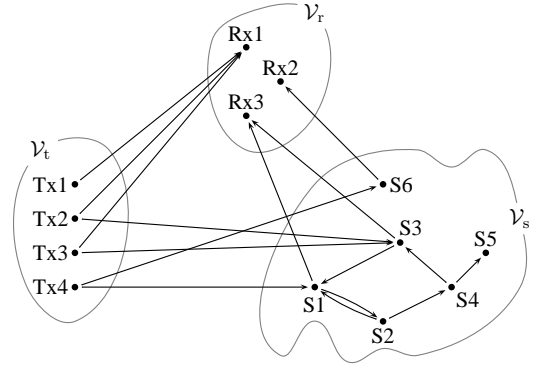
Fig. 2. A propagation graph $\mathcal{G} = (\mathcal{V}, \mathcal{E})$ with four transmit vertices $\mathcal{V}_{\mathrm{t}} = \{\mathrm{Tx1}, \mathrm{Tx2}, \mathrm{Tx3}, \mathrm{Tx4}\}$, three receive vertices $\mathcal{V}_{\mathrm{r}} = \{\mathrm{Rx1}, \mathrm{Rx2}, \mathrm{Rx3}\}$, and six scatterer vertices $\mathcal{V}_{\mathrm{s}} = \{\mathrm{S1}, \mathrm{S2}, \mathrm{S3}, \mathrm{S4}, \mathrm{S5}, \mathrm{S6}, \}$. The edge set $\mathcal{E}$ is the union of the sets $\mathcal{E}_{\mathrm{d}} = \{(\mathrm{Tx1}, \mathrm{Rx1}), (\mathrm{Tx2}, \mathrm{Rx1}), (\mathrm{Tx3}, \mathrm{Rx1})\}$, $\mathcal{E}_{\mathrm{t}} = \{(\mathrm{Tx2}, \mathrm{S3}), (\mathrm{Tx3}, \mathrm{S3}), (\mathrm{Tx4}, \mathrm{S6}), (\mathrm{Tx4}, \mathrm{S1})\}$, $\mathcal{E}_{\mathrm{r}} = \{(\mathrm{S1}, \mathrm{Rx3}), (\mathrm{S3}, \mathrm{Rx3}), (\mathrm{S6}, \mathrm{Rx2})\}$, and $\mathcal{E}_{\mathrm{s}} = \{(\mathrm{S1}, \mathrm{S2}), (\mathrm{S2}, \mathrm{S1}), (\mathrm{S3}, \mathrm{S1}), (\mathrm{S2}, \mathrm{S4}), (\mathrm{S4}, \mathrm{S3}), (\mathrm{S4}, \mathrm{S5})\}$.

between the vertices. Thus, the vertex set of a propagation graph is a union of three disjoint sets: $\mathcal{V} = \mathcal{V}_{\mathrm{t}} \cup \mathcal{V}_{\mathrm{s}} \cup \mathcal{V}_{\mathrm{r}}$, where $\mathcal{V}_{\mathrm{t}} = \{\mathrm{Tx1}, \ldots, \mathrm{Tx}M_{\mathrm{t}}\}$ is the set of transmit vertices, $\mathcal{V}_{\mathrm{r}} = \{\mathrm{Rx1}, \ldots, \mathrm{Rx}M_{\mathrm{r}}\}$ is the set of receive vertices, and $\mathcal{V}_{\mathrm{s}} = \{\mathrm{S1}, \ldots, \mathrm{S}N\}$ is the set of scatterer vertices. The transmit vertices are considered as sources with outgoing edges only. Likewise, the receivers are considered as sinks with only incoming edges. Thus for a propagation graph, the edge set can be partitioned into four disjunct sets as $\mathcal{E} = \mathcal{E}_{\mathrm{d}} \cup \mathcal{E}_{\mathrm{t}} \cup \mathcal{E}_{\mathrm{r}} \cup \mathcal{E}_{\mathrm{s}}$, where $\mathcal{E}_{\mathrm{d}} = \mathcal{E} \cap (\mathcal{V}_{\mathrm{t}} \times \mathcal{V}_{\mathrm{r}})$ is the set of direct edges, $\mathcal{E}_{\mathrm{t}} = \mathcal{E} \cap (\mathcal{V}_{\mathrm{t}} \times \mathcal{V}_{\mathrm{s}})$ is the set of transmitter-scatterer edges, $\mathcal{E}_{\mathrm{r}} = \mathcal{E} \cap (\mathcal{V}_{\mathrm{s}} \times \mathcal{V}_{\mathrm{r}})$ is the set of scatterer-receiver edges, and $\mathcal{E}_{\mathrm{s}} = \mathcal{E} \cap (\mathcal{V}_{\mathrm{s}} \times \mathcal{V}_{\mathrm{s}})$ is the set of inter-scatterer edges. Fig. 2 shows an example propagation graph.

The signals propagate in the graph in the following way. Each transmitter emits a signal that propagates via its outgoing edges. The signal observed by a receiver vertex is the sum of the signals arriving via the ingoing edges. A scatterer sums up the signals on its ingoing edges and re-emits the sum-signal on the outgoing edges. As a signal propagates along an edge, or interacts with a scatterer, it undergoes delay and dispersion in time. The specific delay dispersion endured by a signal depends on the particular propagation mechanism along its edges. Assuming these mechanisms to be linear and time-invariant, this effect can be represented as a convolution with an impulse response or, in the Fourier domain, as a multiplication with a transfer function. Let us for a moment consider the edge $e = (v_n, v_{n'})$ in $\mathcal{E}$. A filtered version of the signal $C_n(f)$ emitted by vertex v_n is observed at vertex $v_{n'}$. The signal observed at vertex $v_{n'}$ via edge e reads $A_e(f)C_n(f)$, where $A_e(f)$ is the transfer function of edge e. In other words, the transfer function $A_e(f)$ describes the interaction the initial vertex v_n and the propagation from v_n to $v_{n'}$.

C. Weighted Adjacency Matrix of a Propagation Graph

Propagation along the edges is described via a transfer matrix $\mathbf{A}(f)$ which can be viewed as an adjacency ma-
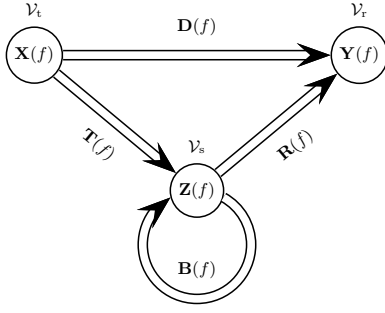
Fig. 3. Vector signal flow graph representation of a propagation graph. Vertices represent vertex sets of the propagation graph with associated vector signals. Signal transmission between the sets are represented by the edges and associated transfer matrices.

trix where the entries are weigthed by the corresponding edge transfer functions. Thus, the weighted adjacency matrix $\mathbf{A}(f) \in \mathbb{C}^{(M_\mathrm{t}+M_\mathrm{r}+N)\times(M_\mathrm{t}+M_\mathrm{r}+N)}$ of the propagation graph $\mathcal{G}$ is defined as

$$[\mathbf{A}(f)]_{nn'} = \begin{cases} A_{(v_n,v_{n'})}(f) & \text{if } (v_n,v_{n'}) \in \mathcal{E}, \\ 0 & \text{otherwise,} \end{cases} \quad (1)$$

i.e., entry n, n' of $\mathbf{A}(f)$ is the transfer function from vertex v_n to vertex $v_{n'}$ of $\mathcal{G}$. Selecting the indexing of the vertices according to

$$v_n \in \begin{cases} \mathcal{V}_\mathrm{t}, & n = 1, \ldots, M_\mathrm{t} \\ \mathcal{V}_\mathrm{r}, & n = M_\mathrm{t}+1, \ldots, M_\mathrm{t}+M_\mathrm{r} \\ \mathcal{V}_\mathrm{s}, & n = M_\mathrm{t}+M_\mathrm{r}+1, \ldots, M_\mathrm{t}+M_\mathrm{r}+N, \end{cases} \quad (2)$$

the weighted adjacency matrix takes the form

$$\mathbf{A}(f) = \begin{bmatrix} \mathbf{0} & \mathbf{0} & \mathbf{0} \\ \mathbf{D}(f) & \mathbf{0} & \mathbf{R}(f) \\ \mathbf{T}(f) & \mathbf{0} & \mathbf{B}(f) \end{bmatrix}, \quad (3)$$

where $\mathbf{0}$ denotes the all-zero matrix of the appropriate dimension and the transfer matrices

$$\mathbf{D}(f) \in \mathbb{C}^{M_\mathrm{r} \times M_\mathrm{t}} \quad \text{connecting } \mathcal{V}_\mathrm{t} \text{ to } \mathcal{V}_\mathrm{r}, \quad (4)$$
$$\mathbf{R}(f) \in \mathbb{C}^{M_\mathrm{r} \times N} \quad \text{connecting } \mathcal{V}_\mathrm{s} \text{ to } \mathcal{V}_\mathrm{r}, \quad (5)$$
$$\mathbf{T}(f) \in \mathbb{C}^{N \times M_\mathrm{t}} \quad \text{connecting } \mathcal{V}_\mathrm{t} \text{ to } \mathcal{V}_\mathrm{s}, \text{ and} \quad (6)$$
$$\mathbf{B}(f) \in \mathbb{C}^{N \times N} \quad \text{interconnecting } \mathcal{V}_\mathrm{s}. \quad (7)$$

The special structure of $\mathbf{A}(f)$ reflects the structure of the propagation graph. The first M_t rows are zero because, we do not accept incoming edges into the transmitters. Likewise columns $M_\mathrm{t}+1, \ldots, M_\mathrm{t}+M_\mathrm{r}$ are all zero since the receiver vertices have no outgoing edges.

The input signal vector $\mathbf{X}(f)$ is defined as

$$\mathbf{X}(f) = [X_1(f), \ldots, X_{M_\mathrm{t}}(f)]^\mathrm{T}, \quad (8)$$

where $X_m(f)$ is the signal emitted by transmitter Txm, and $[\cdot]^\mathrm{T}$ denotes the transposition operator. The output signal vector $\mathbf{Y}(f)$ is defined as

$$\mathbf{Y}(f) = [Y_1(f), \ldots, Y_{M_\mathrm{r}}(f)]^\mathrm{T}, \quad (9)$$

where $Y_m(f)$ is the Fourier transform of the signal observed by receiver Rxm. Similar, to $\mathbf{X}(f)$ and $\mathbf{Y}(f)$ we let $\mathbf{Z}(f)$ denote the output signal vector of the scatterers:

$$\mathbf{Z}(f) = [Z_1(f), \ldots, Z_N(f)]^\mathrm{T}, \quad (10)$$

where the nth entry denotes the Fourier transform of the signal observed at scatterer vertex Sn. By the definition of the propagation graph, there are no other signal sources than the vertices in $\mathcal{V}_\mathrm{t}$. Assuming linear and time-invariant propagation mechanisms, the input-output relation in the Fourier domain reads

$$\mathbf{Y}(f) = \mathbf{H}(f)\mathbf{X}(f), \quad (11)$$

where $\mathbf{H}(f)$ is a $M_\mathrm{r} \times M_\mathrm{t}$ transfer matrix.

The structure of the propagation graph unfolds in the vector signal flow graph depicted in Fig. 3. The vertices of the vector signal flow graph represent the three sets $\mathcal{V}_\mathrm{t}$, $\mathcal{V}_\mathrm{r}$, and $\mathcal{V}_\mathrm{s}$ with the associated signals $\mathbf{X}(f)$,$\mathbf{Y}(f)$, and $\mathbf{Z}(f)$. The edge transfer matrices of the vector signal flow graph are the sub-matrices of $\mathbf{A}(f)$ defined in (4)–(7).

III. TRANSFER MATRIX OF A PROPAGATION GRAPH

In the following we derive the input-output relation of a propagation graph. In Subsection III-A we first discuss how the response of a graph is composed of signal contributions propagating via different propagation paths. This representation is, albeit intuitive, impractical for computation of the transfer function for graphs with cycles. Thus in Subsections III-B and III-C we give the transfer function and partial transfer matrices of a general propagation graph in closed form. Subsection III-D treats the graphical interpretation of reciprocal channels. The section concludes with a discussion of related results in the literature.

A. Propagation Paths and Walks

The concept of a propagation path is a corner stone in modeling multipath propagation. In the literature, this concept is most often defined in terms of the resulting signal components arriving at the receiver. A shortcoming of this definition is that it is often hard to relate to the propagation environment. The graph terminology offers a convenient alternative. We define a propagation path as a walk $\ell = (v^{(0)}, v^{(1)}, \ldots, v^{(K+1)})$ in $\mathcal{G}$ such that the initial vertex $v^{(0)}$ is a transmitter and the terminal vertex $v^{(K+1)}$ is a receiver, i.e., $v^{(0)} \in \mathcal{V}_\mathrm{t}$ and $v^{(K+1)} \in \mathcal{V}_\mathrm{r}$. A signal that propagates along propagation path ℓ traverses $K + 1$ (not necessarily different) edges and undergoes K interactions. We refer to such a propagation path as a K-bounce path. A zero-bounce propagation path $\ell = (v, v')$ is called a line-of-sight path, or direct path, from transmitter v to receiver v'. As an example, referring to the graph depicted in Fig. 2, it is straightforward to verify that $\ell_1 = (\mathrm{Tx1}, \mathrm{Rx1})$ is a direct path, $\ell_2 = (\mathrm{Tx4}, \mathrm{S6}, \mathrm{Rx2})$ is a single-bounce path, and $\ell_3 = (\mathrm{Tx4}, \mathrm{S1}, \mathrm{S2}, \mathrm{S1}, \mathrm{Rx3})$ is a 3-bounce path.

We denote by $\mathcal{L}_{vv'}$ the set of propagation paths in $\mathcal{G}$ from transmitter v to receiver v'. The signal received at v' originating from transmitter v is the superposition of signal

components each propagating via a propagation path in $\mathcal{L}_{vv'}$. Correspondingly, entry (v, v') of $\mathbf{H}(f)$ reads

$$H_{vv'}(f) = \sum_{\ell \in \mathcal{L}_{vv'}} H_\ell(f), \qquad (12)$$

where $H_\ell(f)$ is the transfer function of propagation path ℓ.

The number of terms in (12) equals the cardinality of $\mathcal{L}_{vv'}$, which may, depending on the structure of the graph, be finite or infinite. As an example, the number of propagation paths is infinite if v and v' are connected via a directed cycle in $\mathcal{G}$. The graph in Fig. 2 contains two directed cycles which are connected to both transmitters and receivers.

In the case of an infinite number of propagation paths, computing $H_{vv'}(f)$ directly from (12) is infeasible. This problem is commonly circumvented by truncating the sum in (12) to approximate $H_{vv'}(f)$ as a finite sum. This approach, however, calls for a method for determining how many terms of the sum should be included in order to achieve reasonable approximation.

In the frequently used "K-bounce channel models", propagation paths with more than K interactions are ignored. This approach is motivated by the rationale that at each interaction, the signal is attenuated, and thus terms in (12) resulting from propagation paths with a large number of bounces are weak and can be left out as they do not affect the sum much. This reasoning, however, holds true only if the *sum* of the components with more than K interactions is insignificant, which may or may not be the case. From this consideration, it is clear that the truncation criterion is non-trivial as it essentially necessitates computation of the whole sum before deciding whether a term can be ignored or not.

B. Transfer Matrix for Recursive and Non-Recursive Propagation Graphs

As an alternative to the approximation methods applied to the sum (12) we now give an exact closed-form expression for the transfer function $\mathbf{H}(f)$. Provided that the spectral radius of $\mathbf{B}(f)$ is less than unity, the expression holds true for any number of terms in the sum (12) and thus holds regardless whether the number of propagation paths is finite or infinite.

Theorem 1: If the spectral radius of $\mathbf{B}(f)$ is less than unity, then the transfer matrix of a propagation graph reads

$$\mathbf{H}(f) = \mathbf{D}(f) + \mathbf{R}(f)[\mathbf{I} - \mathbf{B}(f)]^{-1}\mathbf{T}(f). \qquad (13)$$

According to Theorem 1 the transfer matrix $\mathbf{H}(f)$ consists of the two following terms: $\mathbf{D}(f)$ representing direct propagation between the transmitters and receivers and $\mathbf{R}(f)[\mathbf{I} - \mathbf{B}(f)]^{-1}\mathbf{T}(f)$ describing indirect propagation. The condition that the spectral radius of $\mathbf{B}(f)$ be less than unity implies that for any vector norm $\| \cdot \|$, $\|\mathbf{Z}(f)\| > \|\mathbf{B}(f)\mathbf{Z}(f)\|$ for non-zero $\|\mathbf{Z}(f)\|$, cf. [31]. For the Euclidean norm in particular this condition implies the sensible physical requirement that the signal power decreases for each interaction.

Proof: Let $\mathbf{H}_k(f)$ denote the transfer matrix for all k-bounce propagation paths, then $\mathbf{H}(f)$ can be decomposed as

$$\mathbf{H}(f) = \sum_{k=0}^{\infty} \mathbf{H}_k(f), \qquad (14)$$

where

$$\mathbf{H}_k(f) = \begin{cases} \mathbf{D}(f), & k = 0 \\ \mathbf{R}(f)\mathbf{B}^{k-1}(f)\mathbf{T}(f), & k > 0. \end{cases} \qquad (15)$$

Insertion of (15) into (14) yields

$$\mathbf{H}(f) = \mathbf{D}(f) + \mathbf{R}(f)\left(\sum_{k=1}^{\infty} \mathbf{B}^{k-1}(f)\right)\mathbf{T}(f). \qquad (16)$$

The infinite sum in (16) is a Neumann series converging to $[\mathbf{I} - \mathbf{B}(f)]^{-1}$ if the spectral radius of $\mathbf{B}(f)$) is less than unity. Inserting this in (16) completes the proof. ∎

The decomposition introduced in (14) makes the effect of the recursive scattering directly visible. The received signal vector is a sum of infinitely many components resulting from any number of interactions. The structure of the propagation mechanism is further exposed by (16) where the emitted vector signal is re-scattered successively in the propagation environment leading to the observed Neumann series. This allows for modeling of channels with infinite impulse responses by expression (13). It is possible to arrive at (13) in an alternative, but less explicit, manner:

Proof: It is readily observed from the vector signal flow graph in Fig. 3 that $\mathbf{Z}(f)$ can be expressed as

$$\mathbf{Z}(f) = \mathbf{T}(f)\mathbf{X}(f) + \mathbf{B}(f)\mathbf{Z}(f). \qquad (17)$$

Since the spectral radius of $\mathbf{B}(f)$ is less than unity we obtain for $\mathbf{Z}(f)$ the solution

$$\mathbf{Z}(f) = [\mathbf{I} - \mathbf{B}(f)]^{-1}\mathbf{T}(f)\mathbf{X}(f). \qquad (18)$$

Furthermore, according to Fig. 3 the received signal is of the form

$$\mathbf{Y}(f) = \mathbf{D}(f)\mathbf{X}(f) + \mathbf{R}(f)\mathbf{Z}(f). \qquad (19)$$

Insertion of (18) in this expression yields (13). ∎

We remark that the above two proofs allow for propagation paths with any number of bounces. This is highly preferable, as the derived expression (13) is not impaired by approximation errors due to the truncation of the series into a finite number of terms as it occurs when using K-bounce models.

A significant virtue of the expression (13) is that propagation effects related to the transmitters and receivers are accounted for in the matrices $\mathbf{D}(f)$, $\mathbf{T}(f)$ and $\mathbf{R}(f)$, but do not affect $\mathbf{B}(f)$. Consequently, the matrix $[\mathbf{I} - \mathbf{B}(f)]^{-1}$ only needs to be computed once even though the configuration of transmitters and receivers changes. This is especially advantageous for simulation studies of e.g. spatial correlation as this leads to a significant reduction in computational complexity.

C. Partial Transfer Matrices

The closed form expression (13) for the transfer matrix of a propagation graph accounts for propagation via an arbitrary number of scatterer interactions. For some applications it is, however, relevant to study only some part of the response according to a particular number of interactions. One case is where a propagation graph is used to generate only a part of the response and other techniques are used for the remaining

parts. Another case is when one must assess the approximation error when the infinite series is truncated. In the following we derive a few useful expressions for such partial transfer matrices.

We define the $K : L$ partial transfer matrix as

$$\mathbf{H}_{K:L}(f) = \sum_{k=K}^{L} \mathbf{H}_k(f), \quad 0 \le K \le L, \qquad (20)$$

i.e., we include only contributions from propagation paths with at least K, but no more than L bounces. It is straightforward to evaluate (20) for $K = 0$, and $L = 0, 1, 2$:

$$\mathbf{H}_{0:0}(f) = \mathbf{D}(f) \qquad (21)$$
$$\mathbf{H}_{0:1}(f) = \mathbf{D}(f) + \mathbf{R}(f)\mathbf{T}(f) \qquad (22)$$
$$\mathbf{H}_{0:2}(f) = \mathbf{D}(f) + \mathbf{R}(f)\mathbf{T}(f) + \mathbf{R}(f)\mathbf{B}(f)\mathbf{T}(f). \qquad (23)$$

This expansion of the truncated series is quite intuitive but the obtained expressions are increasingly complex for large L. Theorem 2 gives a closed form expression of the partial transfer function $\mathbf{H}_{K,L}(f)$ for arbitrary K and L:

Theorem 2: The partial response $\mathbf{H}_{K:L}(f)$ is given by

$$\mathbf{H}_{K:L}(f) = \begin{cases} \mathbf{D}(f) + \mathbf{R}(f)[\mathbf{I} - \mathbf{B}^L(f)][\mathbf{I} - \mathbf{B}(f)]^{-1}\mathbf{T}(f), \\ \qquad\qquad\qquad\qquad K = 0, L \ge 0 \\ \mathbf{R}(f)[\mathbf{B}^{K-1}(f) - \mathbf{B}^L(f)][\mathbf{I} - \mathbf{B}(f)]^{-1}\mathbf{T}(f), \\ \qquad\qquad\qquad\qquad 0 < K \le L, \end{cases}$$

provided that the spectral radius of $\mathbf{B}(f)$ is less than unity.

Proof: The partial transfer function for $0 \le K \le L$ reads

$$\mathbf{H}_{K:L}(f) = \sum_{k=K}^{\infty} \mathbf{H}_k(f) - \sum_{k'=L+1}^{\infty} \mathbf{H}_{k'}(f)$$
$$= \mathbf{H}_{K:\infty}(f) - \mathbf{H}_{L+1:\infty}(f). \qquad (24)$$

For $K = 0$ we have $\mathbf{H}_{0:\infty}(f) = \mathbf{H}(f)$ by definition; for $K \ge 1$ we have

$$\mathbf{H}_{K:\infty}(f) = \mathbf{R}(f) \sum_{k=K-1}^{\infty} \mathbf{B}^k(f)\mathbf{T}(f)$$
$$= \mathbf{R}(f)\mathbf{B}^{K-1}(f) \sum_{k=0}^{\infty} \mathbf{B}^k(f)\mathbf{T}(f)$$
$$= \mathbf{R}(f)\mathbf{B}^{K-1}(f)[\mathbf{I} - \mathbf{B}(f)]^{-1}\mathbf{T}(f). \qquad (25)$$

Inserting (25) into (24) completes the proof. ∎

Theorem 2 enables closed-form computation of $\mathbf{H}_{K:L}(f)$ for any $K \ge L$. We have already listed a few partial transfer matrices in (21), (22), and (23). By definition the partial response $\mathbf{H}_{K:K}(f)$ equals $\mathbf{H}_K(f)$ for which an expression is provided in (15). The transfer function of the K-bounce approximation is equal to $\mathbf{H}_{0:K}(f)$. Another special case worth mentioning is $\mathbf{H}_{K+1:\infty}(f) = \mathbf{H}(f) - \mathbf{H}_{0:K}(f)$ available from (25), which gives the error due to the K-bounce approximation. Thus the validity of the K-bounce approximation can be assessed by evaluating some appropriate norm of $\mathbf{H}_{K+1:\infty}(f)$.

D. Reciprocity and Propagation Graphs

In most cases, the radio channel is considered reciprocal. As we shall see shortly, the graph terminology accommodates an interesting interpretation of the concept of reciprocity. For any propagation graph we can define the reverse graph in which the roles of transmitter and receiver vertices are swapped. The principle of reciprocity states that the transfer matrix of the reverse channel is equal to the transposed transfer matrix of the forward channel, i.e., a forward channel with transfer matrix $\mathbf{H}(f)$ has a reverse channel with transfer matrix $\tilde{\mathbf{H}}(f) = \mathbf{H}^{\mathrm{T}}(f)$. In the sequel we mark all entities related to the reverse channel with a tilde.

We seek the relation between the forward graph $\mathcal{G} = (\mathcal{V}, \mathcal{E})$ and its reverse $\tilde{\mathcal{G}} = (\tilde{\mathcal{V}}, \tilde{\mathcal{E}})$ under the assumption of reciprocity. More specifically, we are interested in the relation between the weighted adjacency matrix $\mathbf{A}(f)$ of $\mathcal{G}$ and the weighted adjacency matrix $\tilde{\mathbf{A}}(f)$ of $\tilde{\mathcal{G}}$. We shall prove the following theorem:

Theorem 3: A propagation graph $\mathcal{G} = (\mathcal{V}, \mathcal{E})$ with weighted adjacency matrix $\mathbf{A}(f)$ has a reverse graph $\tilde{\mathcal{G}} = (\mathcal{V}, \tilde{\mathcal{E}})$ with edge set $\tilde{\mathcal{E}} = \{(v, v') : (v', v) \in \mathcal{E}\}$ and weighted adjacency matrix $\tilde{\mathbf{A}}(f) = \mathbf{A}^{\mathrm{T}}(f)$.

In words Theorem 3 identifies the graph of the reverse channel as the graph obtained by reversing the direction of all edges of $\mathcal{G}$ while maintaining the edge transfer functions.

Proof: We start by noting that the set of transmitters, receivers, and scatterers is maintained for the reverse channel, thus the vertex set of $\tilde{\mathcal{G}}$ is $\mathcal{V}$. Interchanging the roles of transmitters and receivers means that we admit no edges of the reverse graph $\tilde{\mathcal{G}}$ going into vertices in $\mathcal{V}_{\mathrm{r}}$ and no outgoing edges from vertices in $\mathcal{V}_{\mathrm{t}}$. Consequently, assuming the vertex indexing as in (2), the weighted adjacency matrix of $\tilde{\mathcal{G}}$ is of the form

$$\tilde{\mathbf{A}}(f) = \begin{bmatrix} \mathbf{0} & \tilde{\mathbf{D}}(f) & \tilde{\mathbf{T}}(f) \\ \mathbf{0} & \mathbf{0} & \mathbf{0} \\ \mathbf{0} & \tilde{\mathbf{R}}(f) & \tilde{\mathbf{B}}(f) \end{bmatrix} \qquad (26)$$

where the transfer matrices $\tilde{\mathbf{D}}(f), \tilde{\mathbf{R}}(f), \tilde{\mathbf{T}}(f)$, and $\tilde{\mathbf{B}}(f)$ are defined according to Fig. 4. The input-output relation of the reverse channel reads $\tilde{\mathbf{X}}(f) = \tilde{\mathbf{H}}(f)\tilde{\mathbf{Y}}(f)$ where $\tilde{\mathbf{Y}}(f)$ is the signal emitted by the vertices in $\mathcal{V}_{\mathrm{r}}$ and $\tilde{\mathbf{X}}(f)$ is the signal received by the vertices in $\mathcal{V}_{\mathrm{t}}$. By inspection of Fig. 4 and by arguments similar to those presented in Section III-B we achieve for the reverse channel

$$\tilde{\mathbf{H}}(f) = \tilde{\mathbf{D}}(f) + \tilde{\mathbf{R}}(f) \left[\mathbf{I} - \tilde{\mathbf{B}}(f)\right]^{-1} \tilde{\mathbf{T}}(f). \qquad (27)$$

The reciprocity condition $\tilde{\mathbf{H}}(f) = \mathbf{H}^{\mathrm{T}}(f)$ yields the alternative expression:

$$\tilde{\mathbf{H}}(f) = \mathbf{D}^{\mathrm{T}}(f) + \mathbf{T}^{\mathrm{T}}(f) \left[\mathbf{I} - \mathbf{B}^{\mathrm{T}}(f)\right]^{-1} \mathbf{R}^{\mathrm{T}}(f). \qquad (28)$$

Comparing (27) and (28) it is clear that $\tilde{\mathbf{D}}(f) = \mathbf{D}^{\mathrm{T}}(f), \tilde{\mathbf{B}}(f) = \mathbf{B}^{\mathrm{T}}(f), \tilde{\mathbf{T}}(f) = \mathbf{R}^{\mathrm{T}}(f)$, and $\tilde{\mathbf{R}}(f) = \mathbf{T}^{\mathrm{T}}(f)$. After inserting these four identities into (26) we obtain $\tilde{\mathbf{A}}(f) = \mathbf{A}^{\mathrm{T}}(f)$. The relation between $\tilde{\mathcal{E}}$ and $\mathcal{E}$ now follows from the definition of the weighted adjacency matrix. ∎
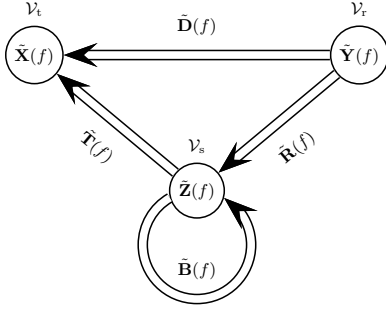
Fig. 4. Vector signal flow graph representation of a reverse propagation graph. Compared to the forward graph depicted in Fig. 3 all edges are reversed.

E. Related Recursive Scattering Models

We provide a few examples of recursive models to assist the reader in recognizing models which can be represented by the graphical structure.

In [18] Shi and Nehorai consider a model for recursive scattering between point scatterers in a homogeneous background. The propagation between any point in space is described by a scalar Green's function. The transfer function obtained by applying the Foldy-Lax equation can also be obtained from a propagation graph by defining the sub-matrices of $\mathbf{A}(f)$ as follows. The model does not include a directed term and thus $\mathbf{D}(f) = \mathbf{0}$. The entry of $[\mathbf{T}(f)]_{m_1 n}$ is the Green's function from transmit vertex m_1 to scatterer n times the scattering coefficient of scatterer n'. Similarly, the entry $[\mathbf{R}(f)]_{nm_2}$ is the Green's function from the position of scatterer n to receiver m_2. The entry $[\mathbf{B}(f)]_{nn'}, n \neq n'$ is the Green's function from the position of scatterer n to the position of scatterer n' times the scattering coefficient of scatterer n. Since a point scatterer does not scatter back on itself, the diagonal entries of $\mathbf{B}(f)$ are all zero. As can be observed from the above definitions, the assumption of homogeneous background medium leads to the special case with $\mathcal{E}_d = \emptyset$, $\mathcal{E}_t = \mathcal{V}_t \times \mathcal{V}_s$, $\mathcal{E}_r = \mathcal{V}_s \times \mathcal{V}_r$, and $\mathcal{E}_t = \mathcal{V}_s^2$.

Another modeling method that can be conveniently described using propagation graphs is (time-dependent) radiosity [24]. The time-dependent radiosity algorithms published in [20]–[24] are formulated in the delay domain. It appears, however, that no closed-form solution feasible for numerical evaluation is available in the literature. Thus [20]–[24] resort to iterative solutions which can be achieved after discretizing the inter-patch propagation delays. The time-dependent radiosity problem can be expressed in the Fourier domain in terms of a propagation graph where each patch is represented by a scatterer, and the entries of $\mathbf{A}(f)$ are defined according to the Fourier transform of the delay-dependent form factor. Using this formulation, a closed form expression of the channel transfer function appears immediately by Theorem 1 with no need for quantization of propagation delays.

F. Revisiting Existing Stochastic Radio Channel Models

It is interesting to revisit existing radio channel models by means of the just defined framework of propagation graphs.

Such an effort may reveal some structural differences between models, which are not apparent merely from the mathematical formulation. It is, however, a fact that the interpretation of a transfer functions as a propagation graph is not unique— different propagation graphs may yield the same transfer function. Therefore different equivalent graphical interpretations may be given for a particular model.

We first consider the structure of the seminal model [32] by Turin *et al.* This model can be expressed in the frequency domain as

$$H(f) = \sum_{\ell=0}^{\infty} \alpha_\ell \exp(-j2\pi f \tau_\ell), \tag{29}$$

where α_ℓ is the complex gain and and τ_ℓ denotes the delay of the ℓth component. We assume that $\tau_0 = 0$. Thus $\{(\tau_\ell, \alpha_\ell) : \ell = 1, 2, \dots\}$ is a marked Poisson point process of delays on $[0, \infty)$ with complex marks $\{\alpha_\ell : \ell = 1, 2, \dots\}$. The reader is referred to [32] for further details. We represent this model as the graph depicted in 5(a). We construct the graph by identifying each term in (29) as corresponding to a specific propagation path from the transmitter to the receiver. It appears that the components $\alpha_\ell \exp(-j2\pi f \tau_\ell), \ell = 0, 1, 2, \dots$ are statistically independent. Therefore, we assign to each component a separate path which results in a graph with infinitely many single-bounce paths. This definition allows for direct interpretation of both the forward and reverse graphs. Since no scatterer-to-scatterer edges exist, $\mathcal{E}_s = \emptyset$ and $\mathbf{B}(f) = \mathbf{0}$. By blocking the propagation from the Tx to scatterer ℓ, the edge (Tx, ℓ) is removed from the graph while the remaining paths are unaffected. The same happens if edge (ℓ, Rx) is removed.

The celebrated model by Saleh and Valenzuela [33] is structured as a second-order Turin model:

$$H(f) = \sum_{\ell=0}^{\infty} \alpha_\ell \exp(-j2\pi f \tau_\ell) \sum_{\ell'=0}^{\infty} \alpha_{\ell\ell'} \exp(-j2\pi f \tau_{\ell\ell'}). \tag{30}$$

Assuming for simplicity that $\tau_0 = 0$ and $\tau_{0\ell'} = 0, \ell' = 0, 1, \dots$, the processes $\{(\alpha_\ell, \tau_\ell) : \ell = 1, 2, \dots\}$ and $\{(\alpha_{\ell\ell'}, \tau_{\ell\ell'}) : \ell = 1, 2, \dots\}, \ell' = 0, 1, \dots$, are independent marked Poisson processes on $[0, \infty)$ with complex marks. Details on these stochastic processes can be found in [33]. Again, considering that statistically independent terms in (30) stem from distinct propagation paths, we can construct the graph depicted in Fig. 5(b). The structure of the graph appears to be asymmetric in the sense that the transmitter is connected to a set of super-ordinate or "cluster" scatterers whereas the receiver is connected to the set of sub-ordinate scatterers. As a result, removing one of the outgoing edges from the transmitter makes a whole cluster disappear; but by removing one of the receiver's ingoing edges only a single component vanishes in the double sum (30). This leads to an interesting effect in the reverse graph: After reversion of all edges the asymmetry is changed as the transmitting vertex is connected to the subordinate scatterers while the receiving vertex is connected to the cluster scatterers. This problem can be circumvented by making the graph symmetric as shown in Fig. 5(c), which in turn necessitates additional scatterers and edges.
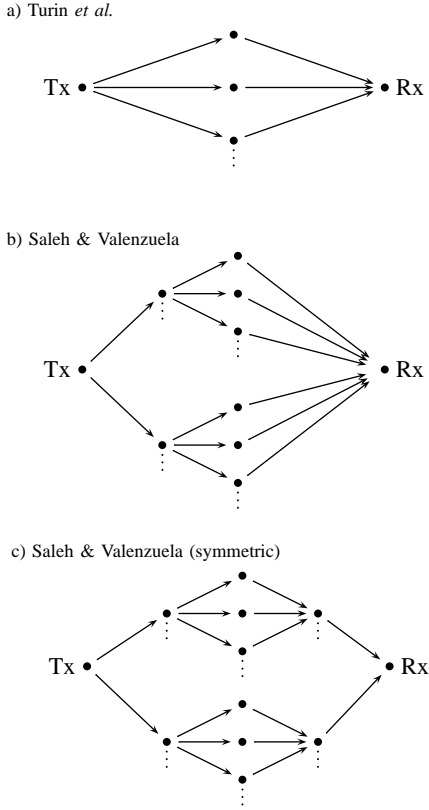
Fig. 5. Propagation graph representations of: a) a realization of the model by Turin *et al.* [32]; b) a realization of the Saleh-Valenzuela model [33]; c) a symmetric version of the model in panel b).

IV. EXAMPLE: STOCHASTIC MODEL FOR IN-ROOM CHANNEL

The concept of propagation graph introduced until now can be used for describing a broad range of channel models. In this section we apply these general results to a specific example scenario where scatterer interactions are considered to be non-dispersive in delay. We specify a method feasible for generating such a graph in Monte Carlo simulations. The model discussed in this example is a variant of the model proposed in [1], [2].

A. Weighted Adjacency Matrix

We define the weighted adjacency matrix according to a geometric model of the environment. We consider a scenario with a single transmitter, a single receiver, and N scatterers, i.e., the vertex set reads $\mathcal{V} = \mathcal{V}_t \cup \mathcal{V}_r \cup \mathcal{V}_s$ with $\mathcal{V}_t = \{Tx\}$, $\mathcal{V}_r = \{Rx\}$, and $\mathcal{V}_s = \{S1, \ldots, SN\}$. To each vertex $v \in \mathcal{V}$ we assign a displacement vector $\mathbf{r}_v \in \mathbb{R}^3$ with respect to a coordinate system with arbitrary origin. To edge $e = (v, v')$ we associate the Euclidean distance $d_e = \|\mathbf{r}_v - \mathbf{r}_{v'}\|$, the gain g_e, the phase ϕ_e, and the propagation delay $\tau_e = d_e/c$ where c is the speed of light. The edge transfer functions are defined as

$$A_e(f) = \begin{cases} g_e(f) \exp(j\phi_e - j2\pi\tau_e f); & e \in \mathcal{E} \\ 0; & e \notin \mathcal{E}. \end{cases} \quad (31)$$

The edge gains $\{g_e(f)\}$ are defined according to

$$g_e^2(f) = \begin{cases} \frac{1}{(4\pi f \tau_e)^2}; & e \in \mathcal{E}_d \\ \frac{1}{4\pi f \mu(\mathcal{E}_t)} \cdot \frac{\tau_e^{-2}}{S(\mathcal{E}_t)}; & e \in \mathcal{E}_t \\ \frac{1}{4\pi f \mu(\mathcal{E}_r)} \cdot \frac{\tau_e^{-2}}{S(\mathcal{E}_r)}; & e \in \mathcal{E}_r \\ \frac{g^2}{\text{odi}(e)^2}; & e \in \mathcal{E}_s \end{cases} \quad (32)$$

where $\text{odi}(e)$ denotes the number of edges from $\text{init}(e)$ to other scatterers and for any $\mathcal{E}' \subseteq \mathcal{E}$

$$\mu(\mathcal{E}') = \frac{1}{|\mathcal{E}'|} \sum_{e \in \mathcal{E}'} \tau_e \quad \text{and} \quad S(\mathcal{E}') = \sum_{e \in \mathcal{E}'} \tau_e^{-2}, \quad (33)$$

with $|\cdot|$ denoting cardinality. The weight of the direct edge is selected according to the Friis equation [34] assuming isotropic antennas at both ends. The weights of edges in $\mathcal{E}_t$ and $\mathcal{E}_r$ also account for the antenna characteristics. They are computed at the average distance to avoid signal amplification when scatterers are close to a transmitter or receiver, namely when the far-field assumption is invalid.

B. Stochastic Generation of Propagation Graphs

We now define a stochastic model of the sets $\{\mathbf{r}_v\}$, $\mathcal{E}$, and $\{\phi_e\}$ as well as a procedure to compute the corresponding transfer function and impulse response. The vertex positions are assumed to reside in a region $\mathcal{R} \subset \mathbb{R}^3$ corresponding to the region of interest. The transmitter and receiver positions are assumed to be fixed, while the positions of the N scatterers $\{\mathbf{r}_v : v \in \mathcal{V}_s\}$ is a Bernoulli point process on $\mathcal{R}$, i.e., the number N of scatterers is assumed constant, and the scatterer positions are drawn independently from a uniform distribution on $\mathcal{R}$.

Edges are drawn independently such that a vertex pair $e \in \mathcal{V}^2$ is in the edge set $\mathcal{E}$ with probability $P_e = \Pr[e \in \mathcal{E}]$ defined as

$$P_e = \begin{cases} P_{\text{dir}}, & e = (Tx, Rx) \\ 0, & \text{term}(e) = Tx \\ 0, & \text{init}(e) = Rx \\ 0, & \text{init}(e) = \text{term}(e) \\ P_{\text{vis}} & \text{otherwise} \end{cases} \quad (34)$$

The first case of (34) controls the occurrence of a direct component. If P_{dir} is zero, the direct term $D(f)$ is zero with probability one. If P_{dir} is unity, the direct term $D(f)$ is non-zero with probability one. The second and third cases of (34) exclude ingoing edges to the transmitter and outgoing edges from the receiver. Thus the generated graphs will have the structure defined in Section II-B. The fourth case of (34) excludes the occurrence of loops in the graphs. This is sensible as a specular scatterer cannot scatter a signal back to itself. A consequence of this choice is that any realization of the graph is loopless and therefore $\mathbf{A}(f)$ has zeros along its main diagonal. The last case of (34) assigns a constant probability P_{vis} of the occurrence of edges from $\mathcal{V}_t$ to $\mathcal{V}_s$, from $\mathcal{V}_s$ to $\mathcal{V}_s$ and from $\mathcal{V}_s$ to $\mathcal{V}_r$.

Finally, the phases $\{\phi_e : e \in \mathcal{E}\}$ are drawn independently from a uniform distribution on the interval $[0; 2\pi)$.

1) Draw $\mathbf{r}_v$, $v \in \mathcal{V}_s$ uniformly on $\mathcal{R}$

2) Generate $\mathcal{E}$ according to (34)

3) Draw independent phases $\{\phi_e : e \in \mathcal{E}\}$ uniformly on $[0, 2\pi)$

4) Compute $\mathbf{A}(f)$ within the frequency bandwidth using (31)

5) IF spectral radius of $\mathbf{B}(f)$ is larger than unity for some frequency within the bandwidth GOTO step 1

6) Estimate $H_{K:L}(f)$ and $h_{K:L}(\tau)$ as described in Appendix

Fig. 6. Algorithm for generating full or partial transfer functions and impulse responses for a preselected bandwidth.

TABLE I

PARAMETER SETTINGS FOR NUMERICAL EXAMPLES

Parameters	Symbol	Values
Room size	$\mathcal{R}$	$[0, 5] \times [0, 5] \times [0, 2.6]\,\mathrm{m}^3$
Transmitter position	$\mathbf{r}_{\mathrm{Tx}}$	$[1.78, 1.0, 1.5]^{\mathrm{T}}\,\mathrm{m}$
Receiver position	$\mathbf{r}_{\mathrm{Rx}}$	$[4.18, 4.0, 1.5]^{\mathrm{T}}\,\mathrm{m}$
Number of scatterers	N	10
Tail slope	ρ	$-0.4\,\mathrm{dB/ns}$
Prob. of visibility	P_{vis}	0.8
Prob. of direct propagation	P_{dir}	1
Speed of light	c	$3 \cdot 10^8$ m/s
Transmit signal	$X[\gamma]$	Unit power Hann pulse
Number of frequency samples	Γ	8192

Given the parameters $\mathcal{R}$, $\mathbf{r}_{\mathrm{Tx}}$, $\mathbf{r}_{\mathrm{Rx}}$, N, P_{dir}, P_{vis} and g, realizations of the (partial) transfer function $H_{K:L}(f)$ and corresponding (partial) impulse response $h_{K:L}(\tau)$ can now be generated for a preselected frequency range $[f_{\min}, f_{\max}]$, using the algorithm stated in Fig. 6.

C. Numerical Experiments

The effect of the recursive scattering phenomenon can now be illustrated by numerical experiments. The parameter settings given in Table I are selected to mimic the experimental setup of [28] used to acquire the measurements reported in Fig. 1. The room size and positions of the transmitter and receiver are chosen as in [28]. We consider the case where direct propagation occurs and set P_{dir} to unity. The probability of visibility P_{vis} and the number of scatterers N are chosen to mimic the observed avalanche effect. The value of g is set to match the tail slope $\rho \approx -0.4\,\mathrm{dB/ns}$ of the delay power spectrum depicted in Fig. 1. The value of g can be related to the slope ρ of the log delay power spectrum via the approximation $\rho \approx 20\log_{10}(g)/\mu(\mathcal{E}_s)$. This approximation arises by considering the power balance for a scatterer assuming the signal components arriving at a scatterer to be statistically independent, neglecting the probability of scatterers with outdegree zero, and approximating edge delays of edges in $\mathcal{E}_s$ by the average $\mu(\mathcal{E}_s)$ defined in (33).

Fig. 7 shows the amplitude of a single realization of the transfer function. Overall, the squared amplitude of the transfer function decays as f^{-2} due to the definition of $\{g_e(f)\}$. Furthermore, the transfer function exhibits fast fading over the considered frequency band. The lower panel of Fig. 7 reports the corresponding impulse response for two different signal bandwidths. Both impulse responses exhibit an avalanche
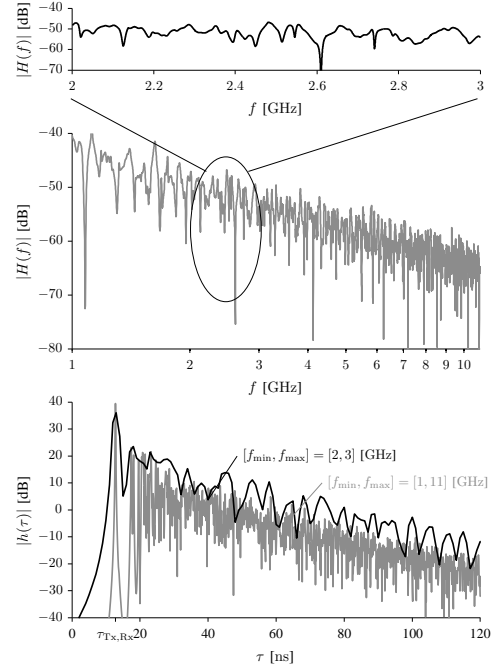
Fig. 7. Channel response for a specific realization of the propagation graph. Top: Transfer function in dB ($20\log_{10}|H(f)|$) in the frequency range $[1, 11]$ GHz. Bottom: Impulse responses in dB ($20\log_{10}|h(\tau)|$) computed for two frequency ranges.

effect as well as a diffuse tail of which the power decays exponentially with $\rho \approx -0.4\,\mathrm{dB/ns}$. As anticipated, the transition to the diffuse tail is most visible in the response obtained with the larger bandwidth.

The build up of the impulse response can be examined via the partial impulse responses given in Fig. 8. Inspection of the partial responses when $K = L$ reveals that the early part of the tail is due to signal components with a low K while the late part is dominated by higher-order signal components. It can also be noticed that as K increases, the delay at which the maximum of the K-bounce partial response occurs and the spread of this response are increasing.

Fig. 9 shows two types of delay-power spectra. The upper panel shows the ensemble average of squared amplitudes of 1000 independently drawn propagation graphs for the two signal bandwidths also considered in Fig. 7. Both spectra exhibit the same trend: A clearly visible peak due to the direct signal is followed by a tail with exponential power decay. As expected, the first peak is wider for the case with $1\,\mathrm{GHz}$ bandwidth than for the case with $10\,\mathrm{GHz}$ bandwidth. The tails differ by approximately 7 dB. This shift arises due to the f^{-2} trend of the transfer function resulting in a higher received power for the lower frequencies considered in the $1\,\mathrm{GHz}$ bandwidth case.

The bottom panel shows spatially averaged delay-power spectra obtained for one particular realization of the propagation graph. The simulated spatial averaged delay-power spectra exhibit the avalanche effect similar to the one observed in Fig. 1. Indeed, for the $10\,\mathrm{GHz}$ bandwidth case the power level
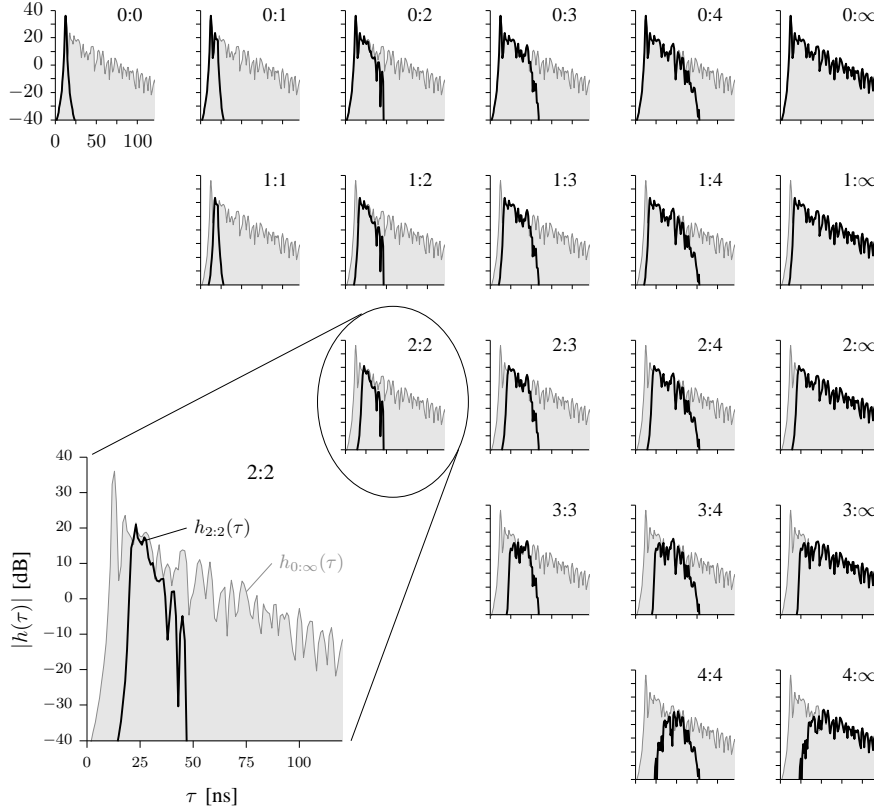
Fig. 8. Partial responses obtained for one graph realization for the bandwidth $[2,3]$ GHz. The $K : L$ settings are indicated in each miniature. The full response is indicated in gray for comparison. Top row: responses of K-bounce approximations. Right-most column: error terms resulting from $(K-1)$-bounce approximations. Main diagonal ($K = L$): K-bounce contributions.
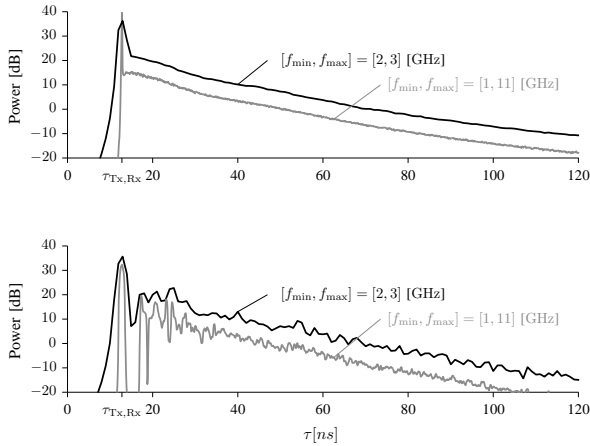
Fig. 9. Simulated delay power spectra. Top panel: Ensemble average over 1000 Monte Carlo runs. Bottom panel: Spatial average of a single graph realization assuming the same grid as the one used in Fig. 1, i.e., 900 receiver positions on a 30×30 horizontal square grid with $1 \times 1 \, \text{cm}^2$ mesh centered at position $\mathbf{r}_{\text{Rx}}$ given in Table I.

of diffuse tails of the delay power spectra agrees remarkably well with measurement in Fig. 1. The modest deviation of about 3 dB can be attributed to antenna losses in the measurement.

V. CONCLUSIONS

The outset for this work was the observation that in-room channels available in the literature are observed to exhibit an avalanche effect where separate signal components appear at increasing rate and gradually merge into a diffuse tail with and exponential decay of power. We hypothesized that this avalanche effect is due to recursive scattering. We propose a model which includes recursive scattering by modeling the propagation environment as a graph where vertices represent transmitters, receivers, and scatterers and edges represent propagation conditions between vertices. This general structure allows for the propagation graph's full and partial transfer matrix to be derived in closed form. This expression can, by specifying the edge transfer functions, be directly used to perform numerical simulations.

We consider as an example a graph-based stochastic model where all interactions are non-dispersive in delay in a scenario similar to an experimentally investigated scenario where the

avalanche effect has been observed. The responses generated from the model also exhibit an avalanche effect. Thus we conclude: 1) the diffuse tail can be generated even when scatterer interactions are non-dispersive in delay and therefore the diffuse tail can be attributed to recursive scattering, and 2) the exponential decay of the delay-power spectra is caused by recursive scattering. As illustrated by the simulation results the proposed model, in contrast to existing models which treats dominant and diffuse components separately, provides a unified account for the avalanche effect.

APPENDIX

The transfer function $\mathbf{H}(f)$ and impulse response $\mathbf{h}(\tau)$ can be estimated as follows:

1) Compute Γ samples of the transfer matrix within the bandwidth $[f_{\min}, f_{\max}]$

$$\mathbf{H}[\gamma] = \mathbf{H}(f_{\min} + \gamma\Delta_f), \quad \gamma = 0, 1, \ldots \Gamma - 1, \quad (35)$$

where $\Delta_f = (f_{\max} - f_{\min})/(\Gamma - 1)$ and $\mathbf{H}(\cdot)$ is obtained using Theorem 1.

2) Estimate the received signal $\mathbf{y}(\tau)$ via the inverse discrete Fourier transform:

$$\mathbf{y}(i\Delta_\tau) = \Delta_f \sum_{\gamma=0}^{\Gamma-1} \mathbf{H}[\gamma]\mathbf{X}[\gamma] \exp(j2\pi i\gamma/\Gamma),$$
$$i = 0, \ldots \Gamma - 1,$$

where $\mathbf{X}[\gamma] = \mathbf{X}(f_{\min} + \gamma\Delta_f), \gamma = 0, 1, \ldots \Gamma - 1$ and $\Delta_\tau = 1/(f_{\max} - f_{\min})$.

The impulse response can be estimated by letting $\mathbf{X}[f]$ be a window function of unit power

$$\int_{f_{\min}}^{f_{\max}} |\mathbf{X}(f)|^2 \mathrm{d}f \approx \sum_{\gamma=0}^{\Gamma} |\mathbf{X}[\gamma]|^2\Delta_f = 1. \quad (36)$$

where $\mathbf{X}[\gamma] = \mathbf{X}(f_{\min} + \gamma\Delta_f)$. The window function must be chosen such that its inverse Fourier transform exhibits a narrow main-lobe and sufficiently low side-lobes; $\mathbf{y}(\tau)$ is then regarded as a good approximation of the impulse response of the channel and by abuse of notation denoted by $\mathbf{h}(\tau)$. Samples of the partial transfer matrix are obtained by replacing $\mathbf{H}(\cdot)$ by $\mathbf{H}_{K:L}(\cdot)$ in (35). The corresponding received partial impulse response is denoted by $\mathbf{h}_{K:L}(\tau)$.

REFERENCES

[1] T. Pedersen and B. Fleury, "Radio channel modelling using stochastic propagation graphs," in *Proc. IEEE International Conf. on Communications ICC '07*, June 2007, pp. 2733–2738.

[2] T. Pedersen and B. H. Fleury, "A realistic radio channel model based on stochastic propagation graphs," in *Proceedings 5th MATHMOD Vienna – 5th Vienna Symposium on Mathematical Modelling*, vol. 1,2, Feb. 2006, p. 324, ISBN 3–901608–30–3.

[3] H. Hashemi, "Simulation of the urban radio propagation," *IEEE Trans. Veh. Technol.*, vol. 28, pp. 213–225, Aug. 1979.

[4] D. Molkdar, "Review on radio propagation into and within buildings," *Microwaves, Antennas and Propagation, IEE Proceedings H*, vol. 138, no. 1, pp. 61–73, 1991.

[5] N. Alsindi, B. Alavi, and K. Pahlavan, "Measurement and modeling of ultrawideband TOA-based ranging in indoor multipath environments," *IEEE Trans. Veh. Technol.*, vol. 58, no. 3, pp. 1046–1058, Mar. 2009.

[6] J. Kunisch and J. Pamp, "Measurement results and modeling aspects for the UWB radio channel," in *IEEE Conf. on Ultra Wideband Systems and Technologies, 2002. Digest of Papers*, May 2002, pp. 19–24.

[7] H. Kuttruff, *Room Acoustics*. London: Taylor & Francis, 2000.

[8] C. Holloway, M. Cotton, and P. McKenna, "A model for predicting the power delay profile characteristics inside a room," *IEEE Trans. Veh. Technol.*, vol. 48, no. 4, pp. 1110–1120, July 1999.

[9] R. Rudd and S. Saunders, "Statistical modelling of the indoor radio channel – an acoustic analogy," in *Proc. Twelfth International Conf. on Antennas and Propagation (Conf. Publ. No. 491)*, vol. 1, 31 March–3 April 2003, pp. 220–224.

[10] R. F. Rudd, "The prediction of indoor radio channel impulse response," in *The Second European Conf. on Antennas and Propagation, 2007. EuCAP 2007.*, Nov. 2007, pp. 1–4.

[11] J. B. Andersen, J. Ø. Nielsen, G. F. Pedersen, G. Bauch, and J. M. Herdin, "Room electromagnetics," *IEEE Antennas Propag. Mag.*, vol. 49, no. 2, pp. 27–33, Apr. 2007.

[12] T. H. Lehman, "A statistical theory of electromagnetic fields in complex cavities," Otto von Guericke University of Magdeburg, Tech. Rep., May 1993.

[13] D. A. Hill, *Electromagnetic Fields in Cavities: Deterministic and Statistical Theories*. Wiley-IEEE Press, 2009.

[14] L. L. Foldy, "The multiple scattering of waves — I general theory of isotropic scattering by randomly distributed scatterers," *Physical Review*, vol. 67, pp. 107–119, Feb. 1945.

[15] M. Lax, "Multiple scattering of waves," *Reviews of Modern Physics*, vol. 23, no. 4, pp. 287–310, Oct. 1951.

[16] ——, "Multiple scattering of waves. II. the effective field in dense systems," *Physical Review*, vol. 85, no. 4, pp. 621–629, Feb. 1952.

[17] M. I. Mishchenko, L. D. Travis, and A. A. Lacis, *Multiple Scattering of Light by Particles: Radiative Transfer and Coherent Backscattering*. Cambridge University Press, May 2006.

[18] G. Shi and A. Nehorai, "Cramér-Rao bound analysis on multiple scattering in multistatic point-scatterer estimation," *IEEE Trans. Signal Process.*, vol. 55, no. 6, pp. 2840–2850, June 2007.

[19] M. Franceschetti, "Stochastic rays pulse propagation," *IEEE Trans. Antennas Propag.*, vol. 52, no. 10, pp. 2742–2752, Oct. 2004.

[20] E.-M. Nosal, M. Hodgson, and I. Ashdown, "Investigation of the validity of radiosity for sound-field prediction in cubic rooms," *The Journal of the Acoustical Society of America*, vol. 116, no. 6, pp. 3505–3514, 2004. [Online]. Available: http://link.aip.org/link/?JAS/116/3505/1

[21] M. Hodgson and E.-M. Nosal, "Experimental evaluation of radiosity for room sound-field prediction," *The Journal of the Acoustical Society of America*, vol. 120, no. 2, pp. 808–819, 2006. [Online]. Available: http://link.aip.org/link/?JAS/120/808/1

[22] S. Siltanen, T. Lokki, S. Kiminki, and L. Savioja, "The room acoustic rendering equation," *The Journal of the Acoustical Society of America*, vol. 122, no. 3, pp. 1624–1635, 2007. [Online]. Available: http://link.aip.org/link/?JAS/122/1624/1

[23] R. T. Muehleisen and C. W. Beamer, IV, "Steady state acoustic radiosity for the prediction of sound pressure levels in enclosures with diffuse surfaces," *Noise Control Engineering Journal*, vol. 57, no. 3, pp. 244–262, 2009. [Online]. Available: http://link.aip.org/link/?NCE/57/244/1

[24] G. Rougeron, F. G. nd Yannik Gabillet, and K. Boutouch, "Simulation of the indoor propgation of a 60 GHz electromagnetic wave with a time-dependent radiosity algorithm," *Computers & Graphics*, vol. 26, pp. 125–141, 2002.

[25] H. Hashemi, "The indoor radio propagation channel," *Proc. IEEE*, vol. 81, no. 7, pp. 943–968, July 1993.

[26] O. Fernandez, L. Valle, M. Domingo, and R. P. Torres, "Flexible rays," *IEEE Veh. Technol. Mag.*, vol. 3, pp. 18–27, Mar. 2008.

[27] J. Kunisch and J. Pamp, "UWB radio channel modeling considerations," in *Proc. International Conference on Electromagnetics in Advanced Applications 2003*, Turin, Sept. 2003.

[28] ——, "An ultra-wideband space-variant multipath indoor radio channel model," in *IEEE Conf. on Ultra Wideband Systems and Technologies, 2003*, Nov. 2003, pp. 290–294.

[29] J. Kunisch, J. amd Pamp, "Locally coherent ultra-wideband radio channel model for sensor networks in industrial environment," in *Proc. IEEE 2006 International Conf. on Ultra-Wideband*, Sept. 2006, pp. 363–368.

[30] R. Diestel, *Graph Theory*. Springer-Verlag, 2000.

[31] R. A. Horn and C. A. Johnson, *Matrix Analysis*. Cambridge University Press, 1985.

[32] G. Turin, F. Clapp, T. Johnston, S. Fine, and D. Lavry, "A statistical model of urban multipath propagation channel," *IEEE Trans. Veh. Technol.*, vol. 21, pp. 1–9, Feb. 1972.

[33] A. A. M. Saleh and R. A. Valenzuela, "A statistical model for indoor multipath propagation channel," *IEEE J. Sel. Areas Commun.*, vol. SAC-5, no. 2, pp. 128–137, Feb. 1987.

[34] H. T. Friis, "A note on a simple transmission formula," *Proceedings of the I.R.E.*, vol. 34, no. 5, pp. 254–256, may 1946.

A.6   Sparse Variational Bayesian SAGE Algorithm with Application to the Estimation of Multipath Wireless Channels

Dmitriy Shutin and Bernard H. Fleury. Sparse variational Bayesian SAGE algorithm with application to the estimation of multipath wireless channels. *to appear in IEEE Transactions on Signal Processing*, 2011.

Sparse Variational Bayesian SAGE Algorithm with Application to the Estimation of Multipath Wireless Channels

Dmitriy Shutin and Bernard H. Fleury

Abstract

In this work we develop a sparse Variational Bayesian (VB) extension of the SAGE algorithm for the high resolution estimation of the parameters of relevant multipath components in the response of frequency and spatially selective wireless channels. The application context of the algorithm considered in this contribution is parameter estimation from channel sounding measurements for radio channel modeling purpose. The new sparse VB-SAGE algorithm extends the classical SAGE algorithm in several respects: by monotonically minimizing the variational free energy, i) distributions of the multipath component parameters can be obtained instead of parameter point estimates and ii) the estimation of the number of relevant multipath components and the estimation of the component parameters are implemented jointly. The sparsity is achieved by defining parametric sparsity priors for the weights of the multipath components. We revisit the Gaussian sparsity priors within the sparse VB-SAGE framework and extend the results by considering Laplace priors. The structure of the VB-SAGE algorithm allows for an analytical stability analysis of the update expression for the sparsity parameters. This analysis leads to fast, computationally simple, yet powerful, adaptive selection criteria applied to the single multipath component considered at each iteration. The selection criteria are adjusted on a per-component-SNR basis to better account for model mismatches, e.g. diffuse scattering, calibration and discretization errors, allowing for a robust extraction of the relevant multipath components. The performance of the sparse VB-SAGE algorithm and its advantages over conventional channel estimation methods are demonstrated in synthetic single-input–multiple-output time-invariant channels. The algorithm is also applied to real measurement data in a multiple-input–multiple-output time-invariant context.

I. INTRODUCTION

In modeling real world data, proper model selection plays a pivotal role. When applying high resolution algorithms to the estimation of wireless multipath channels from multidimensional channel measurements, an accurate determination of the number of dominant multipath components is required in order to reproduce the channel behavior in a realistic manner – an essential driving mechanisms for the design and development of next generation multiple-input–multiple-output (MIMO)-capable wireless communication and localization systems. Consider for simplicity a single-input–multiple-output (SIMO) wireless channel[1], e.g., an uplink channel with a base station equipped with multiple antennas. The received signal vector $\boldsymbol{z}(t)$ made of the signals at the outputs of these antennas can be represented as a superposition of an unknown number L of multipath components $w_l \boldsymbol{s}(t, \boldsymbol{\theta}_l)$ contaminated by additive noise $\boldsymbol{\xi}(t)$ [1]:

$$\boldsymbol{z}(t) = \sum_{l=1}^{L} w_l \boldsymbol{s}(t, \boldsymbol{\theta}_l) + \boldsymbol{\xi}(t). \tag{1}$$

In (1) w_l is the multipath gain factor and $\boldsymbol{s}(t, \boldsymbol{\theta}_l)$ is the received version of the transmitted signal $s(t)$ modified according to the dispersion parameter vector $\boldsymbol{\theta}_l$ of the lth propagation path.[2] Classical parameter estimation [2]–[5] deals with the estimation of the multipath components, i.e. w_l and $\boldsymbol{\theta}_l$, while the estimation of the number L of these components is the object of model order selection [6]–[9]. Despite its obvious simplicity, the model (1) provides an over-simplified description of reality: it adequately accounts for specular-like propagation paths only. Components originating from diffuse scattering inevitably present in measured channel responses are not rendered appropriately in (1). More specifically, a very high number of specular components L is needed to represent such diffuse components. Further effects leading to model mismatch are errors in calibration of the response of the transceiver or measurement equipment that cause inaccuracies in the description of $\boldsymbol{s}(t, \boldsymbol{\theta}_l)$, as well as the discrete-time approximations to (1), typically arising when model parameters are estimated using numerical optimization techniques. All these effects have a significant impact on the performance of both parameter estimation algorithms and model

---

[1]The proposed method can be easily extended to MIMO time-variant channels with stationary propagation constellation; with minor modifications the polarization aspects can be included as well. This extension merely leads to a more complicated signal model, including for instance more dispersion parameters, without adding any new aspect relevant to the understanding of the new proposed concepts and methods. The scenario considering a SIMO channel seems a sensible compromise between complexity of the model underlying the theoretical analyses and an interesting application in which the proposed method can be demonstrated. However, in the experimental section we consider the estimation of a MIMO channel.

[2]We mean as dispersion parameters of the waves propagating from the transmitter side to the receiver site, and by generalization of the multipath components in the resulting channel response, their relative delay, direction of departure, direction of arrival, and Doppler frequency. The parameter $\boldsymbol{\theta}_l$ includes all these parameters or a subset of them depending on the transmitter and receiver configurations.

order selection schemes derived based on (1). Experimental evidence shows that if the model order selection scheme is not carefully designed, the above model mismatch will lead to an overestimation of the number of relevant multipath components. Fictive components without any physical meaning will be introduced and their parameters estimated. Hence, radio channel estimators combining model order (component number) selection and component parameter estimation that are robust against model mismatch are needed here.

Bayesian methods are promising candidates for such robust methods. For a fixed model order L the classical Maximum Likelihood (ML) approach to the estimation of dispersion parameters $\boldsymbol{\Theta} = \{\boldsymbol{\theta}_1, \ldots, \boldsymbol{\theta}_L\}$ and gains $\boldsymbol{w} = \{w_1, \ldots, w_L\}$ in (1) involves maximization of the multidimensional parameter likelihood $p(\boldsymbol{z}|\boldsymbol{\Theta}, \boldsymbol{w})$ given the measurement $\boldsymbol{z}$. Although efficient algorithms exist to solve this optimization problem [2], [3], [10], standard ML algorithms require a fixed number of components L, and typically do not employ any likelihood penalization to compensate for overfitting. Bayesian techniques can compensate for this through the use of a prior $p(\boldsymbol{\Theta}, \boldsymbol{w})$, which effectively imposes constrains on the parameters of the model. The model fit (i.e., the value of the likelihood) can be traded for the model complexity (i.e., number of components in (1)) through the likelihood penalization. Likelihood penalization lies in the heart of celebrated information-theoretic model order selection criteria, such as Minimum Description Length (MDL), Bayesian Information Criterion (BIC), as well as their variants [7]–[9].

Imposing constraints on the model parameters is a key to sparse signal modeling [11]–[16]. In Bayesian sparsity approach [11], [13], [14], [17] the gains $\boldsymbol{w}$ are constrained using a parametric prior $p(\boldsymbol{w}|\boldsymbol{\alpha}) = \prod_l p(w_l|\alpha_l)$, where $p(w_l|\alpha_l)$ is a circularly symmetric probability density function (pdf), with the prior parameter α_l – also called sparsity parameter – being inversely proportional to the width of the pdf. Such form of the prior allows controlling the contribution of each basis associated with the weight w_l through the sparsity parameter α_l: large value of α_l will drive the corresponding weight w_l to zero, thus realizing a sparse estimator. The sparsity parameters are found as the maximizers of $p(\boldsymbol{z}|\boldsymbol{\alpha})$, which is also known as a type-II likelihood function or model evidence [13], [14], [18] and the corresponding estimation approach is known as the Evidence Procedure (EP) [14].

In general, evaluating $p(\boldsymbol{z}|\boldsymbol{\alpha})$ is difficult. This, however, can be done analytically [11], [13], [14], [17] in the special case of linear models[3] $p(\boldsymbol{z}|\boldsymbol{\Theta}, \boldsymbol{w})$ with both model distribution and sparsity prior being Gaussian (which corresponds to the ℓ_2-type of parameter constraints) . Moreover, it can be shown

---

[3]In our context this corresponds to assuming $\boldsymbol{\theta}_l$ as known or fixed, and thus $\boldsymbol{s}(\boldsymbol{\theta}_l) \equiv \tilde{\boldsymbol{s}}$.

[19] that in the Gaussian prior case the maximum of the model evidence $p(\boldsymbol{z}|\boldsymbol{\alpha})$ coincides with the Bayesian interpretation of the Normalized Maximum Likelihood model order selection [7] and reduces to the Bayesian Information Criterion (BIC) as the number of measurement samples grows. Therefore, the EP allows for joint model order selection and parameter estimation. This approach was investigated in [19] within the context of wireless channels; however, work [19] considers the estimation of multipath gains only, thus bypassing the estimation of the dispersion parameters in (1). Recently, a large number of investigations has been dedicated to study of ℓ_1-type of parameter penalties [12], [15], [16], [20], [21], which, in the Bayesian Sparsity framework, is equivalent to choosing $p(w_l|\alpha_l)$ as a Laplace prior for $l = 1, \ldots, L$. Compared to Gaussian priors, such form of constraints leads to sparser models [13], [15], [22], [23]. The ℓ_1-type of penalties significantly limits the analytical study of the algorithm; nonetheless for models linear in their parameters a number of efficient numerical techniques has been developed [15], [24], [25]. Extensions of the Bayesian sparsity methods with Laplace priors applied to the estimation of multipath wireless channels have not been explored yet, mainly due to the nonlinearity of the channel model in $\boldsymbol{\Theta}$. This can be circumvented using virtual channel models [16], [21], which is equivalent to a sampling or gridding of the dispersion parameters $\boldsymbol{\Theta}$ at the Nyquist rate [16]. The algorithm then estimates the coefficients on the grid using sparsity techniques [12], [16], [21]. This approach, however, does not provide high resolution estimates of the multipath parameters. Although it is very effective in capturing channel energy, recent investigations [26] demonstrate that this approach inevitably leads to a mismatch between the true channel sparsity and the estimated sparsity; more specifically, even when fine quantization of $\boldsymbol{\Theta}$ is used, the number of virtual multipath components will always exceed the true number of multipath components; in that respect the channel estimates derived based on virtual models are not appropriate when the goal is to extract physical multipath components. In this paper we aim to demonstrate that the super-resolution property should not be sacrificed to the linearity of the estimation problem. We achieve this by i) casting a super-resolution SAGE algorithm for multipath parameter estimation [3] in a Bayesian framework, and treating the entries in $\boldsymbol{\Theta}$ as random variables whose pdfs are to be estimated and ii) combining this estimation scheme with the Bayesian sparsity techniques, as mentioned in the previous paragraph, i.e., using multiple sparsity parameters α_l to control the model sparsity on a per-component basis. Moreover, as we will show, our analysis also allows defining ways to reduce the impact of estimation artifacts due to the basis mismatches through a detailed analysis of the estimation expressions for the sparsity parameters.

Our main contribution in this work is twofold. First, in order to realize Bayesian sparse estimation and to overcome the computational difficulties due to the nonlinearity of the channel model, we propose a

new Variational Bayesian [27] extension of the Space-Alternating Generalized Expectation-Maximization (SAGE) algorithm for multipath parameter estimation [3], [28] – Variational Bayesian SAGE (VB-SAGE). In contrast to the SAGE algorithm, the VB-SAGE algorithm estimates the posterior pdfs of the model parameters by approximating the true posterior pdf $p(\boldsymbol{\Theta}, \boldsymbol{w}, \boldsymbol{\alpha}|\boldsymbol{z})$ with a proxy pdf $q(\boldsymbol{\Theta}, \boldsymbol{w}, \boldsymbol{\alpha})$ such as to minimize the variational free energy [27]. Similar to the original SAGE algorithm [28], the VB-SAGE algorithm relies on the concept of the admissible hidden data – an analog of the complete data in the EM framework – to optimize at each iteration the variational free energy with respect to the pdfs of the parameters of one component only. We demonstrate that the Monotonicity Property of the VB-SAGE algorithm guarantees that such optimization strategy necessarily minimizes the variational free energy. Such optimization strategy makes the estimation of the parameters in $\boldsymbol{\Theta}$ a tractable optimization problem due to the reduced dimensionality of the resulting objective functions. Second, we demonstrate that the admissible hidden data also permits a detailed analytical study of the sparsity parameters $\boldsymbol{\alpha}$, which leads to selection criteria applied individually to the multipath component updated at each iteration. These selection criteria, on the one hand, allow for a fast implementation of the sparse channel estimator; on the other hand these criteria are easy to interpret and can be adjusted to compensate for model mismatch due to e.g. calibration and discretization errors. Thus, the sparse VB-SAGE algorithm jointly implements the estimation of the number of relevant multipath components and the estimation of the posterior pdfs of the component parameters. We revisit and extend the Gaussian prior case, and present new results for Laplace sparsity priors within the framework of the VB-SAGE algorithm. It should also be mentioned that the performed analysis of sparsity parameters $\boldsymbol{\alpha}$ is equally valid for the problem of sparse estimation of virtual channels models [16] with VB-SAGE algorithm. However, the application of the sparse VB-SAGE algorithm to the estimation of virtual channel models is outside the scope of the paper.

The paper is organized as follows: In Section II we introduce the signal model; Section III addresses the derivation of the VB-SAGE algorithm for the multipath parameter estimation, followed by the analysis of the sparsity priors for model order selection discussed in Section IV; in Section V several practical issues, e.g. algorithm initialization, are discussed; finally, in Section VI estimation results obtained from synthetic and measured data are presented.

Through the paper we shall make use of the following notation. Vectors are represented as boldface lowercase letters, e.g., $\boldsymbol{x}$, and matrices as boldface uppercase letters, e.g., $\boldsymbol{X}$. For vectors and matrices $(\cdot)^T$ and $(\cdot)^H$ denote the transpose and Hermitian transpose, respectively. Sets are represented as calligraphic uppercase letters, e.g., $\mathcal{S}$. We use $\mathcal{I}$ to denote an index set, i.e., $\mathcal{I} = \{1, \ldots, L\}$. The assumed number of elements in $\mathcal{I}$ is L, unless stated otherwise. We will write $\boldsymbol{x}_{\mathcal{I}} \equiv \bigcup\{\boldsymbol{x}_l\}$ as a shorthand notation for a list of

variables $\boldsymbol{x}_l$ with indices $l \in \mathcal{I}$. When $\mathcal{S}$ is a set and $\boldsymbol{x} \in \mathcal{S}$, then $\overline{\mathcal{S}(\boldsymbol{x})} = \mathcal{S} \backslash \{\boldsymbol{x}\}$ is the complement of $\{\boldsymbol{x}\}$ in $\mathcal{S}$. Similarly, $\overline{\mathcal{I}(l)} = \mathcal{I} \backslash \{l\}$ and $\overline{\mathcal{S}(\mathcal{M})} = \mathcal{S} \backslash \mathcal{M}$. Two types of proportionality are used: $x \propto y$ denotes $x = \alpha y$; $x \propto^e y$ denotes $e^x = e^\beta e^y$ and thus $x = \beta + y$, for arbitrary constants α and β. An estimate of a random variable $\boldsymbol{x}$ is denoted as $\widehat{\boldsymbol{x}}$. We use $\mathbb{E}_{q(\boldsymbol{x})}\{f(\boldsymbol{x})\}$ to denote the expectation of a function $f(\boldsymbol{x})$ with respect to a probability density $q(\boldsymbol{x})$; similarly, $\mathbb{E}_{q(\mathcal{M})}\{f(\boldsymbol{x})\}$ denotes the expectation with respect to the joint probability density $q(\mathcal{M})$ of the random variables in the set $\mathcal{M}$. Finally, $N(\boldsymbol{x}; \boldsymbol{a}, \boldsymbol{B})$ and $CN(\boldsymbol{x}; \boldsymbol{a}, \boldsymbol{B})$ denotes respectively a multivariate real and complex Gaussian pdf with a mean $\boldsymbol{a}$ and a covariance matrix $\boldsymbol{B}$; $Ga(x; a, b)$ denotes a Gamma pdf with parameters a and b.

II. SIGNAL MODEL

Channel sounding is an instrumental method for the design of accurate, and realistic radio channel models. Channel sounding is usually performed by sending a specific sounding sequence $u(t)$ through the channel and observing the response $z(t)$ at the receiving side. The received signal $z(t)$ is then used to estimate the channel impulse response (CIR) or its parameters when a parametric model of the response is considered. Consider now a Single-Input Multiple-Output (SIMO) channel model and time-domain channel sounding. The sounding signal $u(t)$ consists of N_u periodically repeated burst waveforms $b(t)$, i.e., $u(t) = \sum_{i=0}^{N_u-1} b(t - iT_f)$, where $b(t)$ has duration $T_b \leq T_f$ and is formed as $b(t) = \sum_{m=0}^{M-1} b_m p(t - mT_p)$. The known sounding sequence $b_0 \ldots b_{M-1}$ consists of M chips and $p(t)$ is the shaping pulse of duration T_p, with $MT_p = T_b$. We assume that the signal vector $\boldsymbol{z}(t)$ has been received/measured with an antenna array consisting of M_r sensors located at positions $\boldsymbol{d}_0, \ldots, \boldsymbol{d}_{M_r-1} \in \mathbb{R}^2$ with respect to an arbitrary reference point. The signal originating from the lth propagation path is an altered version of the original transmitted signal $u(t)$ weighted by a complex gain w_l. The alteration process is described by a (nonlinear) mapping $u(t) \mapsto \boldsymbol{s}(t, \boldsymbol{\theta}_l)$, where $\boldsymbol{\theta}_l$ is the vector of dispersion parameters, e.g., relative delay, azimuth and elevation angles of arrival. The nonlinear mapping $u(t) \mapsto \boldsymbol{s}(t, \boldsymbol{\theta}_l)$ includes the system effects, e.g., the transmitter and the receiver RF/IF filters, the response of the transmit and receive arrays, which in turn depends on the field patterns of their antenna elements and their layout. In the sequel we try to abstract from the concrete channel structure where it is possible and keep the model in its most general form. Additive noise $\boldsymbol{\xi}(t)$ is assumed to be a zero-mean spatially white and temporally wide-sense stationary Gaussian process, i.e., $E\{\xi_k(t)\xi_k^*(t + \tau)\} = R_\xi(\tau)$, and $E\{\xi_m(t)\xi_k^*(t + \tau)\} = 0$, $0 \leq k, m \leq M_r - 1$, $k \neq m$. In our framework we assume that $R_\xi(\tau)$ is known[4]. In practice $\boldsymbol{z}(t)$ is

---

[4]Although it is possible to reformulate the algorithm to estimate the noise covariance [14], [29], we will leave this aspect outside the scope of this work.

low-pass filtered and sampled with the sampling period T_s, resulting in M_r N-tuples, with N being the number of output samples per sensor. By stacking the sampled outputs of the M_r sensors in one vector $\boldsymbol{z}$, (1) can be rewritten as

$$\boldsymbol{z} = \sum_{l=1}^{L} w_l \boldsymbol{s}(\boldsymbol{\theta}_l) + \boldsymbol{\xi}, \tag{2}$$

where we define $\boldsymbol{s}(\boldsymbol{\theta}_l) = [\boldsymbol{s}_0(\boldsymbol{\theta}_l)^T, \ldots, \boldsymbol{s}_{M_r-1}(\boldsymbol{\theta}_l)^T]^T$, $\boldsymbol{\xi} = [\boldsymbol{\xi}_0^T, \ldots, \boldsymbol{\xi}_{M_r-1}^T]^T$, with $\boldsymbol{s}_p(\boldsymbol{\theta}_l) = [s_p(0, \boldsymbol{\theta}_l), \ldots, s_p((N-1)T_s, \boldsymbol{\theta}_l)]^T$, and $\boldsymbol{\xi}_p = [\xi_p(0), \ldots, \xi_p((N-1)T_s)]^T$, $p = 0, \ldots, M_r - 1$. Finally, we define $\boldsymbol{\Omega} = \{w_1, \boldsymbol{\theta}_1, \ldots, w_L, \boldsymbol{\theta}_L\}$.

The probabilistic graph depicted in Fig. 1(a) encodes the dependencies between the parameters and the observation vector in the model (2). According to the graph structure, the joint density of the graph

(a)   (b)
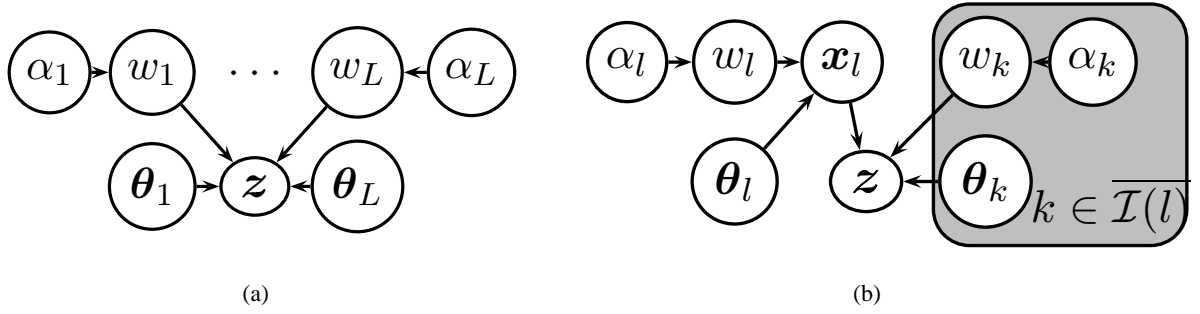
Fig. 1.   a) Graphical model representing (2) with L components; b) extended model with the admissible hidden data $\boldsymbol{x}_l$.

variables can be factored as $p(\boldsymbol{z}, \boldsymbol{\Omega}, \boldsymbol{\alpha}) = p(\boldsymbol{z}|\boldsymbol{\Omega})p(\boldsymbol{\Omega}|\boldsymbol{\alpha})p(\boldsymbol{\alpha})$, where $\boldsymbol{\alpha} = [\alpha_1, \ldots, \alpha_L]^T$ is the vector containing the model sparsity parameters. Let us now specify the statistical model behind the involved variables.

Under the Gaussian noise assumption, $p(\boldsymbol{z}|\boldsymbol{\Omega}) = CN(\boldsymbol{z}; \sum_{l=1}^{L} w_l \boldsymbol{s}(\boldsymbol{\theta}_l), \boldsymbol{\Sigma})$, where $\boldsymbol{\Sigma} = E\{\boldsymbol{\xi}\boldsymbol{\xi}^H\}$. The second term $p(\boldsymbol{\Omega}|\boldsymbol{\alpha})$ is the parameter prior. We assume that $p(\boldsymbol{\Omega}|\boldsymbol{\alpha}) = \prod_{l=1}^{L} p(w_l|\alpha_l)p(\boldsymbol{\theta}_l)$, where $p(w_l|\alpha_l)$ is the sparsity prior for the lth component. The purpose of the sparsity prior is, on the one hand, to constrain the gains $w_1, \ldots, w_L$ of the components, and thus implement sparsification/model order selection, and, on the other hand, to control this constraint through the sparsity parameters $\boldsymbol{\alpha}$. We will study two choices for $p(w_l|\alpha_l)$: i) a Gaussian prior, and ii) a Laplace prior. In both cases the prior pdfs are complex circularly symmetric, with the non-negative hyperparameter α_l inversely proportional to their width. Thus, large values of α_l will render the contribution of the component $w_l \boldsymbol{s}(\boldsymbol{\theta}_l)$ 'irrelevant', since the corresponding prior over w_l will then be concentrated at the origin. The choice of the prior $p(\boldsymbol{\theta}_l)$ is arbitrary; however, it must reflect the underlying physics and restrictions of the measurement

equipment; a non-informative prior can also be used. The prior $p(\alpha_l)$, also called the hyperprior of the lth component, is selected as a Gamma pdf $Ga(\alpha_l; a_l, b_l) = \frac{b_l^{a_l}}{\Gamma(a_l)} \alpha_l^{a_l - 1} \exp(-b_l \alpha_l)$. Practically we set $a_l = b_l = 10^{-7}$ for all components to render their hyperpriors non-informative [13], [14]. Such formulation of a hyperprior pdf $p(\boldsymbol{\alpha}) = \prod_l p(\alpha_l)$ is related to automatic relevance determination [18], [30].

III. PARAMETER ESTIMATION FRAMEWORK

Direct evaluation of $p(\boldsymbol{z}, \boldsymbol{\Omega}, \boldsymbol{\alpha})$ or of the posterior $p(\boldsymbol{\Omega}, \boldsymbol{\alpha} | \boldsymbol{z})$ for performing inference of the unknown parameters $\{\boldsymbol{\Omega}, \boldsymbol{\alpha}\}$ is a nontrivial task. Two main reasons for this are the nonlinearity of the model (1) and the statistical dependence of multipath component parameters when $\boldsymbol{z}$ is observed.[5] Approximative techniques might significantly ease the model fitting step. In our work we resort to the variational Bayesian inference framework. The variational Bayesian inference generalizes the classical EM algorithm [27], and provides a tool for estimating distributions of $\{\boldsymbol{\Omega}, \boldsymbol{\alpha}\}$. Essentially, variational methods approximate the posterior pdf of interest with a simpler one (by, e.g. neglecting some statistical dependencies between random variables) such that the Kullback-Leibler divergence between the former pdf and the later pdf is minimized.

When estimating parameters using the SAGE algorithm [3], [28], the concept of complete data in the EM algorithm is replaced by that of admissible hidden data. The purpose of the admissible hidden data is to make the update procedure for only a subset $\boldsymbol{\Omega}_{\text{sub}} \subset \boldsymbol{\Omega}$ a tractable optimization problem. For the variable $\boldsymbol{x}_{\text{sub}}$ to be an admissible hidden data with respect to $\boldsymbol{\Omega}_{\text{sub}}$ the following factorization must be satisfied: $p(\boldsymbol{z}, \boldsymbol{x}_{\text{sub}}, \boldsymbol{\Omega}) = p(\boldsymbol{z} | \boldsymbol{x}_{\text{sub}}, \{\boldsymbol{\Omega} \setminus \boldsymbol{\Omega}_{\text{sub}}\}) p(\boldsymbol{x}_{\text{sub}}, \boldsymbol{\Omega})$ [28]. The fact that $\boldsymbol{x}_{\text{sub}}$ is an admissible hidden data guarantees that the likelihood of the new parameter update $\boldsymbol{\Omega}'$ (obtained by replacing the updated parameter subset $\boldsymbol{\Omega}'_{\text{sub}}$ in the overall parameter set $\boldsymbol{\Omega}$) cannot be smaller than the likelihood prior to the update [28]. This property is referred to as the Monotonicity Property. The concept of admissible hidden data can be exploited within the variational framework as well. As we will show later this similarly leads to an iterative algorithm – we call it the Variational Bayesian SAGE algorithm – that still exhibits the Monotonicity Property in terms of the variational free energy [27].

Consider for a specific component l the new variable

$$\boldsymbol{x}_l = w_l \boldsymbol{s}(\boldsymbol{\theta}_l) + \boldsymbol{\xi}_l, \tag{3}$$

---

[5]Such graph structure is also referred to as a V-structure [31], which leads to the conditional dependence of the parent variables when the child node is observed.

which can be conceived as a received signal associated with the lth propagation path. The additive noise component $\boldsymbol{\xi}_l$ in (3) is obtained by arbitrarily decomposing the total noise $\boldsymbol{\xi}$, such that $\boldsymbol{\Sigma}_l = E\{\boldsymbol{\xi}_l \boldsymbol{\xi}_l^H\} = \beta_l \boldsymbol{\Sigma}$, and $0 \le \beta_l \le 1$. We define $\boldsymbol{\Delta}_l = (1 - \beta_l)\boldsymbol{\Sigma}$ to be the part of the total additive noise that is not associated with the lth component. Thus, $\boldsymbol{\Delta}_l + \boldsymbol{\Sigma}_l = \boldsymbol{\Sigma}$. Consider now the modified graph in Fig. 1(b) that accounts for $\boldsymbol{x}_l$. It is straight-forward to show that $\boldsymbol{x}_l$ is an admissible hidden data with respect to the subset $\{w_l, \boldsymbol{\theta}_l, \alpha_l\}$. Since we are interested in estimating all L components, we can formulate the estimation algorithm as a succession of L estimations of $\{\boldsymbol{\theta}_l, w_l, \alpha_l\}$ with respect to $\boldsymbol{x}_l$, $l = 1, \ldots, L$, assuming that $\{w_k, \boldsymbol{\theta}_k, \alpha_k\}$, $k \in \overline{\mathcal{I}(l)}$, are known and fixed. According to the extended graph in Fig. 1(b), the joint density $p(\boldsymbol{z}, \boldsymbol{x}_l, \boldsymbol{\Omega}, \boldsymbol{\alpha})$ now factors as

$$p(\boldsymbol{z}|\boldsymbol{x}_l, \boldsymbol{\theta}_{\overline{\mathcal{I}(l)}}, w_{\overline{\mathcal{I}(l)}}) \prod_{k \in \overline{\mathcal{I}(l)}} p(\boldsymbol{\theta}_k) p(w_k|\alpha_k) p(\alpha_k)$$

$$\times p(\boldsymbol{x}_l|w_l, \boldsymbol{\theta}_l) p(w_l|\alpha_l) p(\boldsymbol{\theta}_l) p(\alpha_l),$$

(4)

where

$$p(\boldsymbol{z}|\boldsymbol{x}_l, \boldsymbol{\theta}_{\overline{\mathcal{I}(l)}}, w_{\overline{\mathcal{I}(l)}}) = CN(\boldsymbol{z}; \boldsymbol{x}_l + \sum_{k \in \overline{\mathcal{I}(l)}} w_k \boldsymbol{s}(\boldsymbol{\theta}_k), \boldsymbol{\Delta}_l),$$

(5)

and $p(\boldsymbol{x}_l|w_l, \boldsymbol{\theta}_l) = CN(\boldsymbol{x}_l; w_l \boldsymbol{s}(\boldsymbol{\theta}_l), \boldsymbol{\Sigma}_l)$.

A. Variational Bayesian inference of signal parameters

Bayesian variational inference [27] is a family of techniques that exploit analytical approximations of the posterior pdf of interest, i.e., $p(\boldsymbol{\Omega}, \boldsymbol{\alpha}|\boldsymbol{z})$, using a simpler proxy pdf $q(\boldsymbol{\Omega}, \boldsymbol{\alpha})$. The latter pdf is estimated as a minimizer of the variational free energy $\mathcal{F}(q(\boldsymbol{\Omega}, \boldsymbol{\alpha})\|p(\boldsymbol{\Omega}, \boldsymbol{\alpha}, \boldsymbol{z}))$ [27], which is formally equivalent to the Kullback-Leibler divergence $\mathrm{D_{KL}}(q(\boldsymbol{\Omega}, \boldsymbol{\alpha})\|p(\boldsymbol{\Omega}, \boldsymbol{\alpha}, \boldsymbol{z}))$ between the proxy pdf and the true joint pdf. The admissible hidden data, used in the SAGE algorithm to facilitate the maximization of the parameter likelihood, can also be used within the variational inference framework to ease the minimization of the variational free energy. Such algorithm we term a Variational Bayesian SAGE (VB-SAGE) algorithm.

Essentially, the VB-SAGE algorithm approximates $p(\boldsymbol{\Omega}, \boldsymbol{\alpha}, \boldsymbol{x}_l, \boldsymbol{z})$ with a variational proxy pdf

$$q(\boldsymbol{\Omega}, \boldsymbol{\alpha}, \boldsymbol{x}_l) = q(\boldsymbol{x}_l) \prod_{k=1}^{L} q(w_k) q(\boldsymbol{\theta}_k) q(\alpha_k)$$

(6)

by performing minimization of the free energy with respect to the parameter of the lth component only, and cycling through all L components in a "round-robin" fashion. The Monotonicity Property of the

VB-SAGE algorithm (see Appendix A) ensures that such sequential optimization necessarily decreases the free energy $\mathcal{F}(q(\mathbf{\Omega}, \boldsymbol{\alpha}) \| p(\mathbf{\Omega}, \boldsymbol{\alpha}, \boldsymbol{z}))$.

It is straightforward to show that with the factorization (6) the estimation of any factor $q(a)$, $a \in \{w_{\mathcal{I}}, \boldsymbol{\theta}_{\mathcal{I}}, \alpha_{\mathcal{I}}, \boldsymbol{x}_l\}$, requires the Markov blanket $\mathcal{MB}(a)$ [31] of a to be known.[6] Define now

$$\tilde{p}(a) \propto \exp\left(\mathbb{E}_{q(\mathcal{MB}(a))}\big\{\log p(a|\mathcal{MB}(a))\big\}\right). \tag{7}$$

The unconstrained solution for $q(a)$ that minimizes the corresponding free energy is then simply found as $q(a) = \tilde{p}(a)$. Clearly, an unconstrained solution is preferred; however, we might constrain $q(a)$ to belong to some class of density functions $\mathcal{Q}(a)$ to make the optimization tractable. In this case the approximate solution is obtained by solving

$$q(a) = \underset{q^*(a) \in \mathcal{Q}(a)}{\operatorname{argmin}} \mathrm{D}_{\mathrm{KL}}(q^*(a) \| \tilde{p}(a)). \tag{8}$$

In the case of $\boldsymbol{x}_l$ it is straightforward to show that $\tilde{p}(\boldsymbol{x}_l)$ is quadratic in $\boldsymbol{x}_l$; therefore $\tilde{p}(\boldsymbol{x}_l)$ is a Gaussian pdf, and $q(\boldsymbol{x}_l) = CN(\boldsymbol{x}_l; \widehat{\boldsymbol{x}}_l, \widehat{\boldsymbol{S}}_l^x)$. We stress that the constraint $q(\boldsymbol{x}_l) = \tilde{p}(\boldsymbol{x}_l)$ guarantees the monotonicity of the VB-SAGE algorithm, as we show in the Appendix A. Similarly, we select $\mathcal{Q}(w_l)$ as the set of Gaussian pdfs, i.e., $q(w_l) = CN(w_l; \widehat{w}_l, \widehat{\Phi}_l)$; notice that $q(w_l) = \tilde{p}(w_l)$ only when $p(w_l|\alpha_l)$ is a Gaussian pdf. For the sparsity parameters α_l we select $\mathcal{Q}(\alpha_l)$ as the set of Gamma pdfs, i.e., $q(\alpha_l) = Ga(\alpha_l; \widehat{a}_l, \widehat{b}_l)$. This choice is dictated by the Gamma distribution being the conjugate prior for the inverse variance of the normal distribution; as a result, in the Gaussian prior case $q(\alpha_l) = \tilde{p}(\alpha_l)$. We select $\mathcal{Q}(\boldsymbol{\theta}_l)$ as the set of Dirac measures on the range of $\boldsymbol{\theta}_l$; thus, $q(\boldsymbol{\theta}_l) = \delta(\boldsymbol{\theta}_l - \widehat{\boldsymbol{\theta}}_l)$. By doing so we restrict ourselves to point estimates of the dispersion parameters.[7] The parameters $\widehat{\boldsymbol{x}}_l$, $\widehat{\boldsymbol{S}}_l^x$, $\widehat{\boldsymbol{\theta}}_l$, $\widehat{a}_l$, $\widehat{b}_l$, $\widehat{w}_l$, and $\widehat{\Phi}_l$ are called variational parameters. Obviously, knowing the pdf $q(\mathbf{\Omega}, \boldsymbol{\alpha}, \boldsymbol{x}_l)$ translates into knowing the variational parameters of its factors and vice-versa.

B. Variational estimation expressions

Just like SAGE, the VB-SAGE algorithm is implemented in a sequential manner. For the model with L signal components we start with $l = 1$ and update factors $q(\boldsymbol{x}_l)$, $q(\boldsymbol{\theta}_l)$, $q(w_l)$, and $q(\alpha_l)$ related to the lth component, i.e., we update the corresponding variational parameters, assuming that the approximating

---

[6]For a given Bayesian network with $\mathcal{O}$ variables, a Markov Blanket of a variable a is the smallest subset of variables $\mathcal{MB}(a) \subseteq \mathcal{O}$ that 'shields' a from the rest of the variables $\mathcal{R} = \mathcal{O} \setminus \{a, \mathcal{MB}(a)\}$ in the sense that $p(a|\mathcal{MB}(a), \mathcal{R}) = p(a|\mathcal{MB}(a))$.

[7]Considering more complex forms of $q(\boldsymbol{\theta}_l)$ would require $s(\boldsymbol{\theta}_l)$ to be specialized for a particular antenna structure and measurement setting. A detailed study of this case is outside the scope of this paper.

factors for the other components are known and fixed. In the same fashion the component $l = 2$ is updated, and so on, until all L components are considered. The procedure of updating all parameters of all L components in this way constitutes a single update cycle of the algorithm. The update cycles are repeated anew until convergence.

In what follows, we consider the update expressions for the variational parameters $\{\widehat{\boldsymbol{x}}_l, \widehat{\boldsymbol{S}}_l^x, \widehat{\boldsymbol{\theta}}_l, \widehat{a}_l, \widehat{b}_l, \widehat{w}_l, \widehat{\Phi}_l\}$ of the lth component only. The updated value of a parameter will be denoted by $(\cdot)'$; let us point out that after $q(\boldsymbol{x}_l)$ has been updated, the other factors related to the component l can be updated in any order.

1) Estimation of $q(\boldsymbol{x}_l)$: From the graph in Fig. 1(b) we conclude that $\mathcal{MB}(\boldsymbol{x}_l) = \{\boldsymbol{z}, \boldsymbol{\theta}_{\mathcal{I}}, w_{\mathcal{I}}\}$. Evaluating (7) in this case leads to $\tilde{p}(\boldsymbol{x}_l) \propto p(\boldsymbol{z}|\boldsymbol{x}_l, \widehat{\boldsymbol{\theta}}_{\overline{\mathcal{I}(l)}}, \widehat{w}_{\overline{\mathcal{I}(l)}}) p(\boldsymbol{x}_l|\widehat{w}_l, \widehat{\boldsymbol{\theta}}_l)$. Since the right-hand side is a product of Gaussian pdfs, $\tilde{p}(\boldsymbol{x}_l)$ is as well a Gaussian pdf, with the mean and covariance matrix given by

$$\widehat{\boldsymbol{x}}_l' = (1 - \beta_l)\widehat{w}_l \boldsymbol{s}(\widehat{\boldsymbol{\theta}}_l) + \beta_l \left(\boldsymbol{z} - \sum_{k \in \overline{\mathcal{I}(l)}} \widehat{w}_k \boldsymbol{s}(\widehat{\boldsymbol{\theta}}_k) \right),$$

$$(\widehat{\boldsymbol{S}}_l^x)' = (\boldsymbol{\Delta}_l^{-1} + \boldsymbol{\Sigma}_l^{-1})^{-1},$$

(9)

and $q(\boldsymbol{x}_l) = \tilde{p}(\boldsymbol{x}_l) = CN(\boldsymbol{x}_l; \widehat{\boldsymbol{x}}_l, \widehat{\boldsymbol{S}}_l^x)$. The result (9) generalizes that obtained in [3] by accounting for the covariance matrix of $\boldsymbol{x}_l$ and for the noise covariance matrix $\boldsymbol{\Sigma}$. Note, however, that the expression for the mean $\widehat{\boldsymbol{x}}_l$ in (9) is identical to that obtained in the SAGE algorithm.

Let us consider the limiting case as $\beta_l \to 1$. It has been show that for models linear in their parameters the choice $\beta_l = 1$ leads to a fast convergence of the algorithm already in the early iteration steps [28]. This is equivalent to assuming that $\boldsymbol{x}_l = \boldsymbol{z} - \sum_{k \in \overline{\mathcal{I}(l)}} w_k \boldsymbol{s}(\boldsymbol{\theta}_k)$, which was also used as an admissible hidden data in [3]. In this case $(\widehat{\boldsymbol{S}}_l^x)' \to 0$ so that $q(\boldsymbol{x}_l)$ collapses to a Dirac distribution, and $\boldsymbol{\Sigma}_l \to \boldsymbol{\Sigma}$.

2) Estimation of $q(\boldsymbol{\theta}_l)$: The Markov blanket of $\boldsymbol{\theta}_l$ is $\mathcal{MB}(\boldsymbol{\theta}_l) = \{w_l, \boldsymbol{x}_l\}$. Here the estimation algorithm profits from the usage of the admissible hidden data $q(\boldsymbol{x}_l)$. Since $q(\boldsymbol{\theta}_l) = \delta(\boldsymbol{\theta}_l - \widehat{\boldsymbol{\theta}}_l)$, finding $q(\boldsymbol{\theta}_l)$ reduces to the computation of $\widehat{\boldsymbol{\theta}}_l$ that maximizes $\tilde{p}(\boldsymbol{\theta}_l)$ given by (7). By noting that $p(\boldsymbol{\theta}_l|w_l, \boldsymbol{x}_l) \propto p(\boldsymbol{x}_l|\boldsymbol{\theta}_l, w_l)p(\boldsymbol{\theta}_l)$ we obtain

$$\widehat{\boldsymbol{\theta}}_l' = \underset{\boldsymbol{\theta}_l}{\operatorname{argmax}} \Big\{ \log p(\boldsymbol{\theta}_l) + $$

$$\log p(\widehat{\boldsymbol{x}}_l|\boldsymbol{\theta}_l, \widehat{w}_l) - \widehat{\Phi}_l \boldsymbol{s}(\boldsymbol{\theta}_l)^H \boldsymbol{\Sigma}_l^{-1} \boldsymbol{s}(\boldsymbol{\theta}_l) \Big\}.$$

(10)

Notice that due to $q(w_l)$ being a Gaussian pdf within the VB-SAGE framework, (10) includes a Tikhonov-like regularization term $\widehat{\Phi}_l \boldsymbol{s}(\boldsymbol{\theta}_l)^H \boldsymbol{\Sigma}_l^{-1} \boldsymbol{s}(\boldsymbol{\theta}_l)$, with the posterior variance $\widehat{\Phi}_l$ of w_l acting as a regularization constant. Unfortunately, since $\boldsymbol{s}(\boldsymbol{\theta}_l)$ depends nonlinearly on $\boldsymbol{\theta}_l$, (10) has to be optimized numerically, e.g., using successive line searches where each element of $\widehat{\boldsymbol{\theta}}_l$ is determined separately, or using a joint search in which all elements of $\widehat{\boldsymbol{\theta}}_l$ are computed jointly; if derivatives of the objective function (10) with respect to $\boldsymbol{\theta}_l$ are available, gradient-based optimization schemes can also be used.

Typically $q(\boldsymbol{\theta}_l)$ is selected to factorize according to $q(\boldsymbol{\theta}_l) = q(\theta_{1l}) \cdot \ldots \cdot q(\theta_{Ml})$, where M is the number of dispersion parameters describing a multipath component.[8] Estimating θ_{ml} can be done by evaluating (7) using $\mathcal{MB}(\theta_{ml}) = \{\mathcal{MB}(\boldsymbol{\theta}_l) \bigcup \{\boldsymbol{\theta}_l \setminus \theta_{ml}\}\}$ and performing a simple line search of the resulting objective function. Notice that the same assumption underpins the SAGE-based estimation of $\boldsymbol{\theta}_l$. The VB-SAGE estimation expression for $\boldsymbol{\theta}_l$ in (10) will coincide with that of the standard SAGE when $p(\boldsymbol{\theta}_l)$ is assumed non-informative and $q(w_l) = \delta(w_l - \widehat{w}_l)$.

3) Estimation of $q(w_l)$: The Markov blanket for w_l is $\mathcal{MB}(w_l) = \{\boldsymbol{\theta}_l, \boldsymbol{x}_l, \alpha_l\}$. Evaluating (7) leads to $\tilde{p}(w_l) \propto p(\widehat{\boldsymbol{x}}_l | w_l, \widehat{\boldsymbol{\theta}}_l) p(w_l | \widehat{\alpha}_l)$. For a given choice of $p(w_l | \alpha_l)$ the moments of $q(w_l) = CN(w_l; \widehat{w}_l, \widehat{\Phi}_l)$ can be either found in closed form, or efficiently approximated. We defer the estimation of these moments to Section IV, where different priors $p(w_l | \alpha_l)$ are discussed.

4) Estimation of $q(\alpha_l)$: Here $\mathcal{MB}(\alpha_l) = \{w_l\}$. Observe that in contrast to $q(\boldsymbol{\theta}_l)$ and $q(w_l)$, the admissible hidden data $\boldsymbol{x}_l$ is not in $\mathcal{MB}(\alpha_l)$. This is the result of the Markov chain $\alpha_l \to w_l \to \boldsymbol{x}_l$; in fact, w_l is the admissible hidden data for estimating α_l since $p(\boldsymbol{x}_l, w_l | \alpha_l, \boldsymbol{\theta}_l) = p(\boldsymbol{x}_l | w_l, \boldsymbol{\theta}_l) p(w_l | \alpha_l)$ due to the factorization (4). By noting that $p(\alpha_l | w_l) \propto p(w_l | \alpha_l) p(\alpha_l)$, (7) can be rewritten as $\tilde{p}(\alpha_l) \propto p(\alpha_l) \exp \left(\mathbb{E}_{q(w_l)} \{\log p(w_l | \alpha_l)\} \right)$. Due to the fact that $q(\alpha_l) = Ga(\alpha_l; \widehat{a}_l, \widehat{b}_l)$, the variational parameters $\widehat{a}_l$ and $\widehat{b}_l$ are found by equating the moments of $q(\alpha_l)$ and $\tilde{p}(\alpha_l)$. Observe that it is the estimation of $q(\alpha_l)$ that eventually leads to the sparse VB-SAGE algorithm. Also notice that the sparsity prior $p(w_l | \alpha_l)$ is a key to the estimation of the sparsity parameters. In the following section we will consider several choices of $p(w_l | \alpha_l)$ and analyze their effect on sparsity-based model order selection.

IV. Sparsity priors for model order selection

In this section we consider three choices for the sparsity prior $p(w_l | \alpha_l)$: i) a Gaussian prior, which leads to the ℓ_2-type of log-likelihood penalty, ii) a flat prior, obtained as a limiting case of the Gaussian prior when $\alpha_l \to 0$, and iii) a Laplace prior, which results in the ℓ_1-type of log-likelihood penalty.

---

[8]If some of the dispersion parameters are statistically dependent, a structured mean field can be used to account for this dependency by means of an appropriate factorization of the proxy pdf $q(\boldsymbol{\theta}_l)$.

A. Gaussian prior

The Gaussian sparsity prior is obtained by selecting $p(w_l|\alpha_l) = CN(w_l; 0, \alpha_l^{-1})$. With this choice it is straightforward to show that $q(w_l) = \tilde{p}(w_l)$, and that

$$
\begin{aligned}
\widehat{\Phi}'_l &= \left(\widehat{\alpha}_l + s(\widehat{\boldsymbol{\theta}}_l)^H \boldsymbol{\Sigma}_l^{-1} s(\widehat{\boldsymbol{\theta}}_l)\right)^{-1}, \\
\widehat{w}'_l &= \widehat{\Phi}'_l s(\widehat{\boldsymbol{\theta}}_l)^H \boldsymbol{\Sigma}_l^{-1} \widehat{\boldsymbol{x}}_l.
\end{aligned}
\tag{11}
$$

Observe that (11) is merely a regularized least-squares estimate of $\widehat{w}'_l$ given $\widehat{\boldsymbol{x}}_l, \widehat{\boldsymbol{\theta}}_l$, with the regularization parameter $\widehat{\alpha}_l = \mathbb{E}_{q(\alpha_l)}\{\alpha_l\} = \widehat{a}_l / \widehat{b}_l$.

The variational parameters $\widehat{a}_l$ and $\widehat{b}_l$ of $q(\alpha_l)$ are found from $\tilde{p}(\alpha)$. This requires the expectation of $|w_l|^2$ to be computed. Doing so leads to the following update expressions:

$$
\widehat{a}'_l = a_l + 1, \quad \widehat{b}'_l = b_l + (|\widehat{w}_l|^2 + \widehat{\Phi}_l).
\tag{12}
$$

Let us now analyze (12) in more details for the case $a_l = b_l = 0$, i.e., when $p(\alpha_l)$ is non-informative. In this case the mean of $q(\alpha_l)$ is given as

$$
\widehat{\alpha}'_l = \frac{1}{|\widehat{w}_l|^2 + \widehat{\Phi}_l}.
\tag{13}
$$

Note that this result coincides with the EM-based evidence estimation proposed in [11], [14]. However, in our case both $\widehat{w}_l$ and $\widehat{\Phi}_l$ are estimated using the admissible hidden data $\boldsymbol{x}_l$, as opposed to [11], [14] where the incomplete data $\boldsymbol{z}$ is used to obtain these estimates. The updating steps in (11) and (13) can be alternatively repeated, while keeping $\widehat{\boldsymbol{x}}_l$ and $\widehat{\boldsymbol{\theta}}_l$ fixed to generate a sequence $\{\widehat{\alpha}_l^{[m]}\}_{m>0}$, where $\widehat{\alpha}_l^{[1]} = \widehat{\alpha}'_l, \widehat{\alpha}_l^{[2]} = \widehat{\alpha}''_l$, etc. Note that this updating process makes sense since neither $\boldsymbol{x}_l$ nor $\boldsymbol{\theta}_l$ are in $\mathcal{MB}(\alpha_l)$.[9] Therefore, the corresponding sequence of pdfs $\{q^{[m]}(\alpha_l) = Ga(\alpha_l; \widehat{a}_l^{[m]}, \widehat{b}_l^{[m]})\}_{m>0}$ necessarily monotonically decreases the variational free energy with respect to $q(\alpha_l)$. Let $\widehat{\alpha}_l^{[\infty]}$ be the stationary point of the sequence $\{\widehat{\alpha}_l^{[m]}\}_{m>0}$ when $m \to \infty$. In order to simplify the notation we define $\widehat{\boldsymbol{s}}_l \equiv s(\widehat{\boldsymbol{\theta}}_l)$. By substituting (11) into (13) and solving for $\widehat{\alpha}_l^{[\infty]}$ we obtain (see also [19])

$$
\widehat{\alpha}_l^{[\infty]} = \frac{(\widehat{\boldsymbol{s}}_l^H \boldsymbol{\Sigma}_l^{-1} \widehat{\boldsymbol{s}}_l)^2}{|\widehat{\boldsymbol{s}}_l^H \boldsymbol{\Sigma}_l^{-1} \widehat{\boldsymbol{x}}_l|^2 - \widehat{\boldsymbol{s}}_l^H \boldsymbol{\Sigma}_l^{-1} \widehat{\boldsymbol{s}}_l}.
\tag{14}
$$

---

[9]Notice that this property allows for a straightforward extension of the subsequent analysis to the estimation of sparse virtual channel models [16] since it remains valid even when the dispersion parameters $\boldsymbol{\theta}_l$ are constrained to some resolution grid.

By definition $\widehat{\alpha}_l^{[\infty]} > 0$, which is satisfied if, and only, if

$$|\widehat{\boldsymbol{s}}_l^H \boldsymbol{\Sigma}_l^{-1} \widehat{\boldsymbol{x}}_l|^2 > \widehat{\boldsymbol{s}}_l^H \boldsymbol{\Sigma}_l^{-1} \widehat{\boldsymbol{s}}_l. \tag{15}$$

By interpreting (13) as a nonlinear dynamic mapping, which at the iteration m maps $\widehat{\alpha}_l^{[m]}$ into $\widehat{\alpha}_l^{[m+1]}$, it can be shown [19] that for $|\widehat{\boldsymbol{s}}_l^H \boldsymbol{\Sigma}_l^{-1} \widehat{\boldsymbol{x}}_l|^2 \leq \widehat{\boldsymbol{s}}_l^H \boldsymbol{\Sigma}_l^{-1} \widehat{\boldsymbol{s}}_l$ the fixed point of the mapping is at infinity, i.e., $\widehat{\alpha}_l^{[\infty]} = \infty$. As a result, the lth signal component can be removed from the model.[10] A similar result was reported in [17] using a non-variational analysis of the marginal log-likelihood function. This allows us to implement model order selection during a parameter update iteration (i.e., joint multipath component detection and parameter estimation), while still minimizing the variational free energy.

Now, let us reinspect (15). This inequality might at first glance seem a bit counter-intuitive – the quadratic quantity on the right-hand side is compared to the fourth-power quantity on the left-hand side. In order to better understand the meaning of it, let us divide both sides of (15) by $(\widehat{\alpha}_l^{[\infty]} + \widehat{\boldsymbol{s}}_l^H \boldsymbol{\Sigma}_l^{-1} \widehat{\boldsymbol{s}}_l)^2$. It follows that (15) is equivalent to

$$|\widehat{w}_l^{[\infty]}|^2 > \gamma_l \frac{1}{\widehat{\alpha}_l^{[\infty]} + \widehat{\boldsymbol{s}}_l^H \boldsymbol{\Sigma}_l^{-1} \widehat{\boldsymbol{s}}_l} = \gamma_l \widehat{\Phi}_l^{[\infty]}, \tag{16}$$

where $\gamma_l = \frac{\widehat{\boldsymbol{s}}_l^H \boldsymbol{\Sigma}_l^{-1} \widehat{\boldsymbol{s}}_l}{\widehat{\alpha}_l^{[\infty]} + \widehat{\boldsymbol{s}}_l^H \boldsymbol{\Sigma}_l^{-1} \widehat{\boldsymbol{s}}_l} \leq 1$. The left-hand term in (16) is an estimate of the posterior variance of w_l scaled by γ_l. This result leads directly to several important observations:

1) The sparsity parameter $\widehat{\alpha}_l^{[\infty]}$ of the signal component l with $|\widehat{w}_l^{[\infty]}|^2$ smaller than its posterior variance $\widehat{\Phi}_l^{[\infty]}$ scaled by γ_l is infinite, and thus such components can be removed from the model.

2) By multiplying both sides of (16) with $\widehat{\boldsymbol{s}}_l^H \boldsymbol{\Sigma}_l^{-1} \widehat{\boldsymbol{s}}_l$, we find that this inequality is equivalent to $\widehat{SNR}_l > \gamma_l^2$, where $\widehat{SNR}_l = |\widehat{w}_l^{[\infty]}|^2 \widehat{\boldsymbol{s}}_l^H \boldsymbol{\Sigma}_l^{-1} \widehat{\boldsymbol{s}}_l$ is the estimated signal-to-noise ratio of the lth component. Thus condition (15) (and (16)) corresponds to keeping this component provided $\widehat{SNR}_l > \gamma_l^2$.

3) Condition (15) can be tuned to retain the component provided its estimated SNR is above some predefined level $SNR' \geq \gamma_l^2$ using the modified condition

$$|\widehat{\boldsymbol{s}}_l^H \boldsymbol{\Sigma}_l^{-1} \widehat{\boldsymbol{x}}_l|^2 > \widehat{\boldsymbol{s}}_l^H \boldsymbol{\Sigma}_l^{-1} \widehat{\boldsymbol{s}}_l \times \frac{SNR'}{\gamma_l^2}. \tag{17}$$

These results provide us with the required instruments to determine whether a component l with the sparsity parameter α_l should be updated or pruned: if the component l fails to satisfy (15), it is

---

[10]Strictly speaking, this is true only in the case of non-informative hyperprior $p(\alpha_l)$.

removed since for $\widehat{\alpha}_l^{[\infty]} \to \infty$, $\widehat{w}_l^{[\infty]} \to 0$. In case of (17) we remove the component if its estimated SNR is below some level $SNR' \geq \gamma_l^2$. Notice that the obtained results allow for an interpretation of the sparsity parameter α_l in terms of estimated SNR of the lth component. Thus, model order selection (sparsification) can be realized using simple SNR-guided decisions. It should be stressed that the analysis of (14) is possible only due to the use of the admissible hidden data $\boldsymbol{x}_l$. A standard approach with Gaussian priors [11], [14], [17] requires an $L \times L$ posterior covariance matrix $\widehat{\boldsymbol{\Phi}}$ of the gain coefficient vector $\boldsymbol{w} = [w_1, \ldots, w_L]^T$ to be computed. This significantly complicates the analytical computation of the fixed point $\widehat{\alpha}_l^{[\infty]}$ and its analysis. The sparse VB-SAGE algorithm with Gaussian sparsity priors and model order selection scheme that utilizes (15) or (17) we denote as the VB-SAGE-G algorithm.

B. Flat priors

In the case where $p(w_l | \alpha_l)$ is chosen to be non-informative, we can still make use of the Bayesian sparsity to estimate the model order. This can be done by using the VB-SAGE-G algorithm in the limiting case as $\widehat{\alpha}_l \to 0$ (i.e., $\widehat{b}_l \to \infty$). Due to the structure of the graph (see Fig. 1(b)), this will only affect the moments of $q(w_l)$, which remain identical to (11) with $\widehat{\alpha}_l = 0$. Clearly, in this case $\gamma_l = 1$ and condition (16) corresponds to the sparsification of the lth component provided $\widehat{SNR}_l > 1$, i.e., we keep the component when its SNR is above 0dB. The sparse VB-SAGE algorithm with such model order selection scheme we denote as the VB-SAGE-F algorithm. Observe that condition (17) can also be used in the case of the VB-SAGE-F algorithm.

C. Laplace priors (soft thresholding)

As the last choice we consider a Laplace prior $p(w_l | \alpha_l)$. We will use an analogous Laplace prior in the complex domain defined as

$$p(w_l | \alpha_l) = \frac{2\alpha_l^2}{\pi} \exp(-2\alpha_l |w_l|). \tag{18}$$

The mean of $q(w_l)$ can be obtained in closed form:

$$\widehat{w}_l' = \mathrm{sign}(\boldsymbol{s}(\widehat{\boldsymbol{\theta}}_l)^H \boldsymbol{\Sigma}_l^{-1} \widehat{\boldsymbol{x}}_l) \times$$
$$\frac{\max(0, |\boldsymbol{s}(\widehat{\boldsymbol{\theta}}_l)^H \boldsymbol{\Sigma}_l^{-1} \widehat{\boldsymbol{x}}_l| - \widehat{\alpha}_l)}{\boldsymbol{s}(\widehat{\boldsymbol{\theta}}_l)^H \boldsymbol{\Sigma}_l^{-1} \boldsymbol{s}(\widehat{\boldsymbol{\theta}}_l)}. \tag{19}$$

Here $\mathrm{sign}(\cdot)$ is the sign function defined as $\mathrm{sign}(x) = x/|x|$. Expression (19) is also known as a *soft thresholding* rule. To our best knowledge no closed form expression for the posterior variance exists.

However, we can approximate it with the result obtained for the real-valued $w_l \neq 0$, which is given as

$$\widehat{\Phi}'_l \approx \left(s(\widehat{\boldsymbol{\theta}}_l)^H \boldsymbol{\Sigma}_l^{-1} s(\widehat{\boldsymbol{\theta}}_l) \right)^{-1}. \tag{20}$$

Now we turn to the estimation of the sparsity parameter α_l. By plugging (18) in the expression for $\tilde{p}(\alpha_l)$, and ignoring terms independent of α_l, we obtain $\tilde{p}(\alpha_l) \propto p(\alpha_l)\alpha_l^2 \exp\left(-2\alpha_l \mathbb{E}_{q(w)}\{|w_l|\}\right)$. Since $q(w_l)$ is Gaussian, $|w_l|$ follows a Rice distribution characterized by the parameters $|\widehat{w}_l|$ (19) and $\sqrt{\widehat{\Phi}_l/2}$ (20). The expectation $\mathbb{E}_{q(w)}\{|w_l|\}$ is then given as $\sqrt{\widehat{\Phi}_l \pi/4}\mathcal{L}_{1/2}(-|\widehat{w}_l|^2/\widehat{\Phi}_l)$, where $\mathcal{L}_\nu(x)$ denotes the Laguerre polynomial with degree ν. To simplify the estimation of $q(\alpha_l)$, we consider an approximation of $\mathbb{E}_{q(w)}\{|w_l|\}$ as $|\widehat{w}_l|^2/\widehat{\Phi}_l \to \infty$. This approximation is equivalent to assuming a high precision estimate of w_l. In this case $\mathbb{E}_{q(w)}\{|w_l|\} = |\widehat{w}_l|$. Then, it is straightforward to show that

$$\widehat{a}'_l = a_l + 2, \quad \widehat{b}'_l = b_l + 2|\widehat{w}_l|. \tag{21}$$

By selecting a non-informative prior $p(\alpha_l)$, the update expression for the mean $\widehat{\alpha}'_l = \widehat{a}'_l/\widehat{b}'_l$ simplifies to

$$\widehat{\alpha}'_l = 1 \Big/ |\widehat{w}_l|. \tag{22}$$

Similar to the Gaussian prior case we analyze the fixed point $\widehat{\alpha}_l^{[\infty]}$ of (22). We define $\widehat{s}_l \equiv s(\widehat{\boldsymbol{\theta}}_l)$ to simplify the notation. Combining (22) and (19) leads to

$$\widehat{\alpha}_l^{[\infty]} = \frac{\widehat{s}_l^H \boldsymbol{\Sigma}_l^{-1}\widehat{s}_l}{\max(0, |\widehat{s}_l^H \boldsymbol{\Sigma}_l^{-1}\widehat{x}_l| - \alpha_l^{[\infty]})}. \tag{23}$$

Assuming that $|\widehat{s}_l^H \boldsymbol{\Sigma}_l^{-1}\widehat{x}_l| > \alpha_l^{[\infty]}$ (otherwise $\alpha_l^{[\infty]} = \infty$), we solve for $\alpha_l^{[\infty]}$. Doing so yields two solutions:

$$\alpha_{l,+}^{[\infty]} = \frac{1}{2}\left(|\widehat{s}_l^H \boldsymbol{\Sigma}_l^{-1}\widehat{x}_l| + \mu_l\right), \tag{24}$$

$$\alpha_{l,-}^{[\infty]} = \frac{1}{2}\left(|\widehat{s}_l^H \boldsymbol{\Sigma}_l^{-1}\widehat{x}_l| - \mu_l\right), \tag{25}$$

where $\mu_l = \sqrt{|\widehat{s}_l^H \boldsymbol{\Sigma}_l^{-1}\widehat{x}_l|^2 - 4\widehat{s}_l^H \boldsymbol{\Sigma}_l^{-1}\widehat{s}_l}$. Furthermore, we see that a necessary and sufficient condition for the fixed points to be real is that

$$|\widehat{s}_l^H \boldsymbol{\Sigma}_l^{-1}\widehat{x}_l|^2 \geq 4\widehat{s}_l^H \boldsymbol{\Sigma}_l^{-1}\widehat{s}_l. \tag{26}$$

Components that do not satisfy (26) are removed. Note that both fixed points are feasible. We have always empirically observed that when the initial $q(\alpha_l)$ is chosen such that $\widehat{\alpha}_l = 0$, iterations (22) either

diverge ($\alpha_l^{[\infty]} = \infty$) or converge to the closest (smallest) feasible solution given by (25). The properties of the second stationary point are subject to further investigations left outside the scope of this paper. The sparse VB-SAGE algorithm with Laplace sparsity priors that makes use of (26) for model order selection we denote as the VB-SAGE-L algorithm. Similarly to (16) it can be shown that (26) is equivalent to

$$|\widehat{w}_l^{[\infty]}|^2 \geq 4\gamma_l^2 \frac{1}{\widehat{s}_l^H \Sigma_l^{-1} \widehat{s}_l} = 4\gamma_l^2 \widehat{\Phi}_l^{[\infty]}, \tag{27}$$

where $\gamma_l = \frac{|\widehat{s}_l^H \Sigma_l^{-1} \widehat{x}_l| - \widehat{\alpha}_l^{[\infty]}}{|\widehat{s}_l^H \Sigma_l^{-1} \widehat{x}_l|} \leq 1$. In the same way (26) and (27) are equivalent to keeping the component provided $\widehat{SNR}_l \geq 4\gamma_l^2$, where $\widehat{SNR}_l = |\widehat{w}_l^{[\infty]}|^2 \widehat{s}_l^H \Sigma_l^{-1} \widehat{s}_l$ is the estimated component SNR. Note that (26) and (27) are the Laplace-prior equivalent conditions of (15) and (16) respectively for the Gaussian prior. Although the pruning conditions are formally similar, they differ in their numerical values: the moments of $q(w_l)$ are estimated differently for the VB-SAGE-L and VB-SAGE-G schemes; as a result, the estimates of the admissible hidden data x_l for the VB-SAGE-L and VB-SAGE-G algorithms are also different; in addition, the scaling factor γ_l in (27) is computed differently from that in (16). It should also be mentioned that as $\alpha_l \to 0$ the VB-SAGE-L algorithm converges to the VB-SAGE-F algorithm.

Similarly to (17), (26) can be tuned to keep the component when its estimated SNR is above some predefined level $SNR' \geq 4\gamma_l^2$ using the modified condition

$$|\widehat{s}_l^H \Sigma_l^{-1} \widehat{x}_l|^2 \geq \widehat{s}_l^H \Sigma_l^{-1} \widehat{s}_l \times \frac{SNR'}{\gamma_l^2}. \tag{28}$$

V. IMPLEMENTATION AND INITIALIZATION OF THE ALGORITHM

A. Summary of the algorithm

Let us now summarize the main steps of the proposed algorithm. For the moment we assume that at some iteration j the approximating factors $q(x_l)$, $q(\theta_l)$, $q(w_l)$, and $q(\alpha_l)$, $l \in \{1, \ldots, \widehat{L}\}$, are known for the $\widehat{L}$ components. A single update iteration for the component l is summarized in Algorithm 1.

This update iteration is repeated for all components in a round-robin fashion, which constitutes a single update cycle of the algorithm. The update cycles are then repeated until the number of components and their variational parameters converge. Observe that the number of components might be reduced during one update cycle: at each iteration the updated multipath component undergoes a test specified by the conditions (15) or (26). When the corresponding condition is not satisfied the component is removed. The model order might also be increased by adding new components. Details of this procedure are outlined in Section V-D.

Algorithm 1 Update iteration for the component l

Update $q(\boldsymbol{x}_l)$ from (9)

Update $q(\boldsymbol{\theta}_l)$ from (10) and evaluate $\boldsymbol{s}(\widehat{\boldsymbol{\theta}}_l')$

if Condition (17)/(28) are TRUE **then**

    Update $q(\alpha_l)$ from (14) (VB-SAGE-G), or (25) (VB-SAGE-L)

    Update $q(w_l)$ from (11) (VB-SAGE-G, -F), or (19) (VB-SAGE-L)

    $\widehat{L}' \leftarrow \widehat{L}$

else

    Remove the l'th component; $\widehat{L}' \leftarrow \widehat{L} - 1$

end if

B. Algorithm initialization

We propose a simple bottom-up initialization strategy, which allows us to infer the initial variational parameters from the observation $\boldsymbol{z}$ by starting with an empty model, i.e., assuming all variational parameters to be 0. The first component is initialized by letting $\widehat{\boldsymbol{x}}_1' = \boldsymbol{z}$ and applying the initialization loop shown in Algorithm 2. Observe that using $\widehat{\boldsymbol{x}}_l'$ the dispersion parameters $\widetilde{\boldsymbol{\theta}}_l'$ are initialized using a simple

---

Algorithm 2 Algorithm initialization

Set $l \leftarrow 1$; initialize $q(\boldsymbol{x}_l)$: $\widehat{\boldsymbol{x}}_1' \leftarrow \boldsymbol{z}$

while Continue initialization **do**

    Initialize $q(\boldsymbol{\theta}_l)$ by computing $\widetilde{\boldsymbol{\theta}}_l' = \operatorname{argmax}_{\boldsymbol{\theta}_l} \left\{ |\boldsymbol{s}(\boldsymbol{\theta}_l)^H \boldsymbol{\Sigma}_l^{-1} \widehat{\boldsymbol{x}}_l'| \big/ \boldsymbol{s}(\boldsymbol{\theta}_l)^H \boldsymbol{\Sigma}_l^{-1} \boldsymbol{s}(\boldsymbol{\theta}_l) \right\}$

    if Condition (15) (VB-SAGE-G, -F) or (26) (VB-SAGE-L) are TRUE **then**

        Initialize $q(w)$ from (11) with $\widehat{\alpha}_l = 0$

        Initialize $q(\alpha_l)$ from (12) (VB-SAGE-G), or (21) (VB-SAGE-L)

        $\widehat{L}' = l$; $l \leftarrow l + 1$

        $\widehat{\boldsymbol{x}}_l' \leftarrow \boldsymbol{z} - \sum_{k=1}^{l-1} \widehat{w}_k' \boldsymbol{s}(\widehat{\boldsymbol{\theta}}_k')$,

    else

        Stop initialization: $\widehat{L}' = l - 1$

    end if

end while

---

beamformer and the obtained estimate of $\boldsymbol{s}(\widehat{\boldsymbol{\theta}}_l')$ is plugged in (15) (in the Gaussian prior case) or in (26) (in the Laplace prior case) to determine whether the initialized component should be kept in the model. When the test fails, the initialization stops. It should be stressed that the use of conditions (15) or (26) during the initialization is optional and may be omitted if an overcomplete channel representation is desired. The components with large sparsity parameters will then be pruned later during the update iterations. This initialization strategy is similar to the successive interference cancellation scheme proposed in [3], [5]. The number of initialization iterations (i.e., the initial number of signal components) can be either fixed

to L_{max}, or inferred automatically by repeating the initialization iterations until the pruning condition (15) (or (26)) fails at some iteration.[11] In our implementation of the algorithm we use a combination of the two methods, by limiting the maximum number of initial components to L_{max}.

1) Noise statistics: A crucial part of the initialization procedure is to obtain an accurate estimate of the variance of the additive noise $\boldsymbol{\xi}$. Logically, when the noise level is high, we tend to put less "trust" in the estimates of the signal parameters, and thus sparsify components more aggressively.

In many cases estimates of the noise variance can be derived from the signal itself. Specifically, the noise variance can be estimated from the tail of the measured CIR. Alternatively, the noise variance can be estimated from the residual signal obtained after completion of the initialization step. In our work we use the former initialization strategy.

2) Selecting $\boldsymbol{\Sigma}_l$: The obtained sparsity expressions for model order selection all depend on the covariance matrix of the additive noise $\boldsymbol{\xi}_l$ associated with the lth multipath component. The covariance matrix $\boldsymbol{\Sigma}_l$ is related to the total covariance matrix $\boldsymbol{\Sigma}$ as $\boldsymbol{\Sigma}_l = \beta_l \boldsymbol{\Sigma}$, where β_l is the noise splitting parameter introduced in the definition of the admissible hidden data (3). In the SAGE algorithm applied to the estimation of superimposed signal parameters [3], this parameter was set to $\beta_l = 1$; we also adopt this choice. Obviously, in this case, $\boldsymbol{\Sigma}_l = \boldsymbol{\Sigma}$, and $\widehat{SNR}_l = |w_l|^2 \boldsymbol{s}(\boldsymbol{\theta}_l)^H \boldsymbol{\Sigma}^{-1} \boldsymbol{s}(\boldsymbol{\theta}_l)$.

C. Stopping criterion for update cycles

The iterative nature of the algorithm requires a stopping criterion for the variational parameter updates. In our implementation we use the following simple criterion: the estimation iterations are terminated when i) the number of signal components stabilizes, and, ii) the maximum change of the components in $\{\boldsymbol{\Omega}, \boldsymbol{\alpha}\}$ between two consecutive update cycles is less than 0.01%.

D. Adaptive model order estimation

The structure of the estimation algorithm also allows increasing the model order. Increasing the model order might be useful when L_{max} is selected too small so that not all physical multipath components might have been discovered. Alternatively, new components might also appear in time-varying scenarios. The new components can be initialized from the residual signal. After the model fitting has been performed at some update cycle, e.g., j, the residual $\widehat{\boldsymbol{x}}'_{L+1} = \boldsymbol{z} - \sum_{l=1}^{L} \widehat{w}_l \boldsymbol{s}(\widehat{\boldsymbol{\theta}}_l)$ is computed and used to initialize

---

[11]We suggest to use the conditions (15) or (26) instead of their modified versions (17) and (28), since this allows for the inclusion of even the weakest components during the initialization.

new components as explained in Sec. V-B. Essentially, the residual signal can be used at any stage of the algorithm to initialize new components.

E. Estimation uncertainty and selection of sensitivity SNR'

There are four main sources of uncertainty in model-based multipath estimation: (i) the inaccuracy of the specular model (1) in representing reality (e.g. in the presence of diffuse components); (ii) the error in calibrating the measurement equipment, which results in an error in the specification of the mapping $u(t) \mapsto s(t, \boldsymbol{\theta}_l)$; (iii) the discrete-time approximation (2) of the model; and (iv) the discrete optimization that is typically necessary due to the nonlinearity of the model versus some of its parameters. All these aspects have a significant impact on the model order estimation. Any deviation from the "true" model (effects (i) and (ii)) and inaccuracies in the parameter estimates $\widehat{\boldsymbol{\Omega}}$ (due to (iii) and (iv)) results in a residual error, manifesting itself as a contribution from fictive additional components. If no penalization of the parameter log-likelihood is used, this error leads to additional signal components being detected, especially in high SNR regime. These non-physical components are numerical artifacts; they do not correspond to any real multipath components. Moreover, these fictive components (which are typically much weaker than the real specular components) create pseudo-clusters since typically their parameters are highly correlated. In the case of the VB-SAGE-G, VB-SAGE-F and VB-SAGE-L algorithms, the artifacts can be efficiently controlled using the pruning conditions (17) and (28) with an appropriately chosen sensitivity level SNR'. The sensitivity level SNR' can be set globally, or can be tuned individually to each multipath component. We propose the following implementation of individual tuning.

First, we consider the impact of all above-mentioned inaccuracies together. This approach is motivated by experimental evidence indicating that (i) each type of inaccuracies has a non-negligible effect on channel estimation, and (ii) that these effects are difficult to quantify and also to separate. Second, we assume that – due to these inaccuracies – the residual error contributed by a given estimated multipath component is proportional to the sample of the delay power profile at the component delay. Indeed, it makes sense to presume that the stronger a multipath component is, the larger the residual error due to calibration and discretization error is. This rationale leads us to select $SNR' \equiv SNR'(\tau)$ proportional to an estimate of the delay power profile. We select as such an estimate a low-pass filtered version of the delay power profile $DPP(\tau)$. In Sec. VI-B we discuss how this scheme is applied to measured CIRs.

Note that there are also alternative approaches to account for the inaccuracy of the specular model. In [32] the authors propose a method that jointly estimates the specular multipath components and the diffuse component, called dense multipath component (DMC) in a time-variant MIMO context. The

parameters of the components (direction of departure (DoD), direction of arrival (DoA), relative delay, Doppler frequency, polarimetric path gain) are estimated using an extended Kalman filter built around a dynamic model of these parameters. The parameters of the DMC are computed from the residual signal resulting after subtracting the estimated specular components from the observed signal; obviously, an accurate estimation of the specular part of the channel plays a vital role here. We now discuss the main difference of the sparse VB-SAGE algorithm proposed here with the method published in [32]. First, both algorithms apply a path pruning algorithm that relies on comparing the path weight to a threshold. The pruning algorithm proposed here is based on a Bayesian sparsity framework, while that used in [32] implements the Wald test. This leads to different ways of computing the pruning threshold and the signals compared to this threshold. Second, the sparse VB-SAGE algorithm does not make any particular assumption on the structure of the DMC. Experimental evidence suggests that the DoD-DoA-delay power spectrum characterizing the DMC typically does not factorize up to a proportionality constant in the product of the corresponding DoD, DoA, and delay spectra, as implied by the Kronecker factorization of the transmit-array–receive-array-frequency covariance matrix assumed in [32]. The inherent directionality of the radio channel, which holds for both specular components and diffuse components, translates in power spots scattered in the DoD-DoA-delay plane that cannot be represented by the above factored spectrum (see also Fig. 5(d)-5(f) and Fig. 6(d)-6(f)). This observation, combined with the other early mentioned model inaccuracies, has motivated the empirical method based on the selected $SNR'(\tau)$ threshold. Finally, the sparse VB-SAGE is derived and applied in a time-invariant SIMO scenario with only one polarization considered. As early mentioned it can be easily extended to time-variant MIMO scenario including full path polarization, provided the propagation constellation is stationary. Extension to the time-variant scenario with changing propagation constellation as considered in [32] will require further work. A thorough investigation is needed to assess the pros and contras of the model order selection methods applied in the channel estimation proposed in [32] and in the sparse VB-SAGE algorithm. This study is, however, out of the scope of this paper.

VI. APPLICATION OF THE SPARSE VB-SAGE ALGORITHM TO THE ESTIMATION OF WIRELESS CHANNELS

A. Synthetic channel responses

We first demonstrate the performance of the algorithm with synthetic channel responses generated according to model (2). We use a sounding sequence with $M = 63$ chips and a square-root-raised-cosine shaping pulse $p(t)$ with a duration $T_p = 10nsec$ and a roll-off factor 0.25. A horizontal-only propagation

scenario is considered with a single received replica of the transmitted signal represented as $w_l s(t, \boldsymbol{\theta}_l) = w_l \boldsymbol{c}(\phi_l) u(t - \tau_l)$ with w_l, ϕ_l, and τ_l denoting respectively the complex gain, the azimuthal direction and the relative delay of the lth multipath component. Thus, $\boldsymbol{\theta}_l = \{\phi_l, \tau_l\}$. The M_r-dimensional complex vector $\boldsymbol{c}(\phi_l) = [c_1(\phi_l), \ldots, c_{M_r}(\phi_l)]^T$ is the steering vector of the array [3]. We assume a linear array with $M_r = 16$ ideal isotropic sensors, spaced half a wavelength apart. The parameters of the multipath components are chosen by randomly drawing samples from the corresponding distributions: delays τ_l and angles ϕ_l are drawn uniformly in the interval $[0.03, 0.255]\mu sec$ and $[-\pi/2, \pi/2]$, respectively. For generating the multipath gains w_l we follow two scenarios. First, we generate the gains as $w_l = \sqrt{P}\mathrm{e}^{j\eta_l}$, where P is some positive constant and η_l, $l = 1, \ldots, L$, are independent random phases uniformly distributed in the interval $[0, 2\pi]$. This ensures that all multipath components have the same power P and therefore the same per-component SNR. In the second scenario the values of w_l, $l = 1, \ldots, L$, are independently drawn from a complex Gaussian distribution with the pdf $CN(w_l; 0, P'\mathrm{e}^{-\tau_l/\tau_s})$, where P' is some positive constant and τ_s is the delay spread set to $T_b/4$. In this case the distribution of the component gains w_l is conditioned on the delay τ_l such that the received power decays exponentially as the delay increases. The later choice approximates better the physical distribution of component powers versus delay. At the same time it demonstrates the performance of the algorithm under conditions with changing per-component SNR.

By sampling $\boldsymbol{z}(t)$ with a sampling period T_s we obtain the equivalent discrete-time formulation (2) with N samples per channel. The samples of the received signal are recorded over the time window $T_b = 0.63\mu sec$ (i.e., $N_u = 1$) at a rate $1/T_s = 200$MHz. In the simulations we set the number of specular components to $L = 20$. By fixing L we aim to demonstrate the possible bias of the model order selection mechanism. Additive noise $\boldsymbol{\xi}$ is assumed to be white with covariance matrix $\boldsymbol{\Sigma} = \sigma_\xi^2 \boldsymbol{I}$. Different SNR conditions are simulated. The considered SNR is the averaged per-component SNR defined as

$$SNR = \frac{1}{L} \sum_l \frac{|w_l|^2 \|\boldsymbol{s}(\boldsymbol{\theta}_l)\|^2}{\sigma_\xi^2}.$$

With this setting the estimation step (10) is implemented as a sequence of two numerical optimizations. For instance, the estimation of τ_l with $\mathcal{MB}(\tau_l) = \{\boldsymbol{x}_l, w_l, \phi_l\}$ is performed first as

$$\tau_l' = \underset{\tau_l}{\operatorname{argmax}} \left\{ \log p(\widehat{\boldsymbol{x}}_l' | \tau_l, \widehat{\phi}_l, \widehat{w}_l) - \right.$$
$$\left. \widehat{\Phi}_l \boldsymbol{s}(\tau_l, \widehat{\phi}_l)^H \boldsymbol{\Sigma}_l^{-1} \boldsymbol{s}(\tau_l, \widehat{\phi}_l) + \log p(\tau_l) \right\}, \tag{29}$$

followed by the estimation of the azimuth ϕ_l with $\mathcal{MB}(\phi_l) = \{\boldsymbol{x}_l, w_l, \tau_l\}$ as

$$
\begin{aligned}
\widehat{\phi}'_l = \operatorname*{argmax}_{\phi_l} \Big\{ & \log p(\widehat{\boldsymbol{x}}'_l | \widehat{\tau}'_l, \phi_l, \widehat{w}_l) - \\
& \widehat{\Phi}_l \boldsymbol{s}(\widehat{\tau}'_l, \phi_l)^H \boldsymbol{\Sigma}_l^{-1} \boldsymbol{s}(\widehat{\tau}'_l, \phi_l) + \log p(\phi_l) \Big\}.
\end{aligned}
\tag{30}
$$

Optimizations (29) and (30) are performed using a simple line search on a grid followed by polynomial interpolation to improve the precision of the estimates. For the initialization of the algorithm we follow the scheme described in Sec. V-B. The maximum number of initialized components is set to $L_{max} = N$. We use the modified pruning conditions (17) for the VB-SAGE-G and VB-SAGE-F schemes and (28) for the VB-SAGE-L algorithm with SNR' set to the true SNR used in the simulations. This setting demonstrates the performance of the algorithms when the true per-component SNR is known. In particular, it allows us to investigate how the modified pruning conditions can be used to control the estimation artifacts.

We compare five estimation algorithms: i) VB-SAGE-G, ii) VB-SAGE-F, iii) VB-SAGE-L, iv) the SAGE algorithm [3] with Bayesian Information Criterion for model order selection (SAGE-BIC), and v) the VB-SAGE algorithm with the negative log-evidence (NLE) approach for model order selection (VB-SAGE-NLE) [19]. The NLE is equivalent to the Bayesian interpretation of the Normalized Maximum Likelihood model order selection [7], [9]. For SAGE-BIC and VB-SAGE-NLE we set the initial number of components to the number of samples N.

We first consider the simulation scenario where all components have the same power. The corresponding results, averaged over 200 Monte Carlo runs, are summarized in Fig. 2. It can be seen that VB-SAGE-G,
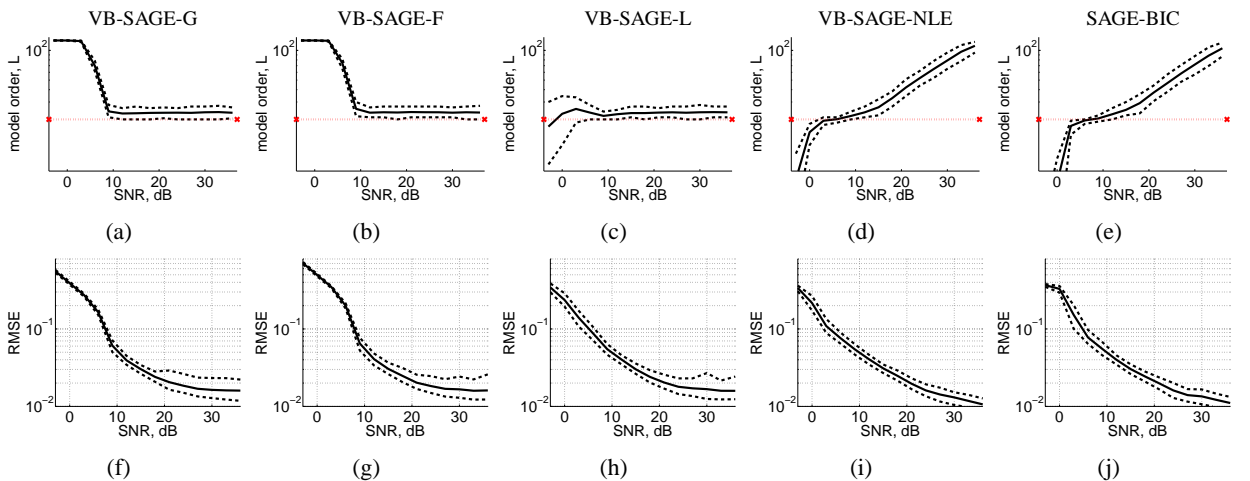

Fig. 2. Performance of the proposed estimation algorithms applied to synthetic channels with equal component power. Estimation of model order $\widehat{L}$ (a-e), and the achieved RMSE between the synthetic and reconstructed responses (f-j). The true number of components is $L = 20$ (dotted line in upper plots). The solid lines denote the averaged estimates of the corresponding parameters. Upper and lower dotted lines denote the 5th and 95th percentiles of the estimates, respectively.

VB-SAGE-F, and VB-SAGE-L clearly outperform the other two methods, with VB-SAGE-L exhibiting the best performance. Notice that (17) in VB-SAGE-G and VB-SAGE-F fails for low SNR; also the initial number of components (126 in this case) remains unchanged during the update iterations. The VB-SAGE-L algorithm, however, does not exhibit such behavior. Nonetheless, all three methods have a small positive model order bias in the high SNR regime. VB-SAGE-NLE and SAGE-BIC perform reasonably only in the limited SNR range $8 - 14$dB and fail as the SNR increases beyond. The reason for this is an inadequate penalization of the parameter likelihood, which leads to the introduction of estimation artifacts. Specifically, the selected sampling rates of the processed signals limit the precision in the estimation of the dispersion parameters $\boldsymbol{\theta}_l$ of the multipath components. As a result the mean-squared estimation errors of these estimates exhibit a floor at high SNR. These estimates are obtained by optimizing parameter-specific objective functions, cf. (29) and (30), which in a real implementation are computed from discrete signals. As a consequence, the objective functions need to be interpolated between their computed samples in these optimization procedures. It is these interpolations that lead to the flooring of the estimate errors at high SNR regime. The residual errors of the dispersion parameters translate into residual interference that may manifest itself as fictive components if not handled appropriately. This effect can also be seen as a basis mismatch problem that leads to an overestimation of true model sparsity [26]. The use of adjusted pruning conditions in case of VB-SAGE-G, -F, and -L algorithms allows for a better control over the estimation artifacts. This, however, leads to a floor of the RMSE between the synthetic and reconstructed channel responses at high SNR, as seen in Figures 2(f), 2(g), and 2(h). In contrast, VB-SAGE-NLE and VB-SAGE-BIC do not exhibit this behavior of RMSE, albeit at the expense of introducing more and more fictive multipath components to compensate for multipath parameter estimation errors as the SNR increases.[12] Increasing the number of samples N while keeping T_b fixed and increasing the number of antenna elements reduce the noise RMSE floor since the multipath dispersion parameters can be estimated with greater precision.

Obviously, the model order estimate has a significant impact on the convergence speed of the algorithm. Fig. 3 depicts the averaged number of update cycles versus SNR for the five investigated channel estimation schemes. We see here that for SNR above 12dB the VB-SAGE-G, -F, and -L schemes outperform the other estimation schemes, with the convergence rate of the VB-SAGE-L algorithm being almost independent of the SNR. Notice that the overestimation of the model order with VB-SAGE-NLE and SAGE-BIC leads to a significant increase of the number of iterations as the SNR increases.

---

[12]Note, however, that that the same effect is observed with VB-SAGE-G and VB-SAGE-L when SNR' is not used to enforce sparsity and correct for model order estimation errors.
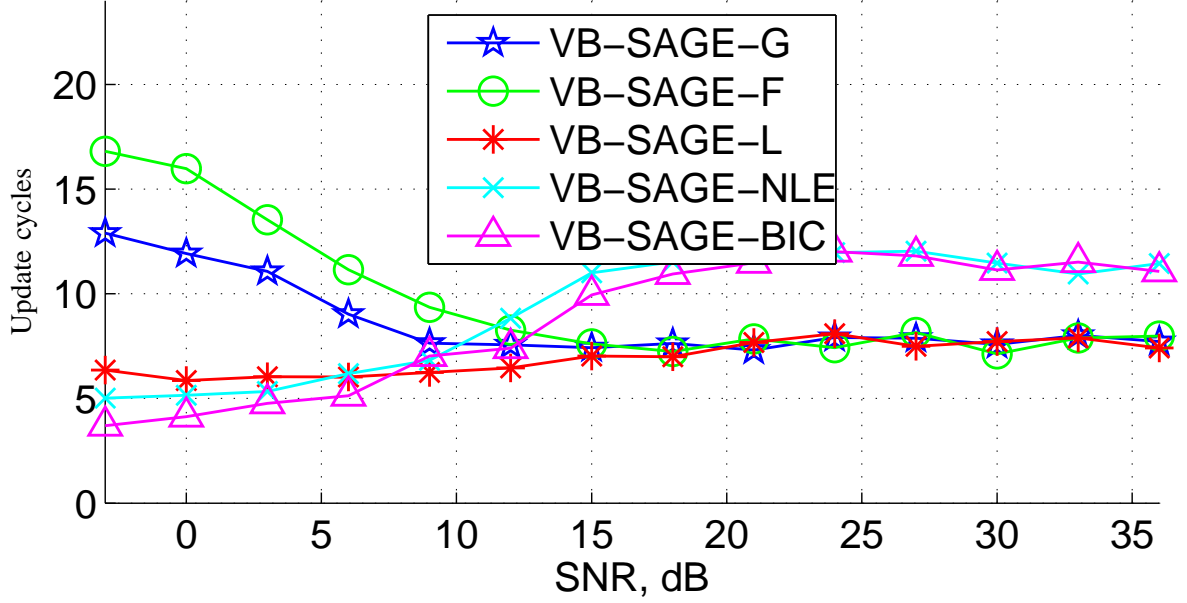
Fig. 3.   a) Averaged number of update cycles versus the averaged per-component SNR.

Let us now consider the second scenario where the component power decreases exponentially versus delay. These results are reported in Fig. 4. A picture similar to the equal-power case is observed here.
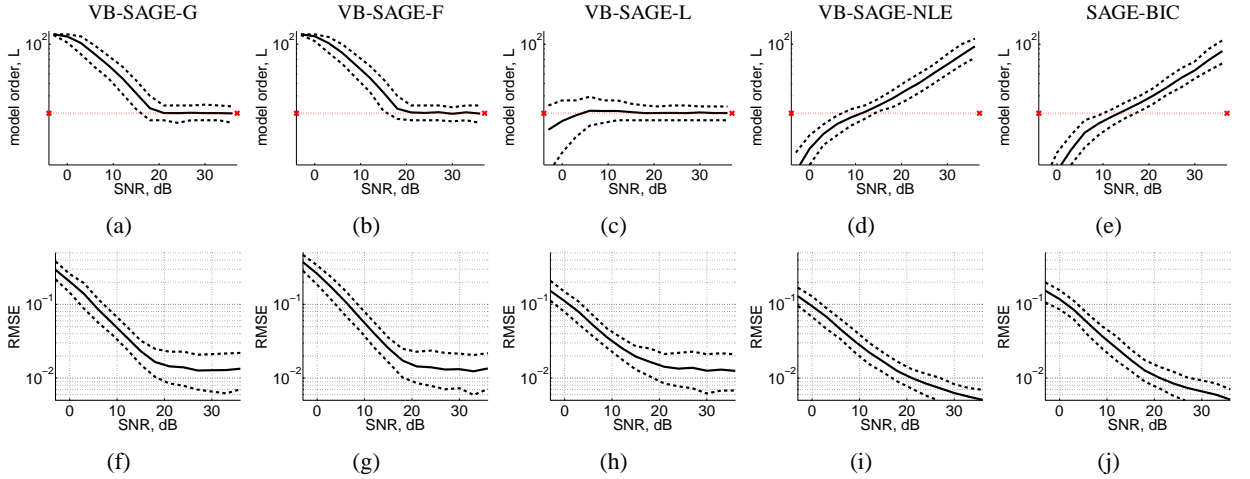

Fig. 4.   Performance of the proposed estimation algorithms applied to synthetic channels with exponentially decaying component power. Estimation of model order $\widehat{L}$ (a-e), and the achieved RMSE between the synthetic and reconstructed responses (f-j). The true number of components is $L = 20$ (dotted line in upper plots). The solid lines denote the averaged estimates of the corresponding parameters. Upper and lower dotted lines denote the 5th and 95th percentiles of the estimates, respectively.

The performance of VB-SAGE-L is clearly better than that of the other tested schemes. In this setting both VB-SAGE-G and VB-SAGE-F require higher SNR to bring the estimated model order within the

range of the true number of components. Notice that all three conditional methods are no longer biased and on average estimate the correct number of components.

B. Estimation of measured wireless channels

We now investigate the performance of the VB-SAGE-L algorithm applied to the estimation of measured wireless channel responses collected in an indoor environment. The measurements were done with the MIMO channel sounder PropSound manufactured by Elektrobit Oy. The measurement setup consisted of $M_r = 18$ receiving and $M_t = 50$ transmitting antenna elements. In the conducted experiment the sounder operated at the center frequency 5.2GHz with a chip period of $T_p = 10$nsec. The sounding sequence consisted of $M = 255$ chips, resulting in a burst waveform duration of $T_b = 2.55\mu$sec. One burst waveform was sent to sound each channel corresponding to any pair or transmit antenna and receive antenna.The received signal was sampled with the period $T_s = T_p/2$ (i.e., 2 samples/chip).

The estimation results obtained using the VB-SAGE-L algorithm are compared to those obtained with Bartlett beamformer outputs [33]. Since the receiver was equipped with a planar array, we report only the azimuthal information of the estimated multipath components. In order to minimize the effect of estimation artifacts we make use of (28). The sensitivity level SNR' is computed from the estimated delay power profile as described in Section V-E: a smoothed estimate of the delay power profile $DPP(\tau)$ is normalized with the estimated additive noise variance σ_ξ^2; the sensitivity $SNR'(\tau)$[13] is then defined as $SNR'(\tau) = \frac{DPP(\tau)}{\sigma_\xi^2}\Big/10^{1.5}$. This setting allows for a detection (removal) of components at a certain delay with power above (below) a threshold 15dB below the received power at that delay. The algorithm is initialized as described in Sec.V-B. To initialize τ_l's we partition the DPP in 8 delay segments, covering the delay interval $[10, 360]$ns. Then, using (29) and (30) we initialize at most 7 components per segment[14], which results in $L_{\max} = 56$. For the used sensitivity level $SNR'(\tau)$ the algorithm estimates $L = 18$ components. The parameter estimates of these components are summarized in Fig. 5 and 6.

Investigations, not reported due to space limitation, show that the estimated multipath components can be associated to propagation paths computed from the geometry of the environment using ray-tracing.

Due to the delay-dependent sensitivity level $SNR'(\tau)$ very weak components at the tails of the delay response are also detected. Their positions coincide well with the maxima of the Bartlett spectrum

[13]A possible extension, not considered here due to space limitations, would consists in making SNR' both delay and direction dependent.

[14]The initialization of the multipath components located in a delay segment is interrupted when the pruning condition (26) fails.
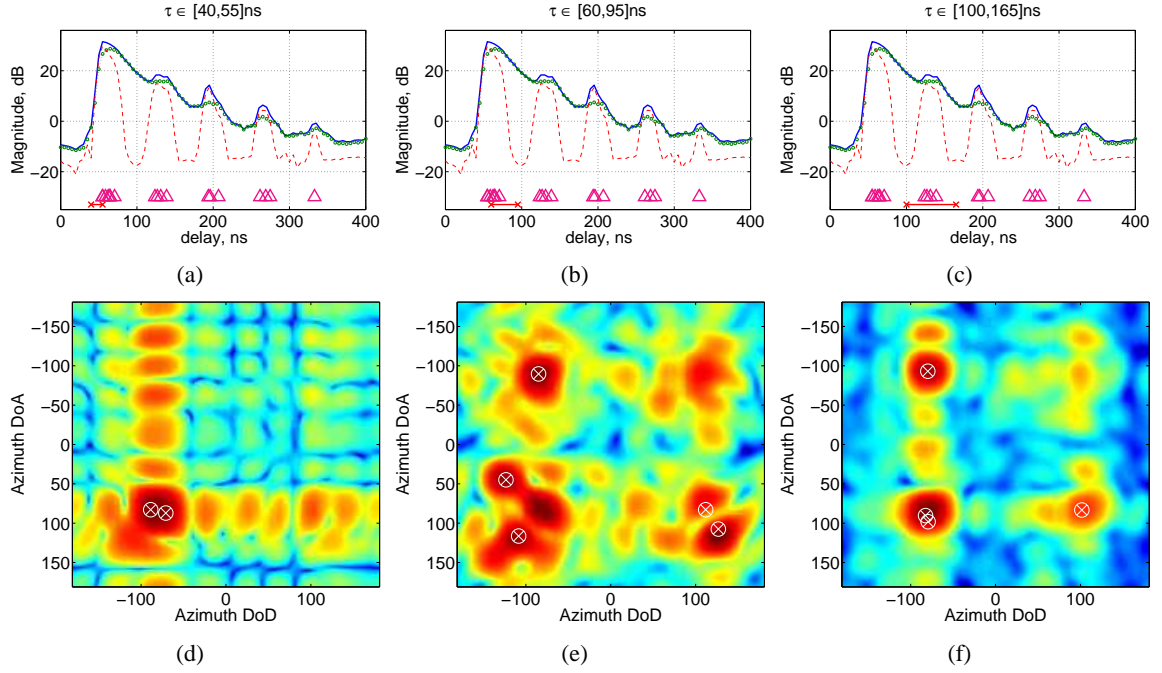
Fig. 5. (a-c) Bartlett estimates (solid line) and model-based estimates (dashed line) of the delay power profile; dotted lines denote the estimated delay power profile of the residual $\boldsymbol{\xi}$; triangles denote the delays of the estimated components; (d-f) normalized Bartlett estimates of the azimuth of arrival and departure for the selected delay ranges (denoted by crosses in figures (a-c), respectively.

estimates. We also note that not all of the "footprints" in the Bartlett spectrum have been identified as multipaths. This is due to the component magnitudes being below the detection sensitivity of the algorithm; also, some of the footprints observed in the Bartlett spectrum are likely due to side lobes caused by the system response and thus may not correspond to any true physical multipath component.

VII. CONCLUSION

This contribution proposes a new algorithm that estimates the number of relevant multipath components in the response of radio channels and the parameters of these components within the Bayesian framework. High-resolution estimation of the multipath components is performed using the Variational Bayesian SAGE (VB-SAGE) algorithm – a new extension of the traditional SAGE algorithm – which allows computing estimates of the posterior probability density functions (pdfs) of the component parameters, rather than parameter point estimates. By introducing sparsity priors for the multipath component gains, the sparse VB-SAGE algorithm allows estimating the posterior pdfs of the component parameters jointly with the posterior pdfs of the sparsity parameters by minimizing the variational free energy. The pdfs of the parameters of a single component are updated at each iteration of the algorithm, with the iterations
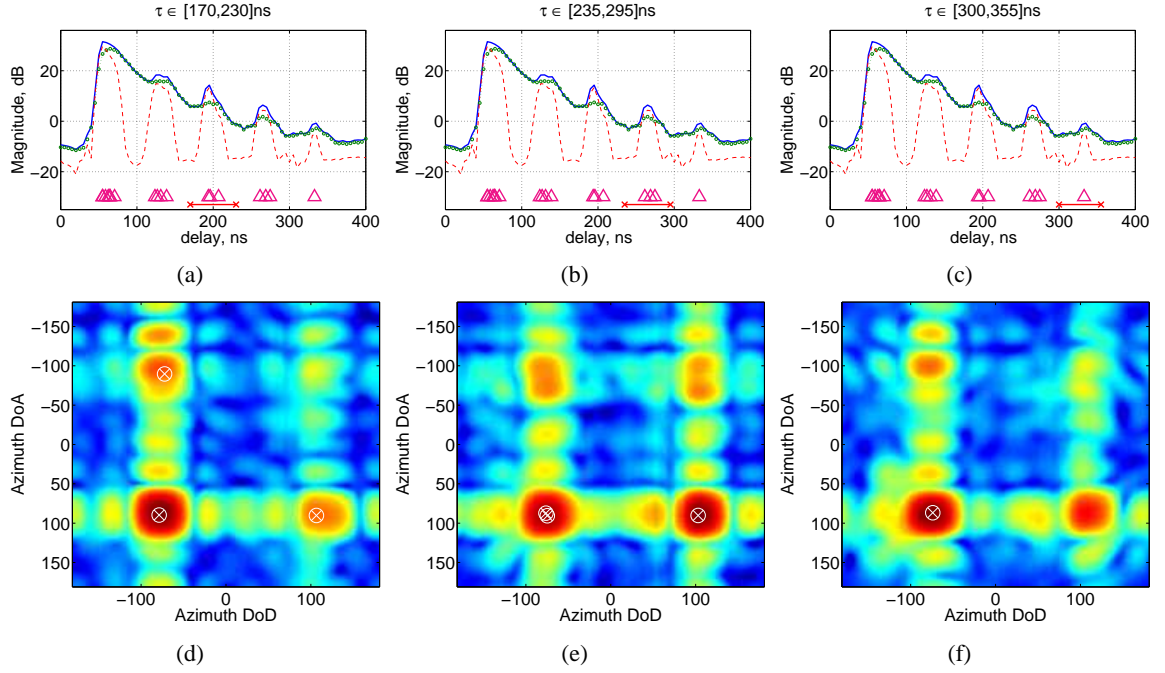
Fig. 6. (a-c) Bartlett estimates (solid line) and model-based estimates (dashed line) of the delay power profile; dotted lines denote the estimated delay power profile of the residual $\boldsymbol{\xi}$; triangles denote the delays of the estimated components; (d-f) normalized Bartlett estimates of the azimuth of arrival and departure for the selected delay ranges (denoted by crosses in figures (a-c), respectively.

cycling through the components. Due to the Monotonicity Property of the VB-SAGE algorithm, the free energy is non-decreasing versus the iterations.

Several sparsity priors are considered: Gaussian, flat and Laplace priors. The admissible hidden data introduced in the VB-SAGE algorithm allow obtaining simple and easy to interpret component pruning rules/conditions for these priors. Theses conditions are shown to be equivalent to removing signal components based on comparison of the per-component SNR with a given threshold. This threshold can be set for all components or tailored for each component individually.

The sparse VB-SAGE algorithm is applied to the estimation of the multipath components in the response of synthetic and measured wireless multipath channels. We show by means of Monte Carlo simulations that the sparsity-based model order selection methods with sensitivity-adjusted pruning conditions outperform the Bayesian Information Criterion and the Negative Log-Evidence model order selection criterion. These methods fail since, due to various effects (calibration errors, finite precision in the discretization process, diffuse scattering, etc.) leading to a model mismatch, numerical artifacts are introduced, which lead to a decreasing RMSE at the expense of an increased model order. In case of estimation of wireless channels this is highly undesirable, since the estimated artifacts have no physical

meaning. The proposed modifications of the pruning conditions allow correcting for possible model order estimation bias due to modeling mismatch. Making use of the Laplace prior results in the best performance among the tested methods. Simulations show that for low SNR the VB-SAGE algorithm with Laplace sparsity priors, which we refer to as the VB-SAGE-L algorithm, keeps only reliably estimated components, while successfully removing the artifacts. The VB-SAGE-L algorithm also exhibits the fastest convergence as compared to the other tested algorithms with the same stopping criterion.

We apply the VB-SAGE-L algorithm to the estimation of the multipath components in the measured CIRs. In order to minimize the effects of model mismatch, the detector sensitivity SNR' is adjusted based on an estimate of the delay power profile. Since the artifacts are typically more pronounced in areas of the high received power, a smoothed version of the delay power profile can be used as an indicator of the received power versus propagation delay. Investigations, not reported in this paper due to space limitation, show that the estimated multipath components can be associated to propagation paths computed from the geometry of the environment using ray-tracing.

The sparse VB-SAGE algorithm provides a new and effective tool for efficient estimation of wireless channels. Its flexibility and its iterative structure make it very attractive for many applications in wireless communications: analysis and estimation of complex MIMO channel configurations in channel sounding and MIMO radars, channel estimation in iterative receivers performing joint channel estimation and data decoding, as well as extraction of location-dependent features of the radio channel for localization purposes.

APPENDIX A
MONOTONICITY PROPERTY OF THE VB-SAGE ALGORITHM

Define $\mathcal{A}_l = \{w_l, \boldsymbol{\theta}_l, \alpha_l\}$ as the set of parameters associated with the lth multipath component and $\mathcal{R}_l = \{w_k, \boldsymbol{\theta}_k, \alpha_k; k \in \overline{\mathcal{I}(l)}\}$ as the set of the other multipath parameters. We assume that $q(\mathcal{A}_l, \mathcal{R}_l) = q(\mathcal{A}_l)q(\mathcal{R}_l)$. It is straightforward to show that minimizing the free energy $\mathcal{F}(q(\mathcal{A}_l, \mathcal{R}_l) \| p(\boldsymbol{z}, \mathcal{A}_l, \mathcal{R}_l))$ with respect to $q(\mathcal{A}_l)$ is equivalent to minimizing $\mathcal{F}(q(\mathcal{A}_l) \| \tilde{p}(\boldsymbol{z}, \mathcal{A}_l))$, where $\tilde{p}(\boldsymbol{z}, \mathcal{A}_l) \propto \exp\left(\mathbb{E}_{q(\mathcal{R}_l)}\{\log p(\boldsymbol{z}, \mathcal{A}_l, \mathcal{R}_l)\}\right)$. The VB-SAGE algorithm facilitates this optimization using the admissible hidden data $\boldsymbol{x}_l$ in (3). Consider the equality $p(\boldsymbol{x}_l, \boldsymbol{z}, \mathcal{A}_l, \mathcal{R}_l) = p(\boldsymbol{x}_l | \boldsymbol{z}, \mathcal{A}_l, \mathcal{R}_l)p(\boldsymbol{z}, \mathcal{A}_l, \mathcal{R}_l)$. By combining this equality with the factorization (4) and computing the expectation with respect to $\boldsymbol{x}_l$

and $\mathcal{R}_l$ we obtain

$$\mathbb{E}_{q(\mathcal{R}_l)}\{\log p(\boldsymbol{z}, \mathcal{A}_l, \mathcal{R}_l)\} = \mathbb{E}_{q(\boldsymbol{x}_l)}\{\log p(\boldsymbol{x}_l, \mathcal{A}_l)\}$$

$$-\mathbb{E}_{q(\boldsymbol{x}_l)}\mathbb{E}_{q(\mathcal{R}_l)}\{\log p(\boldsymbol{x}_l | \boldsymbol{z}, \mathcal{A}_l, \mathcal{R}_l)\} + const$$

where $const$ is a term independent of $\mathcal{A}_l$. Define now $\tilde{\tilde{p}}(\mathcal{A}_l) \propto \exp\left(\mathbb{E}_{q(\boldsymbol{x}_l)}\{\log p(\boldsymbol{x}_l, \mathcal{A}_l)\}\right)$. Observe that $p(\boldsymbol{x}_l, \mathcal{A}_l)$ is a function of the admissible hidden data and of the lth multipath component parameters. Now, the free energy with respect to $\mathcal{A}_l$ can be rewritten as

$$\mathcal{F}(q(\mathcal{A}_l)\|\tilde{p}(\boldsymbol{z}, \mathcal{A}_l)) = \mathcal{F}(q(\mathcal{A}_l)\|\tilde{\tilde{p}}(\mathcal{A}_l))$$

$$-\mathbb{E}_{q(\boldsymbol{x}_l)}\mathbb{E}_{q(\mathcal{A}_l)}\mathbb{E}_{q(\mathcal{R}_l)}\{\log p(\boldsymbol{x}_l | \boldsymbol{z}, \mathcal{A}_l, \mathcal{R}_l)\} + const. \tag{31}$$

Minimizing $\mathcal{F}(q(\mathcal{A}_l)\|\tilde{\tilde{p}}(\mathcal{A}_l))$ is typically simpler as compared to minimizing $\mathcal{F}(q(\mathcal{A}_l)\|\tilde{p}(\boldsymbol{z}, \mathcal{A}_l))$. However, whether $\mathcal{F}(q(\mathcal{A}_l)\|\tilde{p}(\boldsymbol{z}, \mathcal{A}_l))$ decreases as $\mathcal{F}(q(\mathcal{A}_l)\|\tilde{\tilde{p}}(\mathcal{A}_l))$ decreases ultimately depends on the term $\mathbb{E}_{q(\boldsymbol{x}_l)}\mathbb{E}_{q(\mathcal{A}_l)}\mathbb{E}_{q(\mathcal{R}_l)}\{\log p(\boldsymbol{x}_l | \boldsymbol{z}, \mathcal{A}_l, \mathcal{R}_l)\}$ in (31).

Let $q(\mathcal{A}_l)$ denote an existing (old) estimate of $\mathcal{A}_l$, and let $q'(\mathcal{A}_l)$ be the new minimizer of $\mathcal{F}(q(\mathcal{A}_l)\|\tilde{\tilde{p}}(\mathcal{A}_l))$. A current estimate $q(\boldsymbol{x}_l)$ of the admissible hidden data posterior pdf is given by (7), i.e., $q(\boldsymbol{x}_l) = \tilde{p}(\boldsymbol{x}_l) \propto \exp\left(\mathbb{E}_{q(\mathcal{A}_l)}\mathbb{E}_{q(\mathcal{R}_l)}\{\log p(\boldsymbol{x}_l | \boldsymbol{z}, \mathcal{A}_l, \mathcal{R}_l)\}\right)$, since $\mathcal{MB}(\boldsymbol{x}_l) = \{\boldsymbol{z}, \mathcal{A}_l, \mathcal{R}_l\}$. Note that it is easy to show that $\log \tilde{p}(\boldsymbol{x}_l)$ must be quadratic in $\boldsymbol{x}_l$. Similarly we define $\tilde{p}'(\boldsymbol{x}_l) \propto \exp\left\{\mathbb{E}_{q'(\mathcal{A}_l)}\mathbb{E}_{q(\mathcal{R}_l)}\{\log p(\boldsymbol{x}_l | \boldsymbol{z}, \mathcal{A}_l, \mathcal{R}_l)\}\right\}$. With these settings it follows that

$$\mathcal{F}(q(\mathcal{A}_l)\|\tilde{p}(\boldsymbol{z}, \mathcal{A}_l)) - \mathcal{F}(q'(\mathcal{A}_l)\|\tilde{p}(\boldsymbol{z}, \mathcal{A}_l)) =$$

$$\mathcal{F}(q(\mathcal{A}_l)\|\tilde{\tilde{p}}(\mathcal{A}_l)) - \mathcal{F}(q'(\mathcal{A}_l)\|\tilde{\tilde{p}}(\mathcal{A}_l)) \tag{32}$$

$$+\mathrm{D}_{\mathrm{KL}}(\tilde{p}(\boldsymbol{x}_l)\|\tilde{p}'(\boldsymbol{x}_l)) \geq 0.$$

Result (32) expresses the Monotonicity Property of the VB-SAGE algorithm. Furthermore, $q(\boldsymbol{x}_l) = \tilde{p}(\boldsymbol{x}_l) \propto \exp\left\{\mathbb{E}_{q(\mathcal{A}_l)}\mathbb{E}_{q(\mathcal{R}_l)}\{\log p(\boldsymbol{x}_l | \boldsymbol{z}, \mathcal{A}_l, \mathcal{R}_l)\}\right\}$ is a sufficient condition that guarantees the monotonicity of the VB-SAGE algorithm for our estimation problem.

REFERENCES

[1] T. S. Rappaport, *Wireless Communications. Principles and Practice.* Prentice Hall PTR, 2002.

[2] H. Krim and M. Viberg, "Two decades of array signal processing research: the parametric approach," *IEEE Signal Processing Mag.*, pp. 67–94, July 1996.

[3] B. Fleury, M. Tschudin, R. Heddergott, D. Dahlhaus, and K. I. Pedersen, "Channel parameter estimation in mobile radio environments using the SAGE algorithm," *IEEE Journal on Sel. Areas in Comm.*, vol. 17, no. 3, pp. 434–450, March 1999.

[4] O. Besson and P. Stoica, "Decoupled estimation of DOA and angular spread for a spatially distributed source," *IEEE Trans. on Sig Proc.*, vol. 48, no. 7, pp. 1872–1882, 2000.

[5] A. Richter, "Estimation of Radio Channel parameters : Models and Algorithms," Ph.D. dissertation, Technische Universität Ilmenau, 2005.

[6] H. Akaike, "A new look at the statistical model identification," *Trans. on Autom. Control*, vol. 19, no. 6, pp. 716–?723, Dec. 1974.

[7] J. I. Myung, D. J. Navarro, and M. A. Pitt, "Model selection by normalized maximum likelihood," *J. of Math. Psychology*, vol. 50, pp. 167–179, 2005.

[8] D. J. MacKay, *Information Theory, Inference, and Learning Algorithms*. Cambridge University Press, 2003.

[9] A. Lanterman, "Schwarz, Wallace, and Rissanen: Intertwining themes in theories of model order estimation," *International Statistical Review*, vol. 69, no. 2, pp. 185–212, 2000.

[10] M. Feder and E. Weinstein, "Parameter Estimation of Superimposed Signals Using the EM Algorithm," *IEEE Trans. on Acoustics, Speech, and Sig. Proc.*, vol. 36, no. 4, pp. 477–489, April 1988.

[11] D. G. Tzikas, A. C. Likas, and N. P. Galatsanos, "The variational approximation for Bayesian inference," *IEEE Sig. Proc. Magazine*, vol. 25, no. 6, pp. 131–146, November 2008.

[12] D. Malioutov, M. Cetin, and A. Willsky, "A sparse signal reconstruction perspective for source localization with sensor arrays," *IEEE Trans. on Sign. Proc.*, vol. 53, no. 8, pp. 3010–3022, 2005.

[13] D. Wipf and B. Rao, "Sparse Bayesian learning for basis selection," *IEEE Trans. on Sig. Proc.*, vol. 52, no. 8, pp. 2153 – 2164, aug. 2004.

[14] M. Tipping, "Sparse Bayesian learning and the relevance vector machine," *J. of Mach. Learning Res.*, vol. 1, pp. 211–244, June 2001.

[15] M. Figueiredo, "Adaptive sparseness for supervised learning," *IEEE Trans. on Pattern Analysis and Machine Intel.*, vol. 25, no. 9, pp. 1150–1159, 2003.

[16] W. Bajwa, J. Haupt, A. Sayeed, and R. Nowak, "Compressed channel sensing: A new approach to estimating sparse multipath channels," *Proceedings of the IEEE*, vol. 98, no. 6, pp. 1058–1076, June 2010.

[17] M. E. Tipping and A. C. Faul, "Fast marginal likelihood maximisation for sparse bayesian models," in *roceedings of the Ninth International Workshop on Artificial Intelligence and Statistics*, Key West, FL,, January 2003.

[18] R. Neal, *Bayesian Learning for Neural Networks*, ser. Lecture Notes in Stat. New York: Springer-Verlag, 1996, vol. 118.

[19] D. Shutin, G. Kubin, and B. H. Fleury, "Application of the evidence procedure to the analysis of wireless channels," *EURASIP Journal on Advances in Signal Processing*, vol. 2007, pp. 1–23, 2007.

[20] Y. Tsaig and D. L. Donoho, "Extensions of compressed sensing," *Signal Processing*, vol. 86, no. 3, pp. 549 – 571, 2006.

[21] J. W. Wallace and M. a. Jensen, "Sparse Power Angle Spectrum Estimation," *IEEE Trans. on Antennas and Propagation*, vol. 57, no. 8, pp. 2452–2460, Aug. 2009.

[22] P. Zhao and B. Yu, "On model selection consistency of LASSO," *J. Mach. Learn. Res.*, vol. 7, pp. 2541–2563, 2006.

[23] D. L. Donoho and M. Elad, "Optimally sparse representation in general (nonorthogonal) dictionaries via ℓ_1 minimization," *Proc. of the Nat. Acad. of Sciences of the USA*, vol. 100, no. 5, pp. 2197–2202, 2003.

[24] R. Tibshirani, "Regression shrinkage and selection via the LASSO," *J. R. Statist. Soc.*, vol. 58, pp. 267–288, 1994.

[25] M. Figueiredo, R. Nowak, and S. Wright, "Gradient projection for sparse reconstruction: Application to compressed sensing and other inverse problems," *IEEE J. on of Sel. Topics in Sig. Proc.*, vol. 1, no. 4, pp. 586–597, Dec. 2007.

[26] Y. Chi, A. Pezeshki, L. Scharf, and R. Calderbank., "Sensitivity to basis mismatch in compressed sensing," in *Int. Conf. Acoustics, Speech, and Sig. Proc.*, 2010.

[27] M. J. Beal, "Variational Algorithm for Approximate Bayesian Inference," Ph.D. dissertation, University College London, 2003.

[28] J. Fessler and A. Hero, "Space-alternating generalized Expectation-Maximization algorithm." *IEEE Transactions on Signal Processing*, vol. 42, pp. 2664–2677, Oct. 1994.

[29] D. Shutin and H. Koeppl, "Application of the evidence procedure to linear problems in signal processing," in *Proc. of the 24th Int. Workshop on Bayesian Infer. and Max. Entr. Methods in Sc. and Eng.*, July 2004, pp. 124–127.

[30] D. J. C. MacKay, "Bayesian Methods for Backpropagation Networks," in *Models of Neural Networks III*, E. Domany, J. L. van Hemmen, and K. Schulten, Eds. New York: Springer-Verlag, 1994, ch. 6, pp. 211–254.

[31] C. M. Bishop, *Pattern Recognition and Machine Learning (Information Science and Statistics)*. Springer, August 2006.

[32] J. Salmi, A. Richter, and V. Koivunen, "Detection and tracking of MIMO propagation path parameters using state-space approach," *IEEE Trans. on Sig. Proc.*, vol. 57, no. 4, pp. 1538–1550, April 2009.

[33] H. L. V. Trees, *Optimum Array Processing: Part IV of Detection, Estimation, and Modulation Theory*. John Wiley & Sons, Inc., 2002.

REFERENCES

[1] WHERE2 Partners. Wireless Hybrid Enhanced Mobile Radio Estimators (Phase 2) Annex I - "Description of Work". Annex FP7-ICT-2009-4, WHERE2, 2009.

[2] C. Mensing, S. Sand, A. Dammann, and W.Utschick. Location Estimation in Cellular OFDM Communications Systems. In *IEEE Global Communications Conference (GLOBECOM)*, Honolulu, USA, November/December 2009.

[3] W. Wang, T. Jost, C. Gentner, A. Dammann, and U. Fiebig. Outdoor-to-Indoor Channels at 2.45 GHz and 5.2 GHz for Geolocation Applications. In *The 5th European Conference on Antennas and Propagation (Eucap)*, Rome, Italy, April 2011.

[4] W. Wang and T. Jost. Multiple-Links NLoS Error Evaluations for Geolocation Channel Modelling. In *The 71th IEEE Vehicular Technology Conference (VTC 2010 - Spring)*, Taipei, Taiwan, May 2010.

[5] C.L. Holloway, M.G. Cotton, and P. McKenna. A model for predicting the power delay profile characteristics inside a room. *IEEE Trans. Veh. Technol.*, 48(4):1110–1120, 1999.

[6] J.B. Andersen, J.O. Nielsen, G.F. Pedersen, G. Bauch, and J.M. Herdin. Room electromagnetics. *IEEE Antennas Propagat. Mag.*, 49(2):27–33, 2007.

[7] Heinrich Kuttruff. *Room Acoustics*. Taylor & Francis, London, fourth edition, 2000.

[8] David A. Hill. *Electromagnetic Fields in Cavities: Deterministic and Statistical Theories*. IEEE Press Series on Electromagnetic Wave Theory. Wiley/IEEE Press, Piscataway, NJ, 2009.

[9] G. Steinböck, T. Pedersen, and B.H. Fleury. Model for the Path Loss of In-room Reverberant Channels. In *Vehicular Technology Conference (VTC 2011-Spring), 2011 IEEE 73rd*, pages 1–5, May 2011.

[10] J. Kunisch and J. Pamp. Measurement results and modeling aspects for the UWB radio channel. In *IEEE Conf. on Ultra Wideband Systems and Technologies, 2002. Digest of Papers*, pages 19–24, May 2002.

[11] T. Pedersen, G. Steinböck, and B.H. Fleury. Modeling of Reverberant Radio Channels Using Propagation Graphs. *IEEE Trans. Antennas Propagat.*, submitted.

[12] G. Turin, F. Clapp, T. Johnston, S. Fine, and D. Lavry. A statistical model of urban multipath propagation channel. *IEEE Trans. Veh. Technol.*, 21:1–9, February 1972.

[13] Adel A. M. Saleh and Reinaldo A. Valenzuela. A statistical model for indoor multipath propagation channel. *IEEE J. Select. Areas Commun.*, SAC-5(2):128–137, February 1987.

[14] Dmitriy Shutin and Bernard H. Fleury. Sparse variational Bayesian SAGE algorithm with application to the estimation of multipath wireless channels. *to appear in IEEE Transactions on Signal Processing*, 2011.

[15] B.H. Fleury, M. Tschudin, R. Heddergott, D. Dahlhaus, and K. Pedersen. Channel Parameter Estimation in Mobile Radio Environments Using the SAGE Algorithm. *IEEE J. Select. Areas Commun.*, 17(3):434–450, March 1999.